

学位論文

Studies on interactions of molecules with
intense femtosecond laser pulses
(高強度フェムト秒レーザーパルスと分子
との相互作用に関する研究)

平成26年12月博士(理学)申請
東京大学大学院理学系研究科
物理学専攻 酒見 悠介

Abstract

Interaction of a strong laser field with matter causes many interesting phenomena such as high-order harmonic generation and nonsequential double ionization. The applications of these phenomena include attosecond pulse generation and tomographic imaging of molecular orbitals, and attract scientists with various backgrounds (physics, chemical physics, biochemistry). The present thesis aims to reveal the dynamics of high-order harmonic generation with carrier-envelope-phase (CEP) stabilized pulses (first part) and of tunnel ionization from polar molecules (second part).

In the first part, we show the observations of the high-order harmonic spectra generated in aligned molecules with CEP stabilized pulses. The spectrum has clear structures in the cutoff region (the shortest wavelength region) where their shape changes depending on the value of the CEP. A Fourier analysis reveals that the structures stem from the interference of attosecond bursts, and that the magnitude of the chirp of the high-order harmonics (harmonic chirp) can be estimated by comparing the experimental results with a simple model. The effects of the phase variation in high-order harmonics depending on the orientation direction of molecules are also discussed.

In the second part, we study the tunnel ionization dynamics of carbonyl sulfide by observing the molecular-frame photoelectron distributions (MF-PADs) correlated with the fragment ions produced from photodissociation of carbonyl sulfide (S^+ , CO^+ , CS^+ , and O^+) with a coincidence velocity-map imaging spectrometer. The MF-PADs have clear asymmetry, and depend on the species of the fragment ions. The asymmetry becomes more significant as the laser intensity increases from $5 \times 10^{13} \text{ W/cm}^2$ to $2.2 \times 10^{14} \text{ W/cm}^2$. Since the asymmetry reflects the angular-dependent ionization rates of OCS molecules, the observed asymmetry indicates that electrons are more likely to be ionized from the O atom than from the S atom for S^+ , CO^+ , and CS^+ , and vice versa for O^+ . The results imply that the dissociation processes and the tunnel ionization processes are correlated with each other. We qualitatively discuss the mechanism by giving a hypothetical idea that the difference in the asymmetry depending on the correlated dissociation channels corresponds to the tunnel ionization of different (inner) molecular orbitals, leading to the difference in the (excited) states of the produced ions.

Contents

Abbreviations and conventions	3
1 Introduction	5
1.1 Strong field interaction	5
1.2 Motivation	9
1.2.1 High-order harmonics generated from aligned molecules with carrier-envelope-phase stabilized pulses	10
1.2.2 Coincidence study of tunnel ionization dynamics in OCS molecules	11
1.3 Contents of this thesis	15
2 Theoretical background	16
2.1 Strong field ionization	16
2.1.1 Atomic tunneling theory	16
2.1.2 Molecular tunneling theory	18
2.2 High-order harmonic generation	21
3 High-order harmonics generated from aligned molecules with carrier-envelope-phase stabilized pulses	24
3.1 Experiment	24
3.1.1 Laser	25
3.1.2 Vacuum system	30
3.1.3 Optics	30
3.1.4 Chamber apparatus	31
3.1.5 Field-free molecular alignment	32
3.2 Results	34
3.2.1 Molecular alignment	34
3.2.2 CEP effects	35
3.2.3 Fourier analysis	36
3.2.4 Simulation with the Lewenstein model	41

3.3	Discussion	41
3.3.1	Simple model to describe origine of peaks in Fourier spectrum	41
3.3.2	Model simulation	43
3.3.3	Effects of phase jump	47
3.4	Summary	48
4	Coincidence study of tunnel ionization dynamics in OCS molecules	49
4.1	Experiment	49
4.1.1	CO-VIS apparatus	49
4.1.2	Angular streaking and optical setup	55
4.1.3	Reconstruction of momenta of ion and electrons	59
4.1.4	Momentum calibration	60
4.2	Results	64
4.2.1	Mass spectrum	64
4.2.2	Momentum distribution	66
4.2.3	Coincidence measurement	71
4.2.4	Dissociation probability	75
4.2.5	Reference experiment: CO ₂ molecular sample	83
4.3	Discussion	86
4.3.1	MF-PADs calculated by the WFAT theory	86
4.3.2	Dissociation mechanism	90
4.4	Summary	93
5	Concluding remarks	94
A	Atomic units	98
	Bibliography	100

Abbreviations and conventions

Unless specified, abbreviations and symbols have the meaning below.

Abbreviation	Meaning
ADK theory	Ammosov–Delone–Krainov theory
amu	Atomic mass unit
a.u.	Atomic units
CEP	Carrier-envelope phase
CPA	Chirped pulse amplification
CW	Clockwise
CCW	Counterclockwise
FWHM	Full width at half maximum
HHG	High-order harmonic generation
HHs	High-order harmonics
HOMO	Highest occupied molecular orbital
KLM	Kerr-lens mode
LCP	Left circularly polarized pulse
MF-PAD	Molecular frame photoelectron angular distribution
MO-ADK theory	Molecular Ammosov–Delone–Krainov theory
RCP	Right circularly polarized pulse
TOF	Time of flight
WFAT	Weak-field asymptotic theory
Symbol	
I_p	Ionization potential
I	Intensity of laser field
p	Momentum
U_p	Ponderomotive potential
F	Electric field
Γ	Ionization rate





	Turbo molecular pump
	Scrol vacuum pump
	Valve
	Gate valve

Figure 1: Vacuum symbols defined in Ref. [1].

Chapter 1

Introduction

Intense laser fields have become available with the technical advance of ultrashort laser pulse [2]. Such laser fields can compete with the Coulomb forces which electrons feel in atoms and molecules. In the intensity regime of $I \sim 10^{14}$ W/cm² the electric field strength F of the peak is given by

$$F = \sqrt{\frac{2I}{\epsilon_0 c}} \sim 3 \text{ V/\AA}, \quad (1.1)$$

where c is the speed of light in vacuum, ϵ_0 is the permittivity in vacuum. As a result, atoms and molecules interacting with intense laser fields exhibit new characteristics. In this introductory chapter, we give basic concepts of the strong field interaction in section 1.1. In section 1.2, we give our motivation of research presented in this thesis. Finally, section 1.3 explains how this thesis is organized.

1.1 Strong field interaction

A characteristic of ultrashort laser pulses is that the energy can be concentrated in a short temporal duration [3]. Besides, the maximum intensity of the ultrashort pulse can be reached before breaking matters by exciting or ionizing, which hinders us from studying the interaction between the strong fields and neutral molecules. To obtain such an intense laser pulse, a number of techniques have been developed such as Q-switching, mode locking, and chirped pulse amplification (CPA) [2, 4]. For example, CPA laser systems employing Ti:sapphire for the oscillator and amplifying medium are widely used because they can generate femtosecond pulses (Full width of half maximum (FWHM) < 100 fs) with high repetition rates ($f_{\text{rep}} > 1$ kHz), and now they are commercially available.

When laser fields are sufficiently strong, higher order processes play a significant role instead of the single-photon absorption or emission [5]. These processes are called multiphoton processes during which molecules emit or absorb more than one photon. One

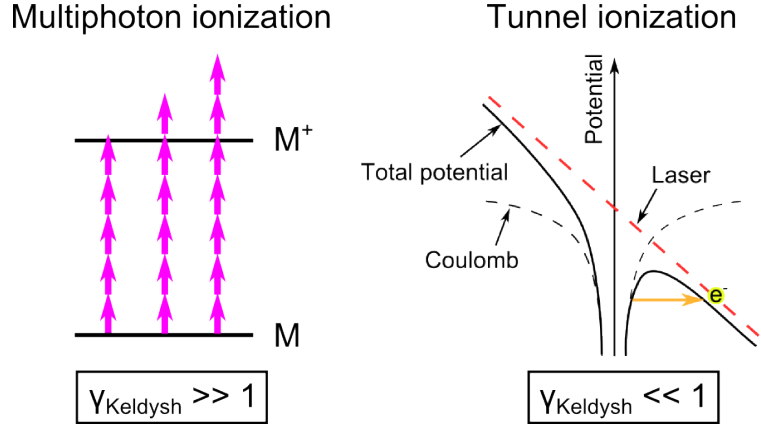


Figure 1.1: Different strong-field ionization dynamics depending on the Keldysh parameter γ_{Keldysh} .

example of multiphoton processes is the multiphoton ionization of atoms and molecules, in which electrons are ejected from the atoms and molecules by absorbing a number of photons as shown in the left panel of figure 1.1. The multi-photon description can be seen, for example, in a perturbation theory or in the Floquet theory. In the multi-photon picture, the ionization of atoms can be described [5]

$$E_{\text{kin}} = n\hbar\omega - I_p + U_p, \quad (1.2)$$

where E_{kin} is the kinetic energy of the ionized electron, n is the number of absorbed photons, \hbar is the Planck constant, I_p is the ionization potential, and U_p is the induced Stark shifts of the Rydberg and continuum states (ponderomotive energy) defined as

$$U_p \equiv \frac{F^2}{4\omega^2}, \quad (1.3)$$

where F is an electric field, and ω is an angular frequency of light. When the laser frequency is low enough, ionization can be interpreted by using a quasi-static model [6]. In the model, the bound electrons feel an effective potential formed by the Coulomb potential with the contribution due to the laser electric field (figure 1.1, right panel). In this model, ionization occurs in such a way that a bound electron tunnels out the effective potential as shown in figure 1.1. The tunnel ionization rate Γ of a hydrogen atom in a static electric field is given by Landau as [6]

$$\Gamma = \frac{4}{F} \exp\left(-\frac{2}{3F}\right). \quad (1.4)$$

The boundary of the two description of the ionization can be determined by an adiabatic parameter, γ_{Keldysh} , also known as Keldysh parameter [7]:

$$\gamma_{\text{Keldysh}} = \frac{\omega\sqrt{2I_p}}{F} = \sqrt{\frac{I_p}{2U_p}}. \quad (1.5)$$

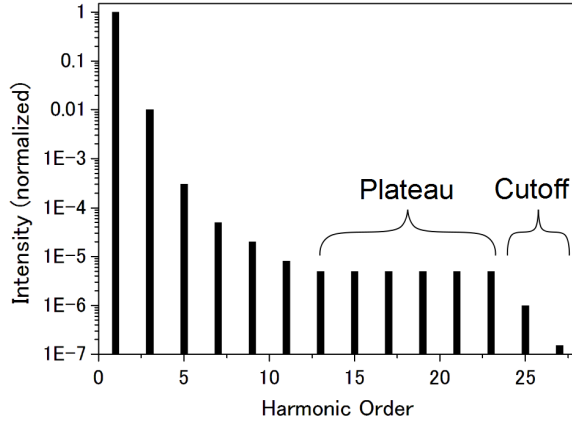


Figure 1.2: A typical spectrum of high-order harmonics.

The two descriptions are valid when the Keldysh parameter γ_{Keldysh} satisfies the following conditions:

$$\gamma_{\text{Keldysh}} \gg 1 \rightarrow \text{Multiphoton ionization} \quad (1.6)$$

$$\gamma_{\text{Keldysh}} \ll 1 \rightarrow \text{Tunnel ionization.} \quad (1.7)$$

We often refer that when $\gamma_{\text{Keldysh}} \gg 1$ it is multi-photon regime and when $\gamma_{\text{Keldysh}} \ll 1$ it is tunneling regime. This parameter offers intuitive descriptions of light-matter interactions.

On the other hand, matters interacting with an intense laser field can emit radiation at multiples of the angular frequency of the fundamental laser (harmonic generation). It was not until the invention of first laser by Maiman [8] that harmonic generation was observed at second order in 1961 [9], and at third order in 1967 [10]. Higher order harmonic generation has been observed along with the development of short laser pulses. For example, the 33rd, 29th, and 21st harmonics in argon, krypton, and xenon, respectively, were observed using a 1064 nm Nd:YAG laser pulse with a duration of 30 ps [11, 12]. In 1993, the 109th harmonic in Ne were observed using a 125 fs, 806 nm Ti:sapphire laser [13]. It was found that the high-order harmonic spectrum exhibit a rapid decrease over the first few harmonics, followed by a plateau of approximately constant intensity, and a cutoff in which the spectral intensity rapidly decreases. Figure 1.2 shows a typical spectrum of high-order harmonics. These characteristics can be reproduced by using non-perturbative approaches, because in a perturbative approach the harmonic intensity in general decreases from one order to the next.

In 1993 Corkum presented a semi-classical theory for high-order harmonic generation (HHG), which is known as three step model. Figure 1.3 shows a schematic diagram of the three step model. When a molecule is subject to an intense laser field with a long wavelength ($\gamma_{\text{Keldysh}} \ll 1$), a portion of the electron wave packet tunnels through the

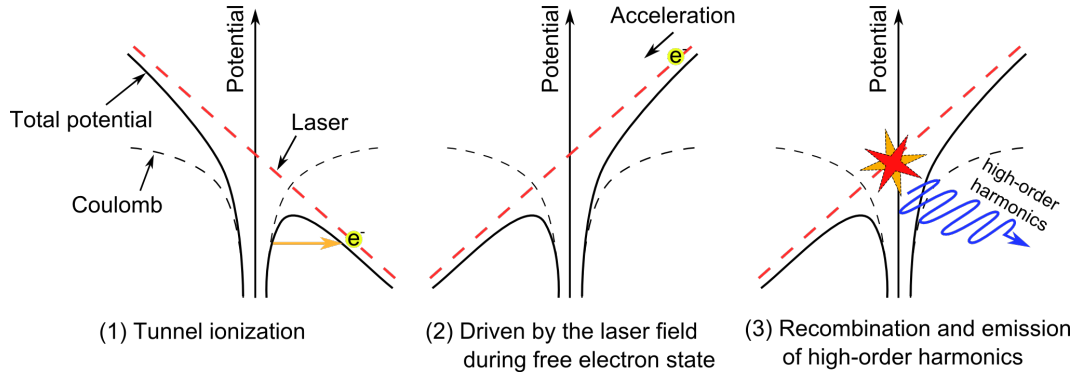


Figure 1.3: Schematic diagram of the three step model of high-order harmonic generation.

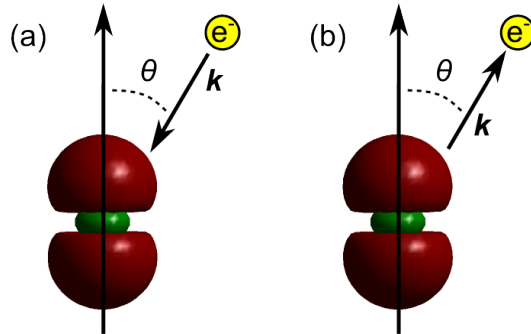


Figure 1.4: Angle-dependent interaction between molecules and laser fields in the tunneling picture. Linearly-polarized pulses are aligned at θ with respect to the molecular axis. (a) An electron with momentum \mathbf{p} recombines with a molecule at an angle of θ . (b) An electron with momentum \mathbf{p} is tunnel ionized at an angle of θ .

Coulomb potential distorted by the laser field (step 1). The electron wave packet in the continuum is driven by the laser field, and after the laser field changes its polarity, it returns to the vicinity of the parent ion (step 2). When the electron wave packet recombines with the parent ion with a probability, a high-energy photon, whose energy is the sum of the kinetic energy of the electron wave packet and the ionization potential of the neutral molecules, is emitted as a result of the coherent oscillation between the recombining electron wave packet and the bound-state electron wave function (step 3). A quantum-mechanical theory of HHG has been developed by Lewenstein *et al.* by using a strong-field approximation (SFA). As described in section 2.1, the theory not only calculates the amplitude and the phase of harmonics but also reproduce the description of the three-step model.

These tunneling-triggered phenomena have been attracting researchers because these phenomena are very sensitive to molecular orbitals. As an example; Itatani *et al.* observed high-order harmonic spectra generated from N_2 molecules by varying the direction of the

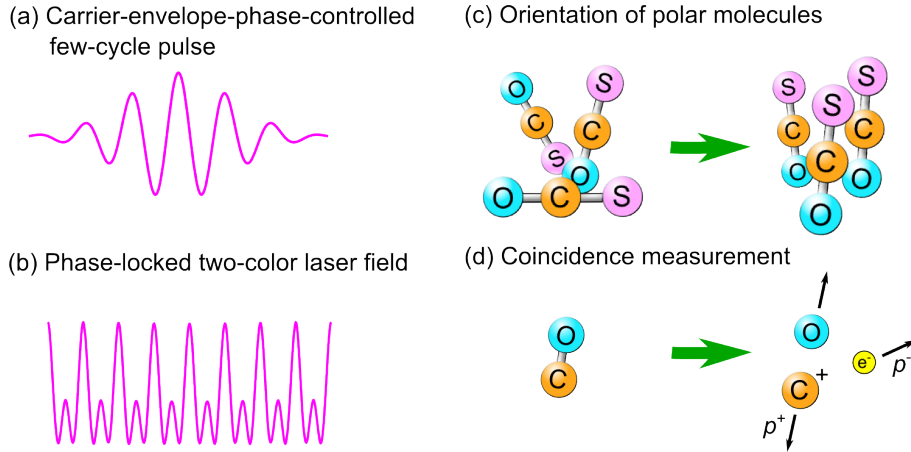


Figure 1.5: Various experimental conditions where inversion symmetry breaks. (a) A condition where a carrier-envelope-phase-controlled few-cycle pulse are used. (b) A condition where a phase-locked two-color laser pulse are used. (c) A condition where an ensemble of oriented polar molar molecules are prepared. (d) Photoion-photoelectron coincidence measurement by which the direction of molecular axis at the instant of ionization can be estimated.

molecular axis with respect to the laser polarization, and demonstrated that the highest occupied molecular orbital (HOMO) can be reconstructed from the angular-dependent spectra [14]. However, HHG process is contributed both by the tunneling, the continuum propagation, and the recombination. Each process requires sophisticated theories to accomplish the reconstruction procedure [15]. In particular, tunneling process is very sensitive to the shape of matters like the scanning tunneling microscope (STM). Akagi *et al.* observed tunnel ionization of electrons from HOMO-1 of HCl molecules by observing tunneling efficiency depending on the angle between the molecular axis and the direction of laser polarization [15].

A strong field offers an opportunity of controlling the light-matter interactions because it give rise to strong interactions without resonances. The dynamics in atoms and molecules in the strong laser field are observed by using femtosecond laser pulses. A number of strong-field phenomena such as high-order harmonic generation, non-sequential double ionization, and above-threshold ionization have been observed, and explained quantitatively. Intuitive pictures for these processes have been given in the early stage. Researchers are now eager to describe those phenomena beyond these intuitive pictures.

1.2 Motivation

As seen in the above introduction, the anisotropy of molecules affects strong-field processes. Extension of applications such as tomographic imaging of molecular orbitals to polar molecules requires observation of strong-field processes without inversion symme-

try. Those observations have been made by employing wave-form-controlled laser fields (figure 1.5 (a) and (b)) or by using oriented polar molecules (figure 1.5 (c) and (d)).

The wave-form-controlled laser fields are accomplished, for example, by using CEP stabilization technique [16] (figure 1.5 (a)) or by using phase-locked two-color laser fields (figure 1.5 (b)) [17]. The orientation of molecules are accomplished by using orientation techniques (figure 1.5 (c)) [18] or using axial recoil approximation where the direction of molecular axis at the instant of ionization is determined from dissociation fragments after the molecule has been ionized (figure 1.5 (d)) [19].

Under the conditions, interesting strong-field phenomena have been observed. For example, even-order harmonics are generated when molecules are irradiated with two-color driving pulses because of the loss of inversion symmetry of the electric fields [20]. Secondly, the photoelectron angular distribution becomes inversion asymmetric when atoms are ionized with CEP-controlled few-cycle pulses [21]. Besides, these observations have reported new findings such as single attosecond pulse generation [22], angular-dependent tunnel ionization rates of polar molecules [23], and shape resonance of CO molecules [24].

The strong-field interaction without inversion symmetry gives possibilities to reveal new dynamics; however, few observation have been done due to their experimental complexity. For example, the high-order harmonic spectrum generated with CEP-stabilized pulses has been measured only for atoms as the non-linear medium, and the photoion-photoelectron coincidence measurement has been applied only to diatomic molecules [15, 25]. Therefore, we experimentally study the strong-field interaction without inversion symmetry in more complicated situations where aligned molecules are used for the former case, and triatomic molecules are used for the latter case. In the following sections, we introduce motivations for the two experiments in detail.

1.2.1 High-order harmonics generated from aligned molecules with carrier-envelope-phase stabilized pulses

High-order harmonic generation from atoms and molecules has been extensively studied over the last quarter century. Nowadays, the researchers' attentions are placed mainly on the attosecond pulse generation and its applications [26], and molecular imaging using a sample of aligned molecules [14, 27, 28, 29, 30, 31]. Since the HHG takes place within one optical cycle and is a highly nonlinear process, each step of the HHG process can be controlled by changing the CEP of the driving pulse. In addition, since both the step 1 and the step 3 are dependent on molecular alignment, one has to prepare a sample of aligned molecules for the purpose of molecular imaging [14, 27, 28, 29]. The controllability of the HHG process by the CEP was demonstrated by observing the changes of the HHG spectra depending on the relative values of CEP a decade ago [32]. However, the

studies aimed to elucidate the underlying physics of the HHG are quite limited. With CEP-stabilized multi-cycle pulses, it is demonstrated that attosecond pulse trains can be controlled, and that the self-referencing technique, which relies on the observation of the interference fringes between the broadened spectral components of the adjacent odd-order harmonics, can be used to estimate the relative phase between them [33]. We apply the self-referencing technique to reveal that the effective duration of the driving pulse, during which the specific orders of harmonics are efficiently generated, is decreased as the harmonic order is increased. In addition, the first application of the technique to aligned molecules leads to some findings as discussed in Ref. [34]. Except for our previous work [34], CEP-stabilized femtosecond pulses have not been used in the HHG experiments with aligned molecules. Here we demonstrate that by employing CEP-stabilized pulses with an appropriate pulse width as a probe pulse, an appropriate number of attosecond pulses is generated to form clear and informative interference fringes in the high-order harmonic spectra generated from aligned molecules. In fact, by performing a detailed Fourier analysis, it is successfully revealed that the fringes are dependent on the CEP and are formed by the interference between attosecond pulses when the harmonic chirp is significantly large. We also examine the possibility of observing the harmonic phase change in the harmonic spectra generated from aligned CO₂ and N₂ without performing direct harmonic phase measurements, which usually rely on the observation of photoelectrons generated from rare gas atoms with the combination of an attosecond pulse and a driving pulse like a technique known as frequency-resolved optical gating for complete reconstruction of attosecond bursts (FROG CRAB) [35].

1.2.2 Coincidence study of tunnel ionization dynamics in OCS molecules

The tunnel ionization of atoms and molecules in strong laser fields is one of the key processes because this process is closely related to other strong field phenomena such as high-order harmonic generation [26], nonsequential double ionization [36], and above-threshold ionization [36]. The tunnel ionization is the first step of the high-order harmonic generation or other phenomena caused by re-collision [26]. Recent studies have revealed that the tunneled electrons can be applied to imaging of molecular orbitals [14] and probing nuclear dynamics [30] with attosecond resolution. Through the rescattering process, the tunnel ionized electron itself can be utilized to measure elastic scattering cross sections of the target ion with the freed free electron [37, 38, 39]. Therefore, understanding the mechanism of tunnel ionization is one of the most important subjects in strong-field physics.

The molecular ionization dynamics in strong fields has been successfully described by molecular Ammosov–Delone–Krainov (MO-ADK) theory, which predicts that the

angular-dependent ionization rate maps the the electron density profile of the ionized molecular orbitals¹ [41, 42, 43]. For example, the MO-ADK theory has reasonably described the angular dependence of ionization rates of simple molecules such as N₂ and O₂. However, recent experiments found that this prediction is not necessarily true, in particular, for polar molecules [15, 23, 44].

Recently, the strong-field interaction with polar molecules have been experimentally studied via high-order harmonics generated in polar molecules by several groups with molecular orientation techniques. Frumker *et al.* observed even-order high-harmonic spectra generated from oriented CO molecules, which can not be observed with non-polar molecules nor unoriented (randomly or only aligned) molecules for symmetry reason [45][46]. The oriented CO molecules are prepared by irradiating with a two-color femtosecond laser field. Later, Kraus *et al.* achieved to prepare strongly-oriented CO molecules for high-order harmonic generation by using a technique proposed theoretically [24, 47].

In order to solve the discrepancy of MO-ADK theory from the experimental results, several theoretical approaches have been made to calculate the angular-dependent ionization rate of polar molecules. One of the approaches is to take account of a large Stark shift, a prominent characteristics of polar molecules, into the effective ionization potential I_p^{eff} [23]:

$$I_p^{\text{eff}} = I_p + (\mu^+ - \mu)F \cos \theta \quad (1.8)$$

$$+ \frac{1}{2}F^2 \left[\left\{ (\alpha_{\parallel} - \alpha_{\parallel}^+) - (\alpha_{\perp} - \alpha_{\perp}^+) \right\} \cos^2 \theta + (\alpha_{\perp} - \alpha_{\perp}^+) \right], \quad (1.9)$$

where F is the electric field, $\mu(\mu^+)$ is the permanent dipole moment of the molecule (the molecular cation), $\alpha_{\parallel}(\alpha_{\parallel}^+)$ and $\alpha_{\perp}(\alpha_{\perp}^+)$ are the polarizability of the molecule (the molecular cation) parallel and perpendicular to the molecular axis, and θ is the angle between the electric field and the molecular axis. As described in Ref. [7], the importance of the Stark shift has been pointed out even in the case of atoms: the ionization rate increases approximately 1.5–2 times by including the Stark shift [7, 48]. Dimitrovski *et al.* extended the MO-ADK theory by taking into account the Stark shift of OCS molecules, and found that ionization of OCS molecules favors an orientation opposite to that predicted by the MO-ADK theory, which was in good agreement with the experimental results [23, 49]. As an other approach, Tolstikhin *et al.* developed the WFAT to treat the tunnel ionization of polar molecules [50]. Other theoretical approaches such as the MO-SFA theory [51], solving the time-dependent Schrödinger equation within the single-active-electron and frozen nuclei [52], and the time-dependent density-functional

¹The angular dependence of the ionization rate of molecules is particularly important because it contains information about molecular orbitals [40].

theory [53] are being developed. By experimentally examining the validity of the theories, we can acquire a deep insight into the dynamics of tunnel ionization of polar molecules. Several groups developed experimental techniques to reveal the ionization dynamics in molecules without inversion symmetry.

A straightforward approach to measure the angular-dependent ionization rate of polar molecules is to prepare oriented molecular samples. Holmegaard *et al.* is the first to measure the angular dependence of ionization rates by using a molecular orientation technique [23]. They employed a molecular deflector to select rotational states [54], and the selected molecules were oriented by a technique known as DC + AC orientation, whereby a dc electric field and a laser electric field adiabatically orient molecules [18]. They prepared highly oriented OCS molecules, strongly confined along the polarization axis and 80 % of the molecules directing their O atoms towards the detector and 20 % of them directing the opposite direction, and they subsequently observed the angle-resolved photoelectron of the sample. They used nearly circularly polarized pulses to ionize OCS molecules, and detected photoelectrons. They have found that OCS molecules are more likely to be ionized when a laser field is pointing from the O atoms to the S atoms than when it is pointing in the opposite direction.

Another approach to study the angular-dependent ionization rate of polar molecules has been done for 1-iodohexane, CO, and OCS molecules by Ohmura *et al.* [55, 56, 44] and for CO and NO molecules by Li *et al.* [57]. Ohmura *et al.* observed photofragments of OCS molecules by using femtosecond two-color laser pulses [17], and found that the momentum distributions of Coulomb exploded fragments (e.g. CO⁺ and S⁺ for OCS molecules) were sensitive to the relative phase between the two color laser pulses. They attributed the observed asymmetry in the momentum distributions to the angular dependent ionization rate of OCS, and, contrary to Holmegaard's results, concluded that OCS molecules are more likely to be ionized when the electric field points from the S end to the O end than vice versa. They pointed out that the difference might come from the excited states of OCS cations.

In addition to the above two approaches (molecular orientation and two-color laser field), a photoelectron-photoion coincidence measurement enables us to study the angular-dependent ionization rate of polar molecules, and offers another opportunities of observing of the effects of excited states during tunnel ionization.

The importance of excited states is well recognized, in particular, in high-order harmonic generation. The tunnel ionization into excited states of cations can be treated as the tunnel ionization of lower-lying orbitals such as HOMO-1 in the Hartree-Fock picture [58]. McFarland *et al.* observed high-order harmonics generated from HOMO-1 of N₂ molecules [59]. Smirnova *et al.* observed destructive interference of high-order harmonics

generated from HOMO and lower-lying orbitals of CO₂ [58]. Tunnel ionization is the first step of the generation process of high-order harmonics; however, the 2nd (acceleration) and the 3rd (recombination) processes make the analysis complicated. Therefore, the study of tunnel ionization dynamics is especially important to investigate the effects of lower-lying orbitals.

For investigating the effects of excited states, a photoelectron-photoion coincidence measurement is preferable to study the effects of lower-lying molecular orbitals because the technique can selectively measure photoelectrons correlated with fragment ions, which is preferably produced from the excited states of cations. Utilizing the existing knowledge what kind of excited states of a cation are likely to be fragmented (potential surfaces of molecular orbitals), one can know how and from what orbital an electron is tunnel ionized by tagging each electron to the fragmented ions.

Akagi *et al.* demonstrated that a photoelectron-photoion coincidence measurement enables us to study tunnel ionization of lower-lying molecular orbitals [15]. They measured the angular dependence of the ionization rate of HCl molecules by observing molecular frame photoelectron distributions (MF-PADs) correlated with HCl fragments H⁺ and Cl⁺ with a cold target recoil ion momentum spectrometer (COLTRIMS) [60]. They found that electrons in HOMO-1 are mainly ionized from the H atom despite the fact that the density of the HOMO-1 electrons are higher around the Cl atom than around the H atom. The results are apparently not consistent with the prediction of the MO-ADK theory. They calculated the angular-dependent ionization rate by a density functional theory [53] and successfully reproduced the experimental results by the HOMO-1 orbitals including 0.1 % contribution from the HOMO of HCl [15].

Wu *et al.* made coincidence measurement to observe the MF-PAD from CO molecules [25]. They observed significant contribution up to 30 % of HOMO-1 to the dissociative single ionization process. In addition, they identified double ionization of multiorbitals by observing the ion sum-momentum distribution of the exploded double ionization channel of C⁺ and O⁺. In both cases, They found the linear Stark effect plays a minor role in the ionization dynamics. Their measurement on the angular-dependent ionization rate is determined by the shape of the molecular orbitals.

As shown above, coincidence measurements on the tunnel ionization of polar molecules offer sophisticated opportunity to understand the dynamics related to excited states of cations. However, the measurements have been limited to diatomic molecules and studies on polyatomic molecules are demanded where a wealth of excited states are open to produce various fragment ions. In chapter 4, we take a triatomic molecule OCS as a sample, and make a coincidence measurement. It gives a deep insight into the dynamics of tunnel ionization because the produced cations can dissociate into many channels:

Table 1.1: Permanent dipoles μ and polarizabilities α , and ionization potentials I_p for several molecules. The data are taken from Ref. [62] unless specified.

Molecule	μ (Debye)	α (\AA^3)	I_p (eV)
OCS	0.71	7.52 [23]	11.19
CO	0.11	1.953	14.01
HCl	1.08	2.515	12.74
NO	0.15	1.698	9.26

$\text{OCS}^+ \rightarrow \text{CO}^+ + \text{S}$, $\text{CO} + \text{S}^+$, $\text{O}^+ + \text{CS}$, or $\text{O} + \text{CS}^+$. In addition, OCS molecules have larger polarizability than CO and HCl molecules have. Therefore, the effects of the Stark shift on the tunnel ionization dynamics could be significant (see table 1.1) [61]. Observing the angular-dependent ionization rates correlated with these dissociation events, we study the correlation dynamics how these dissociation paths affect the asymmetry in the MF-PAD.

1.3 Contents of this thesis

This thesis is organized as follows: In chapter 2, we introduce theoretical backgrounds of strong-field interaction described quantum mechanically. In chapter 3, we show the experiment results on the subject of high-order harmonics generated from aligned molecules with carrier-envelope-phase stabilized pulses. In Chapter 4, we show the experiment results on the subject of coincidence study of tunnel ionization dynamics in OCS molecules. These two chapters independently have four sections which presents the details of our experimental setups and techniques (section 3.1 and section 4.1), show the results of these experiments (section 3.2 and section 4.2), discuss the origins of the results (section 3.3 and section 4.3), and summarize the results (section 3.4 and section 4.4), respectively. In chapter 5, we conclude this thesis.

Chapter 2

Theoretical background

In this chapter we introduce theoretical backgrounds of strong field interaction described quantum mechanically. Keldysh have released his theory on the strong-field interaction [63], and the theory have been an important basis of modern theory of nonlinear ionization [64]. Among a number of approaches the strong-field approximation (SFA) is widely used by experimentalists and theorists because the strong-field approximation offers not only intuitive descriptions of the strong-field phenomena but also quantitative results with low computational costs. The SFA model, known as the Lewenstein model, is a successful case, which reproduced the description of the three-step model [65]. For another case, the SFA is applied to calculate ionization rates. In the following section, we introduce several theoretical treatments of tunnel ionization and high-order harmonic generation.

2.1 Strong field ionization

2.1.1 Atomic tunneling theory

In 1986, Ammosov, Delone and Krainov published their work on the formulation of the tunneling rate for general atoms when the Keldysh parameter satisfies $\gamma_{\text{Keldysh}} \ll 1$, known as “ADK theory” [66]. In the case of a linearly polarized field the ionization rate of an s-state atom is given by [64]

$$\Gamma_{ADK}^{\text{linear}} = \sqrt{\frac{2n^{*3}F}{\pi Z^3}} \frac{FD^2}{8\pi Z} \exp\left(-\frac{2Z^2}{3n^{*3}F}\right) \quad (2.1)$$

where D is given by

$$D = \left(\frac{4eZ^3}{Fn^{*4}}\right)^{n^*}, \quad (2.2)$$

and Z is the charge of the ion left behind, and n^* is the effective principal quantum number given by

$$n^* = \frac{Z}{\sqrt{2I_p}} \quad (2.3)$$

where I_p is the ionization potential. In the case of a circularly polarized field the ionization rate of an s-state atom is given by [64]

$$\Gamma_{ADK}^{\text{circular}} = \frac{FD^2}{8\pi Z} \exp\left(-\frac{2Z^3}{3n^{*3}F}\right). \quad (2.4)$$

It is worth noting that averaging over the magnetic quantum numbers of a considered atom the result for the ionization rate coincides with eq.(2.1), or eq.(2.4). These expressions are applicable when the laser field strength is smaller than the atomic electric field strength [64]:

$$F_{\text{BSI}} = \frac{I_p}{4Z}, \quad (2.5)$$

where Z is the charge of the atomic core.

The expression for the rate of tunnel ionization as a function of electron momentum \mathbf{p} is given by [64]

$$w(p_{\parallel}, p_{\perp}) = w(0) \exp\left[-\frac{p_{\parallel}^2 \omega^2 (2I_p)^{3/2}}{3F^3} - \frac{p_{\perp}^2 (2I_p)^{1/2}}{F}\right], \quad (2.6)$$

where p_{\parallel} and p_{\perp} are the components of electron momentum along and normal to the axis of polarization of laser field, respectively. In the case of circularly polarized field, The expression for the rate of tunnel ionization as a function of electron momentum \mathbf{p} is given by [67, 7]

$$w(p_{\parallel}) = w(0) \exp\left\{\left[-2[2I_p + (p_{\parallel} - F/\omega)^2]^{3/2} + 2(2I_p)^{3/2}\right](3F)^{-1}\right\}. \quad (2.7)$$

The maximum value of the ionization rate takes place at non-zero energy:

$$E_{\parallel} \approx \frac{F^2}{2\omega^2}; \quad E_{\perp} = 0, \quad (2.8)$$

where $E_{\parallel(\perp)} = p_{\parallel(\perp)}^2/2$.

These theoretical predictions were experimentally examined by using a CO₂-laser of wavelength 10 μm to ionize He atoms or Xe atoms, in which the values of the Keldysh parameter is $\gamma_{\text{Keldysh}} \approx 0.01$ [67, 68, 69]. Their results of the ionization yields as a function of the laser intensity are in good agreement with the predictions of the ADK theory [68]. Corkum *et al.* observed the electron energy spectrum for the ionization of Xe atoms by a linearly polarized laser pulses [67], and Mohideen *et al.* observed the electron energy spectrum for the ionization of He atoms by a circularly polarized pulses [69]. The both results are in good agreement with the predictions of the ADK theory.

2.1.2 Molecular tunneling theory

The calculations of the tunneling rates of molecules in electric fields are more difficult tasks than those of atoms in electric fields because molecules in electric fields, in general, do not have any symmetries.

There are several approaches to calculating the ionization rates of molecules in arbitrary oriented electric fields. A straight-forward method is a first-principle calculation, for example, using density-functional theory (DFT) [53] [70] [71]. They calculated the eigen energies of Gamow state by complex number where the ionization rates were obtained from the imaginary parts. It gives highly accurate values of ionization rates; however, its computational cost and calculation techniques prevent, in particular, experimentalists from applying the method to compare their results and calculations. Therefore, an accurate approximated model or an analytical model for the molecular ionization is highly demanded. One of those is an extension of the ADK theory, known as the molecular-orbital ADK theory (MO-ADK theory) [41]. The theory gives analytical values of the ionization rates, and an intuitive description of ionization that the angular-dependent ionization rate maps the electron density profile of the ionized molecular orbitals. More recently, a collaborated group of Russia, Japan, and Denmark has developed a new approach, called the weak-field asymptotic theory (WFAT), to calculating the tunneling rates utilizing Siegert states [50]. Those studies have shown that the tunnel ionization rates of molecules depend crucially on their highest occupied molecular orbitals (HOMOs) [41, 53, 50]. In the following sections, we introduce the two different theories, MO-ADK theory and WFAT.

MO-ADK theory

The MO-ADK theory is an extension of the ADK theory to molecules [41]. Therefore, it is based on the same assumptions as the ADK theory, and it does not include the many-electron effects [41]. Nevertheless, it provides a new insight into the ionization dynamics of molecules.

The asymptotic wave function of a HOMO of a molecule at large distances in the molecular frame is given by [41]

$$\Psi^m(\mathbf{r}) = \sum C_l F_l(r) Y_{lm}(\mathbf{r}), \quad (2.9)$$

$$\Psi^m(\mathbf{r}) \approx r^{Z/\kappa-1} \exp(-\kappa r) \sum_l C_l Y_{lm}(\mathbf{r}) \quad (2.10)$$

where m the magnetic quantum number, and l the angular quantum number. The coefficient C_l is calculated by fitting equation (2.10) to calculated wave function of HOMO. Several values for C_l are given in Ref. [72].

The ionization rate is given by [41]

$$\Gamma_{\text{MO-ADK}}(\mathbf{F}) = \frac{1}{\kappa^{2Z/\kappa-1}} \exp\left(-\frac{2\kappa^2}{3F}\right) \sum_{m'} \frac{B^2(m')}{2^{|m'|} |m'|!} \left(\frac{2\kappa^3}{F}\right)^{(2Z/\kappa)-|m'|-1} \quad (2.11)$$

where $B(m')$ represent orientation dependence of the ionization, and given by

$$B(m') = \sum_l C_{lm} D_{m'm}^l(\mathbf{F}) Q(l, m). \quad (2.12)$$

$Q(l, m)$ is given by

$$Q(l, m) = (-1)^{(|m|-m)/2} \sqrt{\frac{2l+1}{2} \frac{(l+|m|)!}{(l-|m|)!}} \quad (2.13)$$

WFAT

Tolstikhin *et al.* made another approach to calculate ionization rates of molecules [50]. This is different from theories on the basis of the quasi-static approximation such as MO-ADK theory [41]. The “weak” means that the ionization occurs by tunneling of an electron through a potential barrier. On the other hand, when the electric field is sufficiently strong, the electron can escape from the potential through a classically accessible window, which is termed as over-barrier regime. The two regime can be separated by the atomic electric field strength (eq. (2.5)). They constructed Siegert states, which are the regular solutions to the stationary Schrödinger equation under the outgoing-wave boundary conditions. Using parabolic coordinates:

$$\xi = r + z, \quad 0 \leq \xi < \infty \quad (2.14)$$

$$\eta = r - z \quad 0 \leq \eta < \infty \quad (2.15)$$

$$\phi = \arctan \frac{y}{x}, \quad 0 \leq \phi < 2\pi, \quad (2.16)$$

the stationary Schrödinger equation for the electron in the static electric field is given by [50]

$$\left[\frac{\partial}{\partial \eta} \eta \frac{\partial}{\partial \eta} + \beta(\eta) + \frac{E\eta}{2} + \frac{E\eta^2}{4} \right] \psi(\mathbf{r}) = 0, \quad (2.17)$$

where

$$B(\eta) = \frac{\partial}{\partial \xi} \xi \frac{\partial}{\partial \xi} + \frac{\xi + \eta}{4\xi\eta} \frac{\partial^2}{\partial \phi^2} - rV(\mathbf{r}) + \frac{E\xi}{2} - \frac{F\xi^2}{4}. \quad (2.18)$$

They found the solution in the form

$$\psi(\mathbf{r}) = \eta^{-1/2} \sum_{\nu} f_{\nu}(\eta) \Phi_{\nu}(\xi, \phi; \eta), \quad (2.19)$$

with the engenvalue E:

$$E = \varepsilon - \frac{i}{2}\Gamma, \quad (2.20)$$

where Γ represents the ionization rate.

Later, Madsen *et al.* describe the ionization derived from WFAT as [73]

$$\Gamma_{\text{WFAT}}(\beta) = \sum_{n_\xi} \sum_m \Gamma_{n_\xi m}(\beta) + O(\Gamma^2) \quad (2.21)$$

$$\Gamma_{n_\xi m}(\beta) = |G_{n_\xi m}(\beta)|^2 W_{n_\xi m}(F) [1 + O(F)] \quad (2.22)$$

$$W_{n_\xi m}(F) = \frac{\kappa}{2} \left(\frac{2\kappa^2}{F} \right)^{2Z/\kappa - 2n_\xi - |m| - 1} \exp\left(-\frac{2\kappa^3}{3F}\right) \quad (2.23)$$

$$G_{n_\xi m}(\beta) = i^p \sum_{l=|M-m|} C_{n_\xi m}^{(l)} \Theta_{l|M-m}(\beta) \quad (2.24)$$

$$\Theta_{lm}(\beta) = \sqrt{\frac{(2l+1)(l-m)!}{2(l+m)!}} P_l^m(\cos \beta), \quad (2.25)$$

where n_ξ and m are parabolic quantum numbers, $\Gamma_{n_\xi m}$ is the structure factor, $W_{n_\xi m}(F)$ is the field factor, $\kappa = \sqrt{2|E|}$, and Z is the charge of the ion left behind. For even states with respect to the plane including the molecular axis and the electric field, the dominant contribution is given by

$$\Gamma_{\text{WFAT}}^{\text{even}}(\beta) \approx |G_{00}(\beta)|^2 W_{00}(F). \quad (2.26)$$

For odd states the dominant contribution is given by

$$\Gamma_{\text{WFAT}}^{\text{odd}}(\beta) \approx |G_{01}(\beta)|^2 W_{01}(F). \quad (2.27)$$

In these cases, the structure factors are simplified as

$$G_{00}(\beta) = \sum_{l=1} C_{00}^{(l)} \Theta_{l1}(\beta) \quad (2.28)$$

$$G_{01}(\beta) = \sum_{l=0} C_{01}^{(l)} \Theta_{l0}(\beta). \quad (2.29)$$

The coefficients $C_{00}^{(l)}$ and $C_{01}^{(l)}$ for OCS molecules are given in table 2.1 [73]. This formulation allows experimentalists to compare their experimental results with the predictions of WFAT. Figure 2.1 shows the two structure factors G_{00} and G_{01} for the two degenerate HOMOs in OCS of π_g symmetry, respectively. These factors have different dependence on the angle between the molecular axis and the electric field due to their symmetry of the orbitals. Note that the ionization rate is dominantly contributed from the even state, the lower left panel of figure 2.1, because the field factors in equation 2.26 and 2.27 are $W_{00}(F) \gg W_{01}$.

This theory is applicable when the following conditions are satisfied [73]:

$$F \ll F_c = \frac{I_p^2}{2|2Z - \sqrt{2}I_p(m+1)|}, \quad 1 \gg \frac{4\omega I_p}{F^2} = \frac{I_p}{\omega U_p} = 2\omega\gamma_{\text{Keldysh}}^2. \quad (2.30)$$

The first condition guarantees that the laser field amplitude is much smaller than the critical field for a given state $(0, m)$. The second condition validates the adiabatic approximation [74], where an oscillating laser field $F(t)$ is treated as a static electric field.

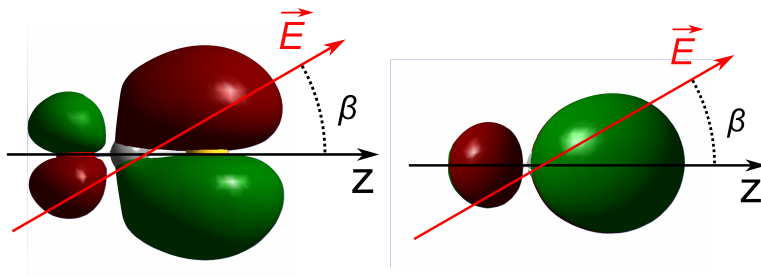
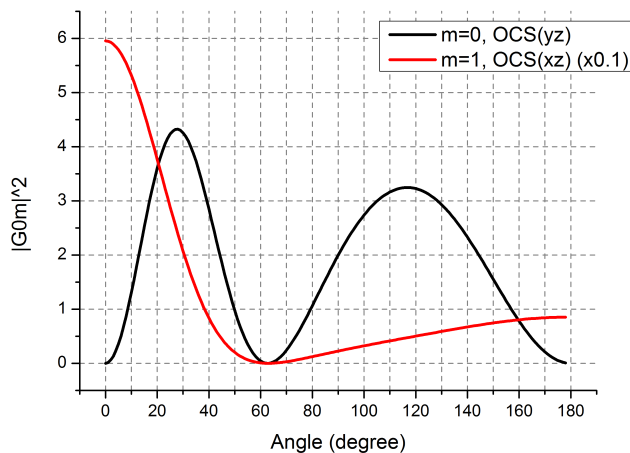


Figure 2.1: Top: The magnitude of the structure factors for the two degenerate HOMOs in OCS of π_g symmetry as a function of the angle β between the internuclear axis and the electric field. Bottom: The configurations of the inter-nuclear axis and electric field for G_{00} (left) and G_{01} (right). The O atom is on the negative axis in the molecular fixed frame.

Under an experimental condition with OCS molecules ($I_p = 11.174$ eV): the wavelength of 800 nm, the laser intensity is 1×10^{14} W/cm², the angular frequency ω is 0.057 a.u., the electric field strength F is 0.0534 a.u., and the Keldysh parameter γ_{Keldysh} is 0.967. In this case, the both conditions are satisfied because $F/F_c = 0.69$ and $2\omega\gamma_{\text{Keldysh}}^2 = 0.11$.

2.2 High-order harmonic generation

The semiclassical model provides an intuitive mechanism of high-order harmonic generation; however, it does not give the amplitude and phase of the radiation. In 1993, Lewenstein *et al.* quantum mechanically described the high-order harmonic generation using the single active electron approximation and the strong field approximation. The Schrödinger equation for atoms containing many electrons (even for He) is very difficult to solve analytically; therefore, they assume that only one electron in the atom responds to the external field. The Schrödinger equation for the atom in the laser field $E(t)$ is

Table 2.1: Structure coefficients for the HOMO of OCS of π symmetry [73]. $a[b] = a \times 10^b$.

l	$C_{00}^{(l)}[\text{OCS}]$	$C_{01}^{(l)}[\text{OCS}]$
0		-0.762
1	-1.093	3.038
2	1.470	1.471
3	0.690	0.757
4	0.352	0.268
5	0.123	0.759[-1]
6	0.340[-1]	0.164[-1]
7	0.749[-2]	0.147[-2]
8	0.105[-2]	
9	-0.317[-3]	

given by

$$i \frac{\partial}{\partial t} |\Psi(t)\rangle = \left[-\frac{1}{2} \nabla^2 + V(\mathbf{r}) - \mathbf{E} \cdot \mathbf{x} \right] |\Psi(t)\rangle, \quad (2.31)$$

where \mathbf{x} is the position of the electron. The resultant oscillation of the electric dipole moment generates high-order harmonics.

Lewenstein *et al* introduced the following approximation: (i) As the bound state, only the ground state $|0\rangle$ is considered and the contributions from all other bound states are neglected. (ii) The depletion of the ground state by ionization is neglected. (iii) In the continuum state, the electron does not influenced by the Coulomb potential of the parent ion, and treated as a plane wave. Under these approximation the differential equation can be integrated as [65, 75]

$$|\Psi(t)\rangle = e^{iI_p t} |0\rangle + \int d^3 p' e^{iI_p t} b(\mathbf{p}, t) |\mathbf{p}'\rangle, \quad (2.32)$$

$$b(\mathbf{p}, t) = i \int_{t_0}^t dt' \mathbf{E}(t') \mathbf{d} \left(\mathbf{p} - \int_{t'}^t \mathbf{E}(s) ds \right) \exp \left[-i \int_{t'}^t \left(\frac{\left(\mathbf{p} - \int_{t''}^t \mathbf{E}(s) ds \right)^2}{2} + I_p \right) dt'' \right], \quad (2.33)$$

where $|\mathbf{p}\rangle$ is the continuum state wave function with momentum \mathbf{p} , I_p is the ionization potential of the atom or molecule and

$$\mathbf{d}(\mathbf{p}) \equiv \langle \mathbf{p} | \mathbf{x} | 0 \rangle = (2\pi)^{-3/2} \int_{\infty}^{\infty} d^3 \mathbf{x} e^{-i\mathbf{p}\mathbf{x}} \mathbf{x} \langle \mathbf{x} | 0 \rangle \quad (2.34)$$

is the bound-free transition dipole. Neglecting continuum-continuum transition, the dipole moment $\mathbf{x}(t) \equiv \langle \Psi(t) | \mathbf{x} | \Psi(t) \rangle$ is given by [65, 75]

$$\mathbf{x}(t) = i \int d^3 \mathbf{p} \int_{t_0}^t dt' |\mathbf{E}(t') \mathbf{d}(\mathbf{p} - \mathbf{A}(t')) \exp[-iS(\mathbf{p}, t, t')] d^*(\mathbf{p} - \mathbf{A}(t)) + c.c., \quad (2.35)$$

where $A(t)$ is the vector potential:

$$A(t) = - \int_0^t dt' \mathbf{E}(t'), \quad (2.36)$$

and $S(\mathbf{p}, t, t')$ are given by

$$S(\mathbf{p}, t, t') = \int_{t'}^t \left[\frac{(\mathbf{p} - \mathbf{A}(t''))^2}{2} + I_p \right] dt''. \quad (2.37)$$

According to the classical electrodynamics theory, the electric field emitted from the dipole is given by [76]

$$E(t, \mathbf{r}, \theta) = \frac{d_0 \omega^2}{4\pi\epsilon_0 c^2} \frac{\sin \theta}{\mathbf{r}} e^{i\omega(t - \frac{r}{c})}, \quad (2.38)$$

where ϵ is the electric permittivity of vacuum, c is the speed of light in vacuum, θ is angle between the axis of the dipole and the \mathbf{r} vector, and d_0 is the amplitude of dipole moment. Therefore, the electric field of high-order harmonics $E_{\text{HH}, z}(t)$ radiated from the oscillation the calculated dipole \mathbf{x} can be expressed as [75]

$$E_{\text{HH}, z}(t) \propto \ddot{x}_z(t - D/c), \quad (2.39)$$

where D is the distance from the electron to the detector and c is the speed of light. Fourier transform of the electric field $E_{\text{HH}, z}(t)$ is given by

$$\tilde{E}_{\text{HH}, z}(\omega) \equiv \int_{-\infty}^{\infty} dt e^{i\omega t} E_{\text{HH}, z}(t) \propto \int_{-\infty}^{\infty} dt \ddot{x}_z(t - D/c) \propto \int_{-\infty}^{\infty} dt \ddot{x}_z(t). \quad (2.40)$$

Assuming the envelope of laser pulses varies slowly enough and the degree of ionization is negligible, we obtain a useful expression [75] :

$$\tilde{E}_{\text{HH}, z}(\omega) \propto \omega^2 \tilde{x}_z(\omega), \quad (2.41)$$

where $\tilde{x}_z(\omega)$ is the Fourier transform of $x_z(t)$.

Chapter 3

High-order harmonics generated from aligned molecules with carrier-envelope-phase stabilized pulses

3.1 Experiment

Figure 3.1 shows the experimental setup. An output from a CEP-stabilized Ti:sapphire based chirped pulse amplification system (FEMTOLASERS, FEMTOPOWER PRO V CEP) has the center wavelength of 800 nm and is split into two pulses [77],[78]. One is used as a 100-fs pump pulse to induce nonadiabatic molecular alignment and the other is used as a probe pulse to generate high-order harmonics. A portion of the pump pulse is used to measure the relative value of the CEP of the pulse with an f -to- $2f$ interferometer, which is fed back to the amplification system to stabilize it. The probe pulse is compressed down to 10 fs with the center wavelength of 770 nm, measured by the SPIDER technique.

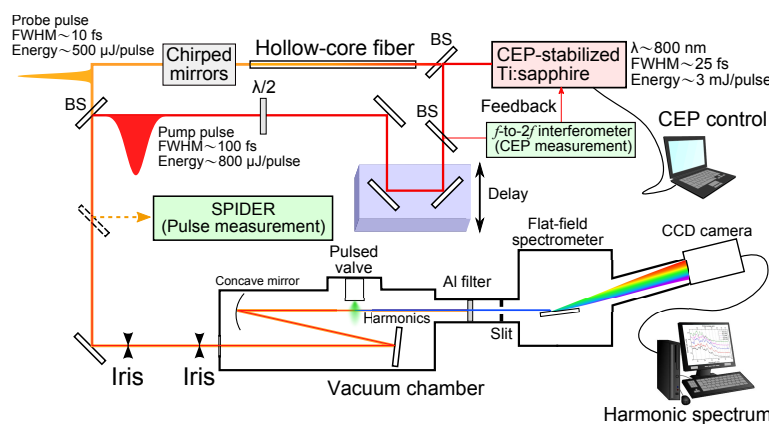


Figure 3.1: Experimental setup. See texts for detail.

The pump and probe pulses collinearly enter the vacuum chamber and are focused by a 300-mm-focal-length spherical concave mirror into a supersonic molecular beam supplied by a pulsed valve. The generated harmonics are spectrally resolved by a flat-field vacuum spectrometer and detected by an x-ray CCD camera. When aligned CO₂ and N₂ molecules are used as a sample, the delay times between the pump and the probe pulses are set at 20.9 and 4.1 ps, respectively, corresponding to the half revivals of nonadiabatic alignment of the sample molecules.

3.1.1 Laser

Our CPA laser systems employing Ti:sapphire for the oscillator and amplifying medium are supplied by FEMTOLASERS. The oscillator is a Kerr-lens mode (KLM) locked Ti:sapphire laser, and can generate a ultrashort pulse with its CEP stabilized by controlling the offset frequency f_o of the pulse. Fluctuations of the CEP during the amplification stage is compensated by a feed-back loop system. This section describes important mechanisms such as KLM, CPA, external compression, and CEP stabilization).

Kerr-lens mode locking

We use Titanium doped Sapphire crystal (Ti³⁺:Al₂O₃). It has advantages that it has broad gain bandwidth (400-600 nm) and it allows one to exploit Kerr-lens mode locking to produce a few cycle pulse. The optical Kerr-effect of the Ti:Sapphire crystal offers an intensity dependent diffraction index:

$$n(\omega, I(r, t)) = n_1(\omega) + n_2(\omega)I(r, t). \quad (3.1)$$

The response time of the intensity dependence of the diffraction is very fast (a few femtoseconds) because this effect is generally due to a hyper-polarizability of a solid medium. Given a Gaussian transverse intensity profile (TEM₀₀), the can be interpreted as a introduction as a spherical lens in the medium by the optical Kerr effect (figure 3.2). The resonator in the oscillator is optimized in such a way that the Kerr effect results in a better overlap with the pump beam (soft aperture). The KLM can be started by inducing a small but rapid change in the resonator length [79].

CPA system

Harmonic generation requires several mJ ultra short pulses; therefore a pulse from the Ti:sapphire oscillator need a further amplification. We use a chirped pulse amplification system to obtain several mJ with 25 fs duration pulses. The short pulse from the oscillator is stretched with blocks of fused silica. The stretched pulse gain energy by passing other

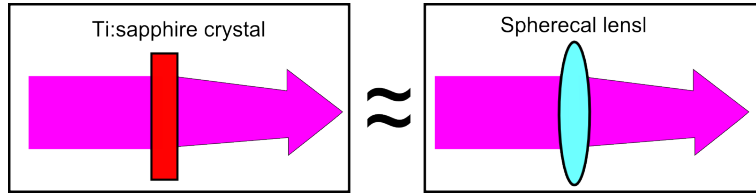


Figure 3.2: Schematic diagram of the Kerr lens effect. When a TEM_{00} pulse propagate in a Ti:sapphire crystal, the crystal works as a spherical lens.

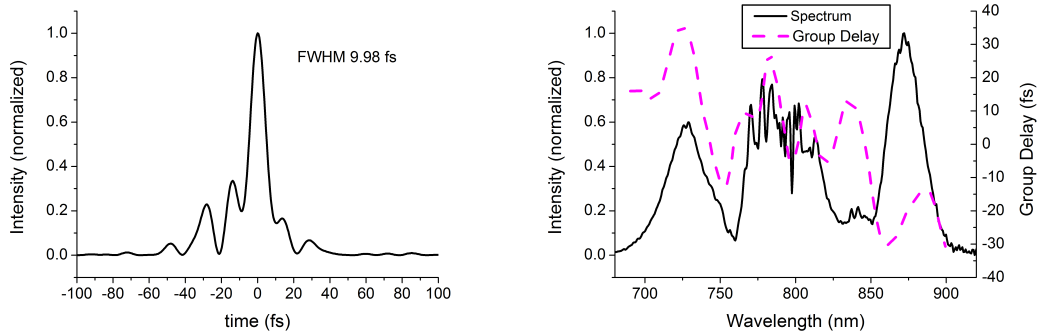


Figure 3.3: Left: the shape of the laser pulse measured by a SPIDER. The full width at half maximum (FWHM) is measured to be 9.98 fs. Right: the power spectrum (black solid line) and the group delay (pink dashed line) of the pulse.

Ti:sapphire crystals pumped with Nd:YAG laser 12 times. Before leaving the CPA system, the pulse is compressed by a pair of gratings down to 25 fs.

External compression

In order to temporally shorten the duration of the laser pulse, the probe pulse is introduced into a 0.25-mm-diam hollow-core fiber filled with 2 bars Ne and gets linearly chirped and spectrally broadened by the self-phase modulation (SPM) during the propagation of 1 meter in the fiber [80, 81]. The mechanism of SPM is that the refractive index is dependent of the laser intensity. For 25 fs pulses the intensity modulation is so large that it causes spectrum broadening. The spectrally-broadened pulse is compressed down to 10 fs using two sets of chirped mirrors with 8-bounces in each set, one of which is placed just after the hollow-core fiber and the other near the vacuum chamber [82]. Figure 3.3 shows the pulse shape and its spectrum and group delay measured by the SPIDER technique [83, 84].

CEP stabilization

The spectrum of the pulse generated from the oscillator is not a continuum, it has many longitudinal modes spaced by the repetition rate, $f_{\text{rep}} \sim 100$ MHz. A number of these

longitudinal modes in a resonator are phase locked such that they constructively interfere to form a Fourier transform limited pulse as a result of the mode locking. These modes can be expressed as

$$f_n = n f_{\text{rep}} + f_o \quad (3.2)$$

$$f_{\text{rep}} = \frac{c}{2L} \quad (3.3)$$

where f_{rep} is a repetition frequency, f_o is an offset frequency satisfying $0 < f_o < f_{\text{rep}}$, and L is the cavity length. The electric field is given by the Fourier transform of them:

$$F(t) = \sum_n F_n \cos [2\pi(n \cdot f_{\text{rep}} + f_o)t + \phi_{\text{CEP}}], \quad (3.4)$$

If the offset frequency is f_{rep}/N , we obtain the relation

$$F\left(t + \frac{N}{f_{\text{rep}}}\right) = F(t), \quad (3.5)$$

meaning that the exact same pulse is reproduced every N pulses. Therefore, locking of the offset frequency f_o is a key to stabilizing the CEP. In our system, the N is set at 4. The offset frequency can be measured by observing the interference between the broadened spectrum $F^{\text{SPM}}(\omega)$ by self-phase modulation (SPM) and the spectrum $F^{\text{DIF}}(\omega)$ by different-frequency generation (DFG), because the different-frequency generation renders the longitudinal modes f_n^{DIF} free from the offset frequency f_o [85, 86],

$$f_n^{\text{DIF}} = n \cdot f_{\text{rep}}. \quad (3.6)$$

These pulses are generated by focusing a pulse from the Ti:sapphire oscillator into a periodically poled magnesium-oxide-doped lithium niobate (PP-MgO:LN) in which DFG and SPM occur at the same time [77]. An avalanche photodiode observes the beat due to the interference of the electric fields:

$$F(t) = F^{\text{SPM}}(t) + F^{\text{DIF}}(t) \quad (3.7)$$

$$= \sum_n F_n^{\text{SPM}} \cos [2\pi f_n t + \phi_n^{\text{SPM}}] + F_n^{\text{DIF}} [2\pi f_n^{\text{DIF}} t + \phi_n^{\text{DIF}}]. \quad (3.8)$$

$$(3.9)$$

The cross terms of $F^2(t)$ are written as

$$\sum_n F_n^{\text{SPM}} F_n^{\text{DIF}} \cos [2\pi f_o t + \phi_n^{\text{DIF}} - \phi_n^{\text{SPM}}], \quad (3.10)$$

where we omit terms which oscillate faster than f_{rep} . The equation (3.10) says that the beat frequency which oscillates slower than f_{rep} corresponds to the offset frequency¹. On

¹The phase deviations caused by $\phi_n^{\text{DIF}} - \phi_n^{\text{SPM}}$ in equation (3.10) do not affect this conclusion because $a \cos(f_o t) + b \cos(f_o t + \alpha) = c \cos(f_o t + \beta)$.

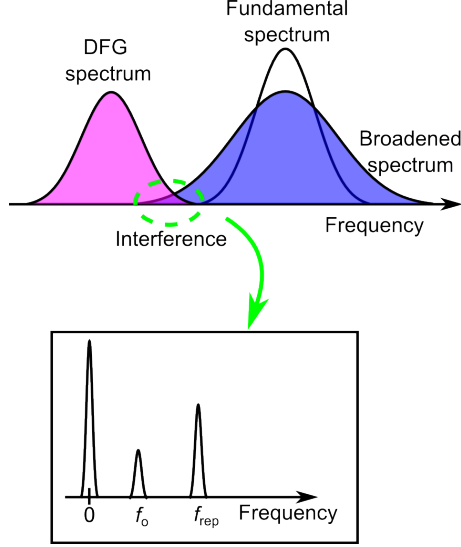


Figure 3.4: Schematic diagram of the measurement technique of the offset frequency. The upper figure shows broadened spectrum of the fundamental spectrum and different-frequency spectrum of the fundamental spectrum. The two spectra partially overlap in the region indicated by the dashed circle. The lower figure shows the Fourier amplitude of the beat signal of the interference region.

the other hand, the control of the offset frequency f_o can be accomplished by varying the pump laser intensity and the path length in a fused-silica glass wedge [87].

After the amplification stage, we observe the value of the relative value of the CEP with a f -to- $2f$ interferometer. The spectrum of the pulse from the amplifier is treated as a continuous one because the repetition frequency is very small $f_{\text{rep}} = 1$ kHz. The pulse is focused into a sapphire plate to induce self-phase modulation. As a result, the spectrum is broadened spanning a octave. The second harmonic of the lower frequency component of the pulse are generated by focusing the pulse into a BBO crystal. In the frequency domain, the electric fields of the two pulses are produced:

$$F^{\text{SPM}}(\omega) = \sqrt{I^{\text{SPM}}(\omega)} e^{i\phi^{\text{SPM}}(\omega) + i\phi_{\text{CEP}}} \quad (3.11)$$

$$F^{\text{SH}}(\omega) = \sqrt{I^{\text{SH}}(\omega)} e^{i\phi^{\text{SH}}(\omega) + i\phi_{\text{CEP}} + \omega\tau}, \quad (3.12)$$

where I^{SPM} and I^{SH} are the intensities of the fundamental pulse and the second harmonic of the low frequency component of the fundamental pulse, τ is the delay between the two pulses. The interference can be written as

$$S(\omega) \propto |E^{\text{SPM}}(\omega) + E^{\text{SH}}(\omega)|^2 \quad (3.13)$$

$$= I^{\text{SPM}} + I^{\text{SH}} + 2\sqrt{I^{\text{SPM}}I^{\text{SH}}} \cos[\omega\tau + \phi^{\text{SH}}(\omega) - \phi^{\text{SPM}}(\omega) + \phi_{\text{CEP}}]. \quad (3.14)$$

The relative value of the CEP ϕ_{CEP} can be extracted from the interference pattern by Fourier transform spectral interferometry. The CEP drift caused in the amplification

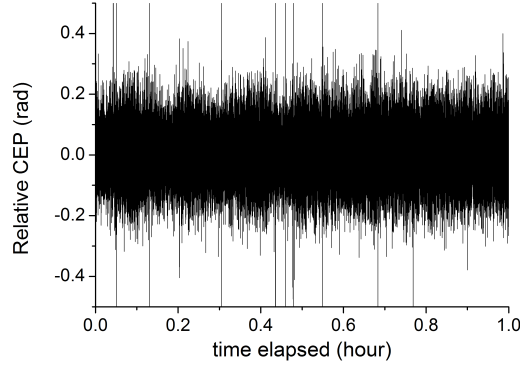


Figure 3.5: 1-hour measurement of the CEP with a feed-back loop.

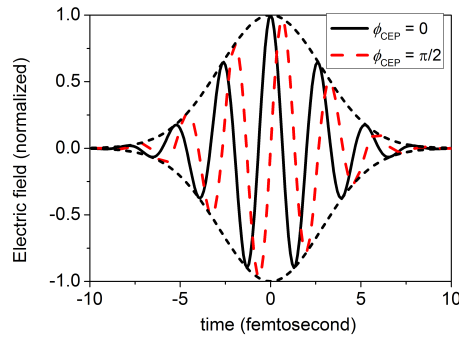


Figure 3.6: A schematic diagram of the electric field of few-cycle pulses with different values of the CEP.

stage is compensated by varying the path length in a fused-silica glass wedge incorporated into the laser pulse [87].

Figure 3.5 shows the result of a 1-hour measurement of the relative CEP with the feed-back loop. The CEP drift is measured to be within 0.2 rad with a few events where the CEP suddenly changes due to experimental errors.

When the spectrum intensity is Gaussian shaped, and replacing $\sum_n E_n$ and $n \cdot f_{\text{rep}} + f_o$ with $\int d\omega E(\omega)$ and ω , respectively, we obtain

$$E(t) = \int d\omega E_0 e^{\frac{\omega^2}{2\omega_0^2}} e^{i(\omega t + \phi_{\text{CEP}})} + \text{c.c.}, \quad (3.15)$$

$$= \omega_0 \sqrt{2\pi} e^{\frac{\omega_0^2}{2} t^2} e^{-i\phi_{\text{CEP}}} + \text{c.c.}. \quad (3.16)$$

The equation explains how the phase ϕ_{CEP} changes the shape of the electric field within the intensity envelope. Figure 3.6 shows the electric field of few-cycle pulses with different values of the CEP.

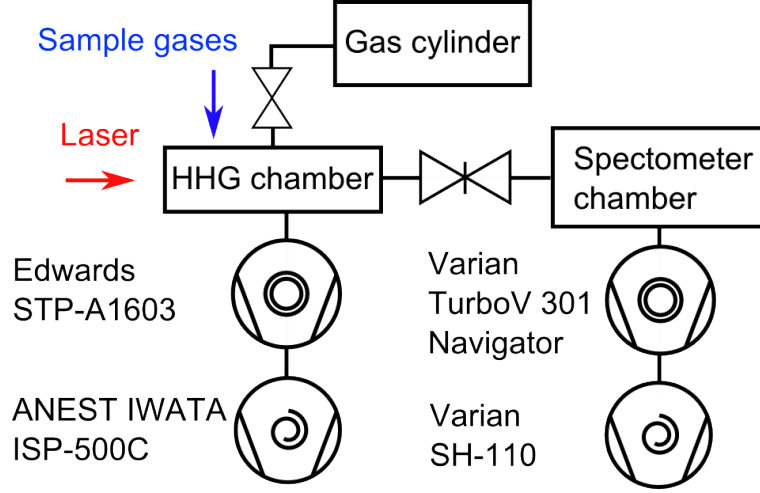


Figure 3.7: Schematic diagram of the vacuum system of the HHG experiment. Vacuum symbols are found in figure 1.

3.1.2 Vacuum system

Since harmonics have their spectral range in the XUV region, air absorbs harmonics. Therefore, harmonics should be generated and detected in a vacuum chamber. Figure 3.7 shows the vacuum system in our experiment. The HHG chamber is evacuated and maintains a vacuum pressure of 10^{-2} Pa during the injection of the gas jet by a turbo molecular pump (Edwards, STP-A1603C, 1600 L/s) backed by a dry scroll pump (ANEST IWATA, ISP-500C, 500 L/min). The spectrometer chamber is evacuated to achieve a pressure of 10^{-6} Pa by a turbo molecular pump (Varian, Turbo-V 301 Navigator, 250 L/s) backed by a dry scroll pump (Varian, SH-110, 90 L/min).

3.1.3 Optics

Because the pulses we use have broad band spectrum ($\Delta\lambda \sim 200$ nm), special cares to the group delay caused by optical components have to be taken. In particular, the lens stretches the pulse by giving different group delays to the pulse propagating through the lens center relative to the pulse propagating along the peripheral region (chromatic aberration). To avoid the chromatic aberration, we use a concave mirror to focus the pulses. Since the concave mirror is not parabolic one but spherical one with a curvature R , it may cause a time delay ΔT of the pulse depending on the position r off-axis (spherical aberration). The spherical aberration can be evaluated using geometrical optics, which is given by [3]

$$\Delta T = \frac{3R}{4c} \left(\frac{r}{R} \right), \quad (3.17)$$

where c is the speed of light in vacuum. Under our experimental condition, $r < 5$ mm, $R = 600$ mm, the delay is $\Delta T < 0.01$ fs, which is much smaller than the optical period of the laser $\tau_{\text{op}} \sim 2.7$ fs. Therefore, the effects of aberration can be neglected in our experiment.

When generating high-order harmonics, the phase-matching condition for high-order harmonics is very important because the characteristics of high-order harmonics are sensitive to the phase-matching condition [88, 89]. We extract the high-order harmonics generated from the short trajectories using the following procedure. First, the laser focus is set at a few millimeter before the gas jet, which makes the major contributions from the short trajectories [88, 89]. Second, the generated harmonics pass through a 1 mm slit, exploiting the fact that the harmonics that are generated from the long trajectories have a larger divergence than those from the short trajectories.

The timing between the pump pulse and the probe pulse is controlled with a delay stage set in the path of the pump pulse. The driver of the pump pulse is controlled with a TTL signal from an ANDOR PC. The overlap between the two pulses is achieved approximately by observing the interference fringes projected on a paper. To achieve better overlap, we carefully rotate a mirror such that the intensity of the harmonics increases due to the interference of the two pulses. Furthermore, we optimize the divergence of the pump pulse by adjusting a telescope placed in the path of the pump pulse such that the intensity of the harmonics increases due to the interference between the pump pulse and the probe pulse. After these procedures, we obtain good molecular alignment effects of the harmonics, as shown in the results section.

3.1.4 Chamber apparatus

Gas jet

A gas jet of samples is expanded into the HHG chamber through a pulsed valve (Parker-Hannifin, 009-1670-900) with an orifice diameter $d = 0.1$ mm and a backing pressure $P_0 = 3$ atm for generating high-harmonics. The pulsed valve is driven by a controller with a repetition rate of 100 Hz (Parker-Hannifin, IOTA-ONE). The temperature of the molecules is estimated to be ~ 60 K for N_2 molecules and $70 \sim 80$ K for CO_2 molecules [75].

Detector

The high-order harmonics are observed by a flat-field grating spectrometer (Vacuum & Optical instruments, XUV-640). An aberration-corrected concave grating with 1200 grooves per mm (Hitachi001-0640) is used in the spectrometer to spectrally resolve the HHs. The spectrally resolved HHs are detected by a charge-coupled device (CCD) camera

(Andor Technology, DO420-BN) and the acquired spectra are transferred to a personal computer through a controller card (Andor Technology, CCI-010). The CCD camera format is 1024×255 , $25 \times 25 \mu^2$. An aluminum filter (Luxel Corporation, with thickness of 1500 \AA) is placed in front of the spectrometer to suppress the fundamental and the lower-order harmonics.

3.1.5 Field-free molecular alignment

Compared to atoms, one of the most important properties of molecules is that they are anisotropic. The angular dependence affects HHG in many ways. Therefore, a molecular alignment technique is crucial to study the high-order harmonics generated from molecules. In this experiment, we exploit the laser-induced nonadiabatic alignment technique, which was first demonstrated by Rosca-Pruna and Vrakking [90]. In the following, we describe the technique [91] [92].

Using the rigid-rotor approximation where the relative positions of the atoms are frozen, the time-dependent Schrödinger equation of the nuclear wave packet is given by [91]

$$i \frac{\partial}{\partial t} |\psi(t)\rangle = (\mathbf{B}\mathbf{J}^2 + V(t)) |\psi(t)\rangle, \quad (3.18)$$

where $\mathbf{B} = 1/2I$ is the rotational constants, and $V(t)$ is the interaction potential induced by the electric field. When the molecule has a permanent dipole moment μ along the molecular axis and polarizability components α_{\parallel} and α_{\perp} parallel and perpendicular to the molecular axis, the interaction potential is given by

$$V(t) = -\mu E_0(t) \cos(\omega t) \cos \theta - \frac{1}{2} E_0^2(t) \cos^2(\omega t) (\alpha_{\parallel} \cos^2 \theta + \alpha_{\perp} \sin^2 \theta). \quad (3.19)$$

When the envelope of the electric field $E_0(t)$ changes much slower than the optical period of the laser field, the rapid oscillations are averaged over one cycle:

$$V(t) = -\frac{1}{4} E_0^2(t) (\alpha_{\parallel} \cos^2 \theta + \alpha_{\perp} \sin^2 \theta) = -\frac{1}{4} E_0^2(t) (\Delta\alpha \cos^2 \theta + \alpha_{\perp}), \quad (3.20)$$

where $\Delta\alpha = \alpha_{\parallel} - \alpha_{\perp}$. By substituting equation. () with , eq. () becomes

$$i \frac{\partial}{\partial t} |\psi(t)\rangle = (\mathbf{B}\mathbf{J}^2 - U_{\perp}(t) - U(t) \cos^2 \theta) |\psi(t)\rangle, \quad (3.21)$$

where $U_{\perp} = E_0^2(t)\alpha_{\perp}/4$ and $U(t) = E_0^2(t)\Delta\alpha$. This equation gives the dynamics of the nuclear wave packet within the rigid-rotor approximation.

Figure 3.9 and figure 3.8 show the results of integration of the equation (3.21) for CO_2 and N_2 , respectively, by using the Runge-Kutta method. The details of the calculation method (basis set, symmetries, etc.) are found elsewhere [92, 91]. The results show calculated degree of alignment $\langle \cos^2 \theta \rangle$ of a CO_2 (N_2) molecule as a function of the time

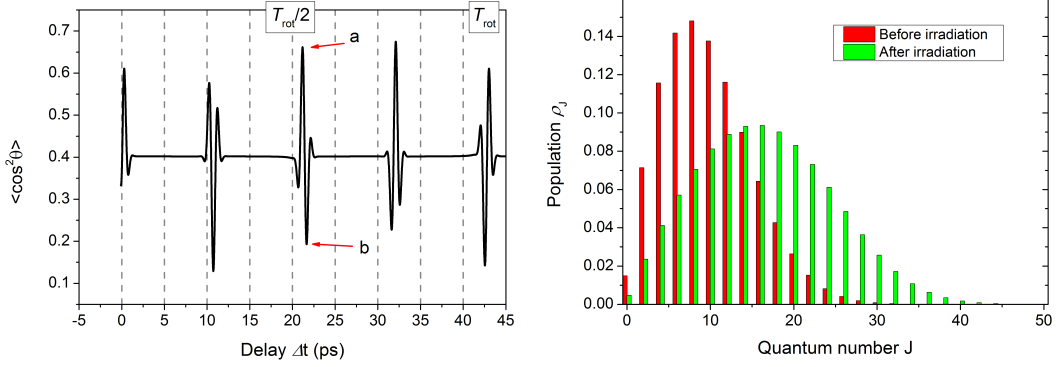


Figure 3.8: Left: Calculated degree of alignment $\langle \cos^2 \theta \rangle$ of a CO₂ molecule as a function of the time delay Δt . The laser intensity is $I = 4 \times 10^{13}$ W/cm², and the following molecular parameters are used: $B = 0.39$ cm⁻², $\alpha_{\parallel} = 4.05$ Å³, and $\alpha_{\perp} = 1.95$ Å³ [93]. Right: Populations of the rotational state with J , before and after irradiating the molecule with the pulse.

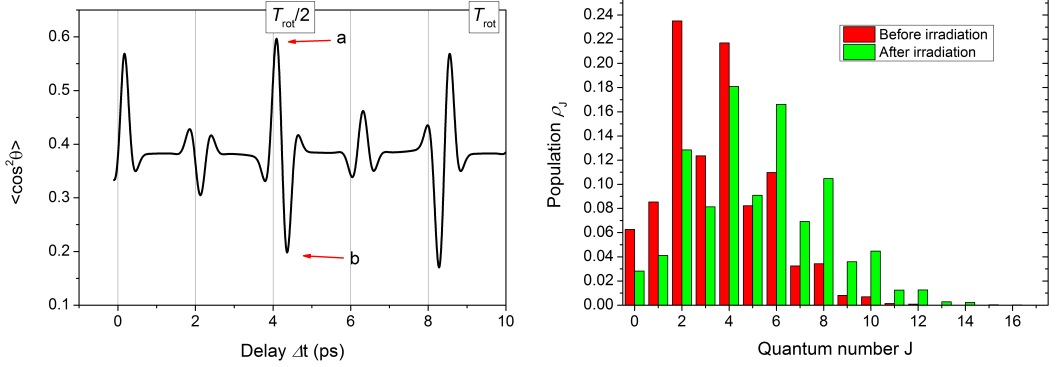


Figure 3.9: Left: Calculated degree of alignment $\langle \cos^2 \theta \rangle$ of a N₂ molecule as a function of the time delay Δt . The laser intensity is $I = 4 \times 10^{13}$ W/cm², and the following molecular parameters are used: $B = 1.99$ cm⁻², $\alpha_{\parallel} = 1.65$ Å³, and $\alpha_{\perp} = 1.00$ Å³ [94]. Right: Populations of the rotational state with J , before and after irradiating the molecule with the pulse.

delay Δt from the instant of the irradiation. The laser intensity is $I = 4 \times 10^{13}$ W/cm², which are equivalent to the estimated intensity of the pump pulse, and the following molecular parameters are used: $B = 0.39$ cm⁻² (1.99 cm⁻²), $\alpha_{\parallel} = 4.05$ Å³ (1.65 Å³), and $\alpha_{\perp} = 1.95$ Å³ (1.00 Å³) [93, 94]. Clear revivals of alignment can be seen at the time delays $\Delta t = T_{\text{rot}}/4, T_{\text{rot}}/2, 3T_{\text{rot}}/4, T_{\text{rot}}$. At around the revival delay $\Delta t = T_{\text{rot}}/2$, the degree of alignment is high at the delay indicated with a, and low at the delay indicated with b, which are called alignment and anti-alignment, respectively. In our experiment, aligned molecules are prepared in this way, and the time delay Δt is set at around the half revival delay $T_{\text{rot}}/2$. We estimate the degree of alignment is estimated to be $\langle \cos^2 \theta \rangle \sim 0.65(0.6)$ for CO₂ (N₂) molecules.

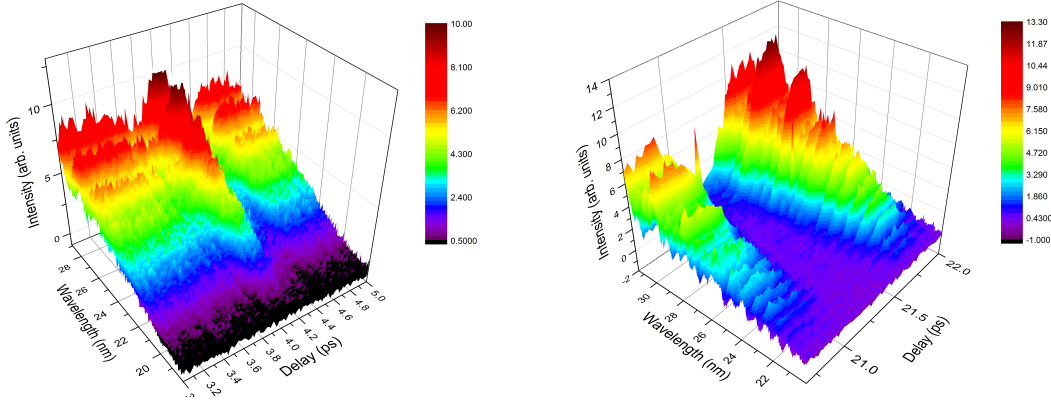


Figure 3.10: Harmonic spectra generated in N_2 (left) and CO_2 (right) as a function of the delay between the pump pulse and the probe pulse.

3.2 Results

3.2.1 Molecular alignment

Figure 3.10 shows the harmonic spectra generated from N_2 as a function of the delay between the pump pulse and the probe pulse. As explained in section 3.1.5, a femtosecond pulse excites many rotational states, and the alignment condition is then restored at a half rotational period T_{rot} after the irradiation of the molecules with the pump pulse [91]. Figure 3.10 shows that the intensity of the harmonics increases at the half revival time corresponding to half the rotational period $T_{\text{rot}} = 8.4$ ps and decreases at slightly longer delay. These intensity modulations are caused by the molecular alignment effects [95, 96]: the intensity of high-order harmonics is enhanced when the molecules are aligned along the polarization direction of the probe pulses, while it is suppressed when molecules are antialigned on the plane perpendicular to the polarization direction. Therefore, we can distinguish aligned molecules or anti-aligned molecules at these delays.

For CO_2 , the patterns of molecular alignment are almost the same as those for N_2 at around T_{rot} , but the patterns of the intensity modulation of the high-order harmonics are different because the alignment effects on the intensity of the harmonics are different from those for N_2 . At the delay corresponding to half the rotational period $T_{\text{rot}} = 42.7$ ps of CO_2 , the intensity of harmonics decreases because the harmonic generation process is suppressed due to the destructive interference [27], as shown in fig. 3.10.

In the following, We observe high-order harmonics generated with a CEP-stabilized driving pulse from the following four samples: N_2 aligned parallel to the laser polarization (parallel N_2), N_2 aligned perpendicular to the laser polarization (perpendicular N_2), CO_2 aligned parallel to the laser polarization (parallel CO_2), and randomly oriented CO_2 (random CO_2). When the perpendicular configuration is employed (perpendicular N_2),

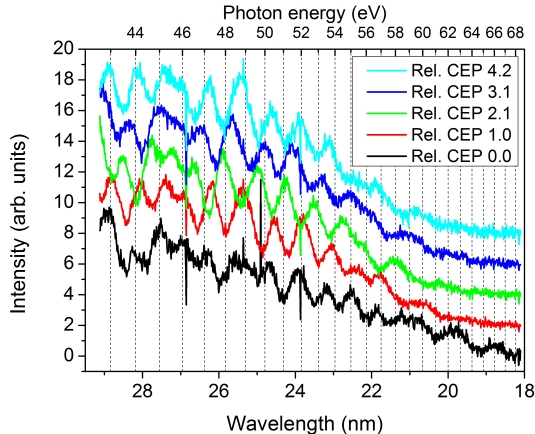


Figure 3.11: High-order harmonic spectra near the cutoff generated in parallel N_2 for different values of relative CEP from 0.0 rad to 4.2 rad. The intensity of the probe pulse is estimated to be 3×10^{14} W/cm².

the pump pulse polarization is rotated 90 degrees by using a zero-order half-wave plate.

3.2.2 CEP effects

Figure 3.11 shows high-order harmonic spectra near the cutoff generated in parallel N_2 molecules for five different values of the CEP of the driving pulse. The high-order harmonic spectra decrease gradually and are super imposed by several complex peak structures, which correspond to fringe between attosecond pulses as discussed in the following subsections. We confirm that these fringes disappear when the CEP is not locked. These characteristics of the harmonic spectra are also observed for for all kinds of samples.

We also measured high-order harmonics spectra generated in perpendicular N_2 in the same frequency region. During the measurements of those spectra generated in parallel N_2 or perpendicular N_2 , we alternately measure the harmonic spectra generated in those samples and random N_2 . In order to minimize the influence of the long-term drift of the probe pulse intensity and make the quantitative comparison of the harmonic intensities accurate as much as possible, we devised a measurement procedure of harmonic intensities. The harmonic intensity generated in aligned molecules in the parallel configuration and that from randomly aligned molecules are alternately measured. The latter sample is prepared simply by blocking the pump pulse with a mechanical shutter. Using the harmonic intensity from random N_2 as a common reference, the harmonic intensities in the two configurations are calibrated, and the result is shown in figure 3.16 (a).

Figure 3.12 shows high-order harmonic spectra near the cutoff generated in parallel CO_2 molecules for five different values of the CEP of the driving pulse. Clearly, the fringes are not clear in the spectral range around ~ 45 eV, while outside this region the fringes

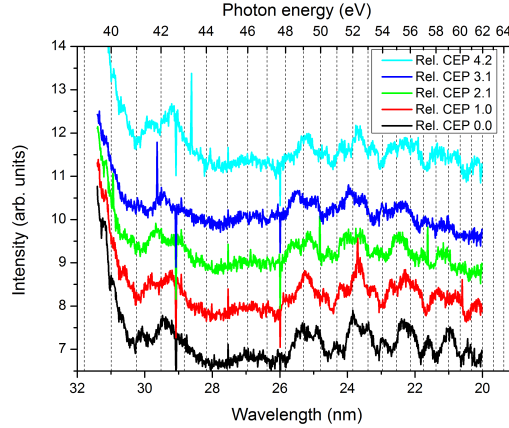


Figure 3.12: High-order harmonic spectra near the cutoff generated in parallel CO_2 for different values of relative CEP from 0.0 rad to 4.2 rad. The intensity of the probe pulse is estimated to be $3 \times 10^{14} \text{ W/cm}^2$.

are clearly observed. During the measurements of the spectra generated in parallel CO_2 , we alternately measure the harmonic spectra generated in random CO_2 . The result is shown in figure 3.17 (a).

In the following sections, we focus on the fringes and discuss their physical origin.

3.2.3 Fourier analysis

Since the observed fringes do not seem to be approximated by single sinusoidal curves, we choose Fourier analysis of the spectra rather than simply curve fitting to analyze the fringes. We follow the Fourier analysis procedure introduced by Tanaka *et al.* [97]. We weight the spectrum by multiplying it by the Hanning window to eliminate the influence of the discontinuity of the spectrum at the both ends [97]. Figure 3.13 shows the absolute values of the Fourier spectra for the HHs generated from N_2 . Figure 3.14 shows the absolute values of the Fourier spectra for the HHs generated from CO_2 . Inspection of figure 3.13 and 3.14 shows that there are at least three peaks in these Fourier spectra, specifically, at $\Delta T = 1.35 \text{ fs}$, 2.53 fs , and 3.88 fs for parallel N_2 . We find that the values of the ΔT do not change as the CEP is varied. We summarize the values of ΔT for all samples in table 3.1. We find that molecular alignment does not affect the values of ΔT . The phases of the Fourier components ϕ_{Fourier} are plotted as a function of the CEP in figure 3.15. It is clear that the phases ϕ_{Fourier} of the first Fourier components are independent of the CEP, while the phase of 2nd and 3rd Fourier components, $\phi_{\text{Fourier}}^{2\text{nd}}$ and $\phi_{\text{Fourier}}^{3\text{rd}}$ linearly increase as the CEP is varied. Figure 3.15 shows that molecular alignment does not affect the phase ϕ_0 . These observations mean that in the observed spectra there

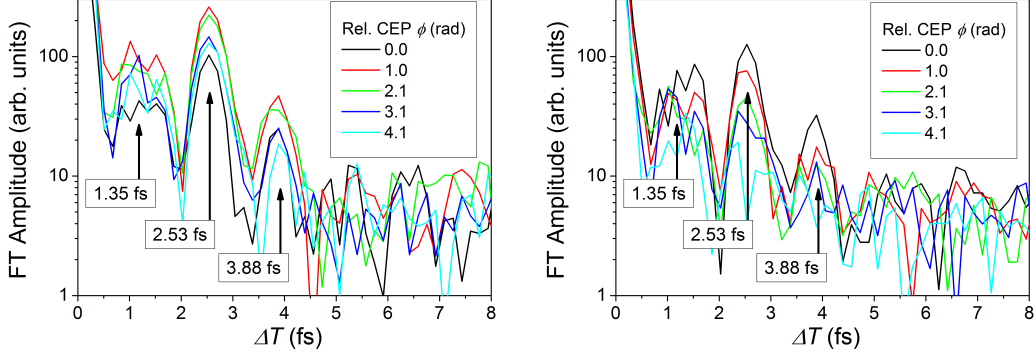


Figure 3.13: The absolute values of Fourier spectra for parallel N_2 (left) and for perpendicular N_2 (right) for different values of the relative CEP.

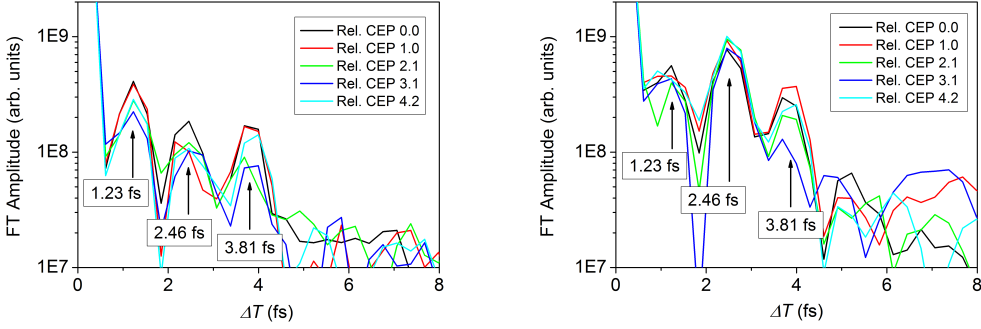


Figure 3.14: The absolute values of Fourier spectra for parallel CO_2 (left) and for random CO_2 (right) for different values of the relative CEP.

exist three sinusoidal curves given by

$$\cos(\omega\Delta T_i + 2\phi_{CEP} + \phi_0 + \phi(\omega)), \quad (3.22)$$

where $\phi(\omega)$ is a frequency dependent phase. By applying inverse Fourier transform to the Fourier spectrum [97] we obtain these sinusoidal curves. Figure 3.16 and figure 3.17 show alignment dependence of the harmonic spectra (a), the filtered spectra of 2nd Fourier peaks(b), and 3rd Fourier peaks(c) for N_2 and CO_2 , respectively. The filtered spectra (b) and (c) are shown for the relative CEPs 0, $\pi/3$, $2\pi/3$, and π from the bottom to the top. In figure 3.16 the solid black lines are for parallel N_2 , and the dashed red lines are for perpendicular N_2 . In figure 3.17 the solid black lines are for parallel CO_2 , and the dashed red lines are for random CO_2 . For CO_2 , in the suppressed region (42–54 eV) the phase of the 2nd and 3rd Fourier peaks, $\phi_{\text{Fourier}}^{2\text{nd}}$ and $\phi_{\text{Fourier}}^{3\text{rd}}$, are distorted, while outside the region these are relatively in phase.

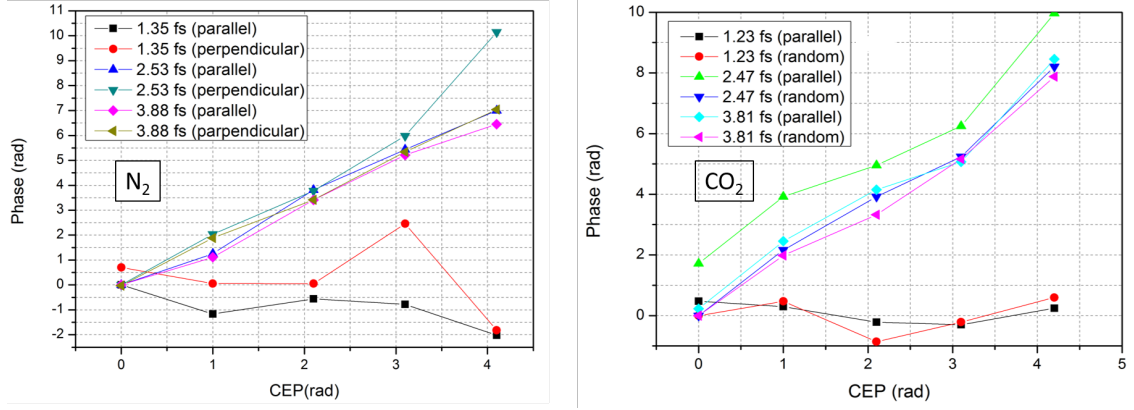


Figure 3.15: The phase of the Fourier peaks ϕ_{Fourier} for the parallel and the perpendicular N_2 (left) and for the parallel and the random CO_2 (right). The phase of the Fourier peaks ϕ_{Fourier} for parallel N_2 at the relative CEP value $\phi_{\text{CEP}} = 0$ is set as 0 rad for the left panel. The phase of the Fourier peaks ϕ_{Fourier} for random CO_2 at the relative CEP value $\phi_{\text{CEP}} = 0$ is set as 0 rad for the right panel.

Table 3.1: The potions of the Fourier peaks, ΔT , for four kinds of samples. In the middle row, the results for numerical simulations with Lewenstein model and the simple model are listed. By comparison, $T_{\text{las}}/2$, T_{las} , and $3T_{\text{las}}/2$ where T_{las} is an optical period at 800 nm are shown in the bottom line of the table.

sample	ΔT_1	ΔT_2	ΔT_3
parallel N_2	1.35 fs	2.53 fs	3.88 fs
perpendicular N_2	1.35 fs	2.53 fs	3.88 fs
parallel CO_2	1.23 fs	2.46 fs	3.81 fs
random CO_2	1.23 fs	2.46 fs	3.81 fs
Lewenstein model	1.15 fs	2.64 fs	3.96 fs
Simple model	1.31 fs	2.60 fs	3.91 fs
Optical period T_{las}	1.33 fs	2.67 fs	4.00 fs

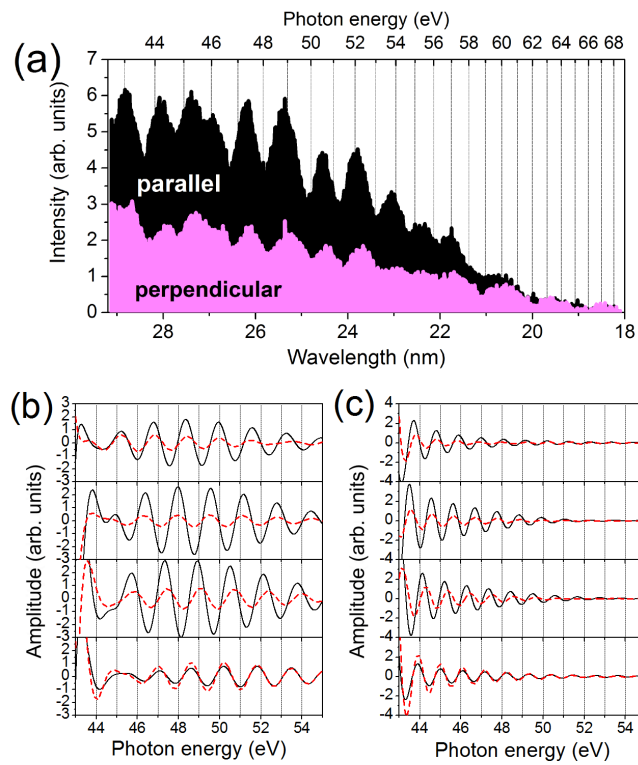


Figure 3.16: Harmonic spectra generated in parallel N₂ (black) and perpendicular N₂ (pink). (b) and (c) The harmonic spectral components from the second and the third Fourier component, respectively, obtained for different values of the CEP. The relative CEP are 0, $\pi/3$, $2\pi/3$, and π from the bottom to the top. The results obtained for parallel and random N₂ are shown by the black solid red dashed curves, respectively.

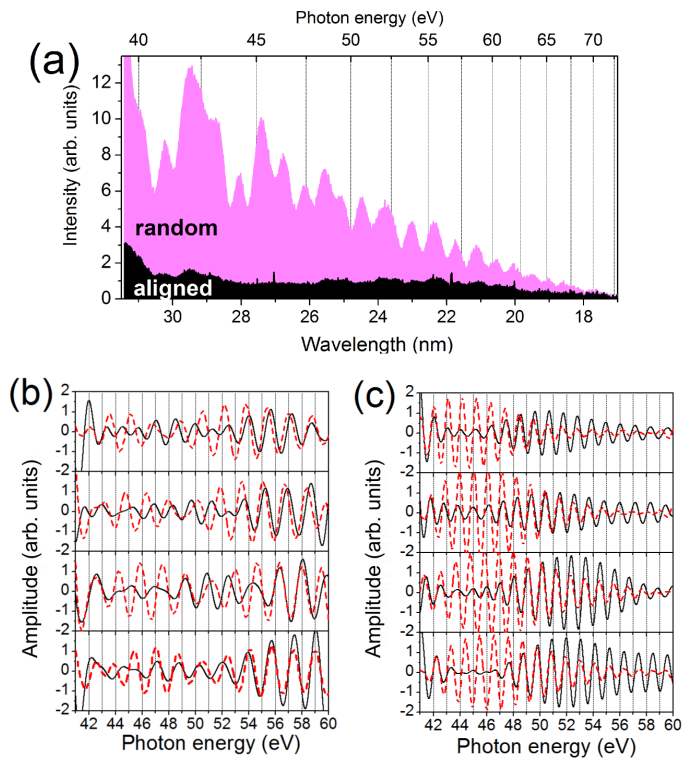


Figure 3.17: Harmonic spectra generated in parallel CO₂ (black) and random CO₂ (pink). (b) and (c) The harmonic spectral components from the second and the third Fourier component, respectively, obtained for different values of the CEP. The relative CEP are 0, $\pi/3$, $2\pi/3$, and π from the bottom to the top. The results obtained for parallel and random CO₂ are shown by the black solid red dashed curves, respectively.

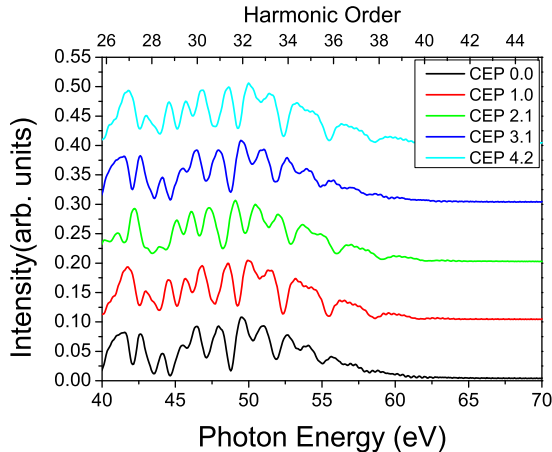


Figure 3.18: Calculated spectra by the Lewenstein model [65]. Intensity is 3×10^{14} W/cm²

3.2.4 Simulation with the Lewenstein model

We use a computational simulation to understand the underlying physics of the experimental results. We calculated the harmonics with a commonly used quantum mechanical model (the Lewenstein model) [65] using the parameters that match the experimental conditions. Figure 3.18 shows the calculated power spectra for five different values of the CEP. The peaks in the spectra show shifts that are similar to the experimental results. We analyzed the calculated spectra with the procedures used to analyze the experimental results and described in section 3.2.3. Figure 3.19 shows the absolute values of the Fourier spectra. We obtain Fourier components at $\Delta T = 1.15$ fs, 2.64 fs, and 3.96 fs. We find that the calculated Fourier spectra exhibit higher order components than the experimental results. It is likely that the limited detector resolution and low signal-to-noise ratio prevent these higher order Fourier components from being experimentally observed. The phases of the Fourier components ϕ_{Fourier} are shown on the right side of figure 3.19. The phase of the first Fourier $\phi_{\text{Fourier}}^{\text{1st}}$ component does not depend on the value of the CEP, whereas the phases of the higher components show a dependence on the CEP values, as seen in the experimental results.

3.3 Discussion

3.3.1 Simple model to describe origine of peaks in Fourier spectrum

The CEP-dependent changes of the spectral characteristics of the HHs were observed by Baltuška *et al.*[32]. Shortly afterwards, Nisoli *et al.* observed the CEP-dependent changes in the high-order harmonic spectra by exploiting one-shot measurements in which the value of the CEP and the high harmonic spectra are simultaneously measured [98].

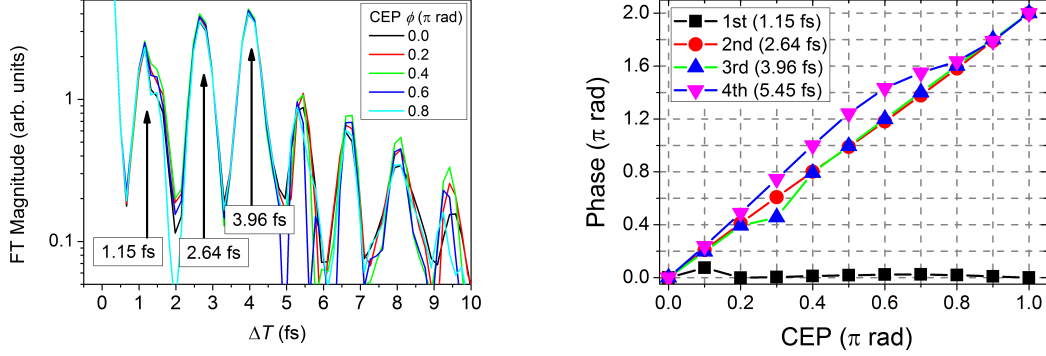


Figure 3.19: Absolute values of Fourier transform of power spectra shown in figure 3.18 (left). The phase of the Fourier peaks ϕ_{Fourier} .

Both groups explained the changes of the spectral characteristics by an interference of the attosecond pulses. When a few-cycle pulse is used, one or two attosecond pulses are generated depending on the value of the CEP. Setting the CEP such that a single attosecond pulse is generated, a structureless spectrum is observed in the cutoff region, while setting the CEP such that two or more attosecond pulses are generated, fringes are observed in the cutoff region. Recently, Mansten *et al.* showed that the interference can be interpreted in terms of the number of attosecond pulses in a specific frequency region by introducing a simple analytical model [99]. In this model, assuming that each pulse has the same temporal profile $a(t)$, the attosecond pulse train that contains N pulses and ($M = N$ or $N \pm 1$) pulses which have different parity is given by

$$S(t) = \sum_{j=1}^N a(t) \otimes \delta(t - jT) - \sum_{j=1}^M a(t) \otimes \delta(t - jT - T/2), \quad (3.23)$$

where T is an optical period of the femtosecond pulse. The Fourier transform of this is given by

$$S(\omega) = A(\omega) (\sum_{j=1}^N e^{ij\omega T} - \sum_{j=1}^M e^{ij\omega T + i\omega T/2}) \quad (3.24)$$

$$= A(\omega) \left(e^{i(N+1)\omega T/2} \frac{\sin N\omega T/2}{\sin \omega T/2} - e^{i(M+2)\omega T/2} \frac{\sin M\omega T/2}{\sin \omega T/2} \right). \quad (3.25)$$

When $N = M$,

$$S(\omega) = e^{i(N+1)\omega T/2} \frac{\sin N\omega T/2}{\sin \omega T/2} (1 - e^{i\omega T/2}), \quad \text{then} \quad (3.26)$$

$$|S(\omega)|^2 = |A(\omega)|^2 \left| \frac{\sin N\omega T/2}{\sin \omega T/2} \right|^2 |\sin \omega T/4|^2. \quad (3.27)$$

The second term on the right-hand side of the equation (3.27) can be interpreted as fringes seen in figure 3.11, while the third term can be interpreted as the odd harmonics. Note

that this equation is not able to explain why three peaks appear in the Fourier transforms of the spectra shown in figure 3.11. Therefore, they modified the spectral component $A(\omega)$ to include an amplitude and a phase which depends on the laser intensity I_j . They calculate the spectrum that include those effects as a function of the CEP value, and find the fringes varies periodically with the CEP ϕ_{CEP} .

3.3.2 Model simulation

Mansten *et al.* have succeeded in reproducing the periodic variation of the fringes by introducing a simple model; however, the characteristics of the Fourier peaks of the fringes (e.g. see figure 3.13) have not been studied. So then, we explain those experimental results by a simulation with the simple model introduced by Mansten *et al.* [99]. Harmonics are generally given in time domain by

$$S(t) = \sum_j (-1)^j S_j(t - jT/2 - \frac{\phi_{\text{CEP}}}{2\pi}T) + \text{c.c.}, \quad (3.28)$$

where S_j represents an attosecond pulse. Quantum calculations revealed that high-order harmonics have two kinds of chirps, known as “harmonic chirp” and “atto chirp”, these terminologies are following Ref. [100]. These chirps are approximately expressed by [101, 102, 103, 104]

$$\Delta\phi_i(t) = -\alpha_i I(t) \quad i: \text{harmonic order}. \quad (3.29)$$

The harmonic order dependence of the phase $\Delta\phi_i$ is atto-chirp, while the phase change owing to a temporal profile of the intensity $I(t)$ is harmonic chirp. Here, because the spectral range of interest is not so broad, we neglect the atto-chirp so that α_i is constant, namely, α . With an FWHM of the Gaussian temporal profile of the intensity, τ_{las} , we have a chirp of high-harmonics [105],

$$\Delta\phi(t) = -\alpha I_0 e^{-\frac{4t^2 \ln 2}{\tau_{\text{las}}^2}} \quad (3.30)$$

$$\approx bt^2, \quad b = \frac{4\alpha I_0 \ln 2}{\tau_{\text{las}}^2} \quad (3.31)$$

where I_0 is the maximum intensity of the laser pulse². As for FWHM of the attosecond train, we use the value, $\tau_{\text{train}} = 2$ fs, determined with the result of the quantum model calculation [65]. Then, we have

$$S(t) = e^{-\frac{2t \ln 2}{\tau_{\text{train}}}} e^{ibt^2} \sum_j (-1)^j A(t - jT/2 - \frac{\phi_{\text{CEP}}}{2\pi}T) + \text{c.c.}, \quad (3.32)$$

where $A(t - jT/2 - \frac{\phi_{\text{CEP}}}{2\pi}T)$ is the j th atto-pulse in the attosecond train given by

$$A(t) = e^{-\frac{2t^2 \ln 2}{\tau_{\text{atto}}^2}}, \quad (3.33)$$

²In deriving the equation (3.31) the constant phase $-\alpha I_0$ is omitted.

where the FWHM of the attosecond pulse is set 300 as, determined with the results of the quantum model calculation [65]. Figure 3.20 shows the electric fields given by equation (3.32) for three values of the CEP. The harmonic chirp e^{ibt^2} is represented by the dashed curve in the same figure. The power spectra of equation (3.32) is given by

$$|S(\omega)|^2 = |FT(S(t))|^2, \quad (3.34)$$

which corresponds to high-order harmonic spectra. Figure 3.21 shows the absolute value of the Fourier spectrum of the equation 3.34. Note that five distinctive peaks are found at $\Delta T = 1.31$ fs, 2.60 fs, 3.91 fs, 5.22 fs, and 6.53 fs, respectively, which are comparable with results for experimental ones and Lewenstein model simulations (see table 3.1).

Figure 3.22 shows how the change in the value of the chirp b affects the phase of the 2nd–5th Fourier components ϕ_{Fourier} in the simple model. The upper left in figure 3.22 shows the phase of the 2nd Fourier components $\phi_{\text{Fourier}}^{2\text{nd}}$ for different values of the harmonic chirp b . When the attosecond pulse train has no harmonic chirp ($b = 0$), the phase of any Fourier component, including the 2nd Fourier component $\phi_{\text{Fourier}}^{2\text{nd}}$ shown in figure 3.22, is independent of the value of the CEP. As the harmonic chirp coefficient b is increased, the phase of the Fourier components ϕ_{Fourier} begin to be CEP-dependent, which are observed for the all Fourier components ϕ_{Fourier} shown in figure 3.22. When the harmonic chirp coefficient b is larger than 0.6 fs^{-2} , the phase of the 2nd Fourier component varies linearly with the CEP value $\phi_{\text{Fourier}}^{2\text{nd}} = 2\phi_{\text{CEP}}$. On the other hand, when the harmonic chirp coefficient b is larger than 0.4 fs^{-2} , the 3rd components $\phi_{\text{Fourier}}^{2\text{nd}}$ and the 4th components vary linearly with the CEP value. When the harmonic chirp coefficient b is larger than 0.2 fs^{-2} , the 5th components $\phi_{\text{Fourier}}^{5\text{th}}$ varies linearly with the CEP value. Since in our experiment the phase of the 2nd and 3rd components, $\phi_{\text{Fourier}}^{2\text{nd}}$ and $\phi_{\text{Fourier}}^{3\text{rd}}$, vary linearly with the value of the CEP $\phi_{\text{Fourier}}^{2\text{nd}(3\text{rd})} = 2\phi_{\text{CEP}}$, the harmonic chirp coefficient b must be larger than 0.6 fs^{-2} observed in our experiment in this simple model.

We evaluate the magnitude of the chirp b by using equation (3.31) under our experimental condition. The coefficient α has been calculated by several groups. Varjú calculated the value of the coefficient α for Argon to be in the range of 10–15 ($10^{-14} \text{ cm}^2/\text{W}$) in the cutoff region at $1.5 \times 10^{14} \text{ W}/\text{cm}^2$ by using Lewenstein model [100]. Gaarde et al. integrated the time-dependent Schrödinger equation within the single active electron approximation, and found the value of the coefficient α to be in the range of 10–20 ($10^{-14} \text{ cm}^2/\text{W}$) in the cutoff region for the 27th harmonic in argon and for the 41st harmonic in neon [104]. We estimate the intensity of the driving pulse such that Lewenstein model gives the same cutoff energy of the high-order harmonics. However, it is known that the intensity estimation in this way is not reliable. For example, the well-know cutoff law [106, 107]:

$$n\hbar\omega = I_p + 3.17U_p, \quad (3.35)$$

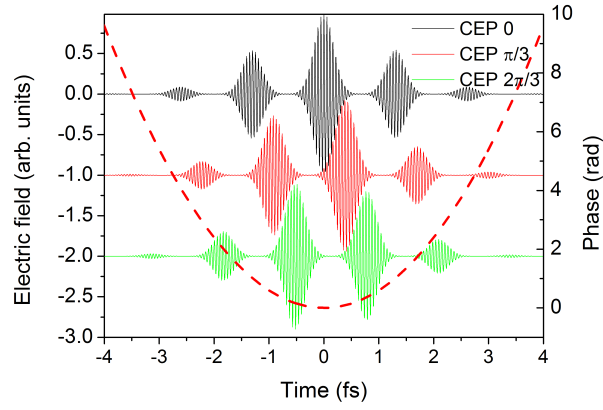


Figure 3.20: Solid lines: the temporal profiles of the high-harmonics in the simple model given by equation (3.32). The values of the CEP are 0, $\pi/3$, and $2\pi/3$ from the top to the bottom. Dashed line: the harmonic chirp defined in equation (3.31).

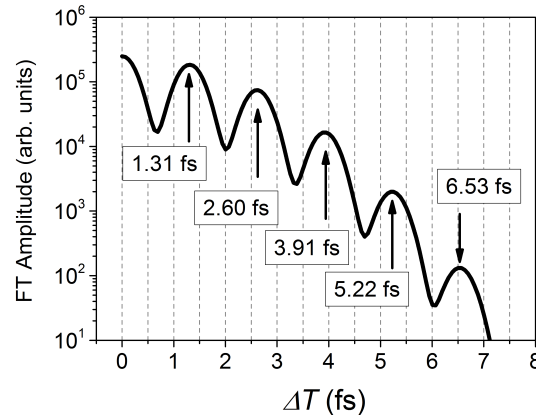


Figure 3.21: Absolute values of Fourier transform of the power spectrum calculated by equation (3.32) without introducing the chirp $b = 0$. In this figure five peaks are found at $\Delta T = 1.31$ fs, 2.60 fs, 3.91 fs, 5.22 fs, and 6.53 fs, respectively.

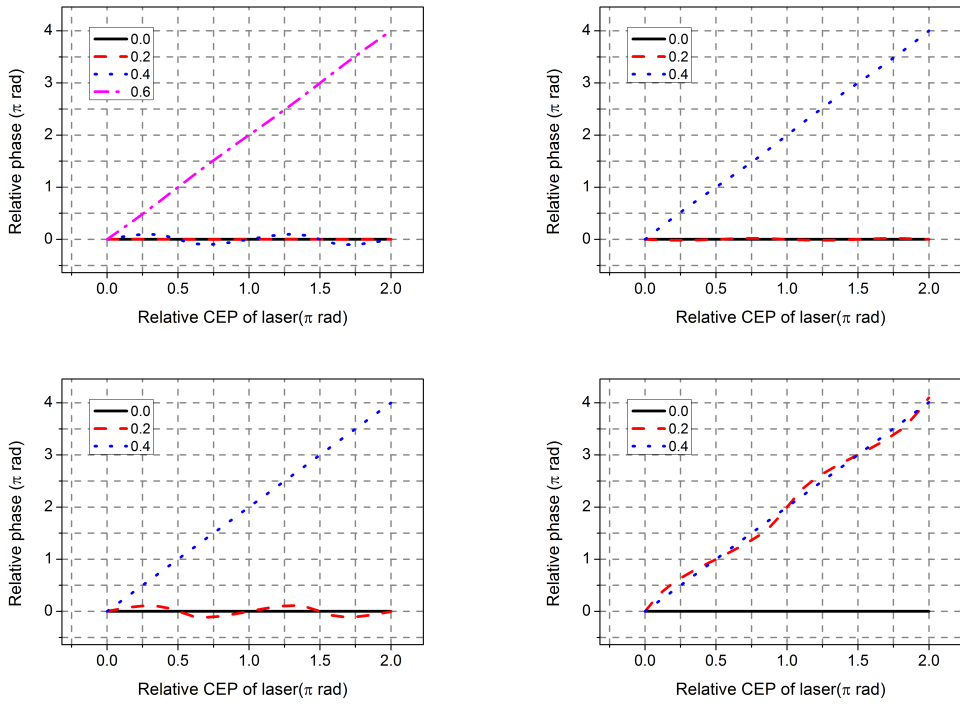


Figure 3.22: The phase of the Fourier components $\phi_{\text{Fourier}}^{2\text{nd}}$ (upper left), $\phi_{\text{Fourier}}^{3\text{rd}}$ (upper right), $\phi_{\text{Fourier}}^{4\text{th}}$ (lower left), and $\phi_{\text{Fourier}}^{5\text{th}}$ as a function of the CEP for different values of the harmonic chirp b , 0.0 fs^{-2} (solid lines), 0.2 fs^{-2} (dashed lines), 0.4 fs^{-2} (dotted lines), and 0.6 fs^{-2} (dash-dotted lines).

where U_p is the ponderomotive energy, gives the intensity of 2.5×10^{14} W/cm². Taking into account these uncertainties for parameters included in equation (3.31), we estimate the value of the chirp b to be $1.1(\pm 0.5)$ fs⁻². This value is in good agreement with the results $b > 0.6$ fs⁻² obtained by the simple model. This fact reinforces the interpretation of the observed fringes by the interference of attosecond pulses, and results in the possibility of observing the magnitude of harmonic chirp b without direct measurements of the high-order harmonic phase.

3.3.3 Effects of phase jump

Next we examine the possibility of observing the harmonic phase change in the harmonic spectra generated from aligned CO₂ and N₂ molecules. For aligned CO₂ and N₂ molecules, the harmonic phase depends both on the harmonic photon energy range and on the configurations of aligned molecules as discussed below. It should be noted that the harmonic phase is determined not only by the recombination phase but also by the continuum evolution phase, which is strongly influenced by the carrier laser field [58]. The continuum evolution phase can be significantly important in the present experiments with few-cycle pulses as the probe pulse because the intensity of the carrier wave changes rapidly within the pulse envelope. In addition, when an excited state such as HOMO-1 also contributes to the HHG process, other sources of the relative phase between the channels such as the phase associated with the evolution of the electronic states of the ion during the excursion of the electron wave packet and the ionization phase can also contribute to the harmonic phase [58]. Our Fourier analysis serves to examine in which Fourier component the harmonic phase change takes place.

In the case of N₂, it is reported that HOMO-1 in addition to HOMO contributes to the high-order harmonic spectra [59]. Since the symmetry of HOMO-1 is π_u , the contribution from HOMO-1 to the harmonic spectra should be more significant in the perpendicular configuration, where the probe pulse polarization is perpendicular to the molecular axis of aligned molecules, than in the parallel configuration, where the probe pulse polarization is parallel to the molecular axis of aligned molecules. The harmonic spectral components from the second and the third Fourier component are shown in figures 3.16 (b) and (c), respectively, which include the spectral regions in which the phase jump is observed with the RABITT technique [108]. First we note that the contribution from the third Fourier component is small in the harmonic photon energy range higher than ~ 52 eV. We also note apparent phase changes between the two configurations (parallel and perpendicular) or even the harmonic phase distortions at 43–46 eV in the harmonic spectral components from the second Fourier component. Although the observation of phase changes between the two configurations demonstrates the potential applicability of

the present self-referencing interferometry to probe harmonic phase changes in the HHG from aligned molecules, we find that high-order harmonic spectra with better statistics, with which the harmonic spectral component from each Fourier component is evaluated, are necessary to ensure the quantitative reproducibility of the phase change and to point out a conclusive indication of the phase change.

In the case of CO₂, destructive interference of electron de Broglie waves during the recombination process was first observed by our group and is successfully explained by the two-center interference picture [27]. The validity of the two-center interference picture has been further reinforced by our observation that suppression of harmonic intensity from aligned CO₂ molecules is observed for both 1300-nm and 800-nm pulses *over the same harmonic photon energy range* [29]. In fact, a π phase jump is observed in the harmonic photon energy range, where the harmonic intensity from aligned CO₂ molecules is suppressed, with various harmonic phase measurement techniques [109, 110, 111]. In figure 3.17 (b) one can see apparent phase changes or even anti-correlations in the harmonic phases between the two samples especially at 42–54 eV in the harmonic spectral component from the second Fourier component. However, since the intensities in the parallel configuration are very low, we find it rather difficult to provide a conclusive argument, and it should also be very difficult to apply the direct harmonic phase measurement techniques. We therefore emphasize that the strongly suppressed harmonic intensities in the parallel configuration should be further examined experimentally and theoretically as a new open question.

3.4 Summary

We observe clear interference fringes in the high-order harmonic spectra generated from aligned molecules with CEP-stabilized 10-fs pulses. A detailed Fourier analysis is applied to reveal that the CEP-dependent fringes are formed by the interference between attosecond pulses when the harmonic chirp is significantly large. We also examine the possibility of observing the harmonic phase change in the harmonic spectra generated from aligned CO₂ and N₂. In the course of the measurements, we find a remarkable characteristic that the harmonic intensities from aligned CO₂ molecules are more strongly suppressed than those observed with multi-cycle pulses. We also find that the contribution from the third Fourier component is small in the harmonic photon energy range higher than ~ 52 eV generated from aligned N₂ molecules.

Chapter 4

Coincidence study of tunnel ionization dynamics in OCS molecules

4.1 Experiment

We now describe the measurement system used in this experiment. A schematic diagram of the experimental setup is shown in figure 4.1. We use the same laser system as for the high-order harmonic generation experiment, but we do not use a hollow-core fiber, and the carrier-envelope phase is not stabilized. A laser pulse (FWHM ~ 25 fs, ~ 800 nm center wave-length) from the laser system passes through four optics and enters the spectrometer through a 2-mm-thick fused-silica window. The laser intensity is precisely controlled by the combination of a zero-order half-wave plate (Thorlabs) with a thin flat polarizer (65° incident, 25 mm diameter, LAYERTEC), and the intensity drift of the laser pulses is monitored during measurements (1 day – 7 days) by a photo diode. Another combination of a zero-order half wave plate and a zero-order quarter-wave plate allows us to control the ellipticity and the major axis of the laser pulse. In a coincidence velocity-map imaging spectrometer (CO-VIS) [112] unaligned molecular samples supplied in a super sonic molecular beam are ionized by focusing the laser pulse by a 100-mm-focal-length concave aluminum-coated mirror. The ionized samples and the produced electrons are detected by micro channel plates and HEXs in the spectrometer. The signals sent from detectors are processed by signal-processing electronics, and stored in a personal computer. In the following, each component shown in figure 4.1 is described in detail.

4.1.1 CO-VIS apparatus

In this section, we describe the coincidence measurement system, called coincidence velocity-map imaging spectrometer (CO-VIS) [112]. Figure 4.2 shows an overview of

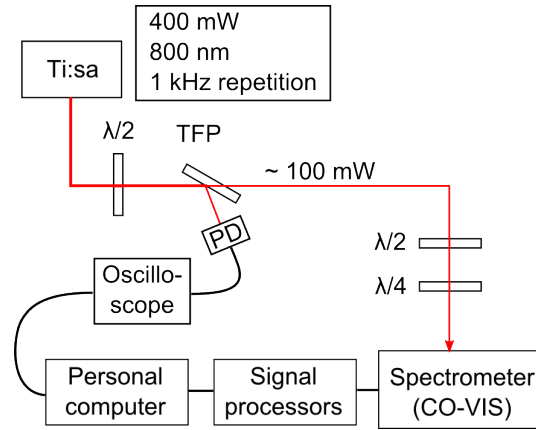


Figure 4.1: Schematic diagram of the experimental setup. See texts for details. $\lambda/2$: Half-wave plate. $\lambda/4$: Quarter-wave plate. TFP: Thin-film polarizer. PD: Photo diode.

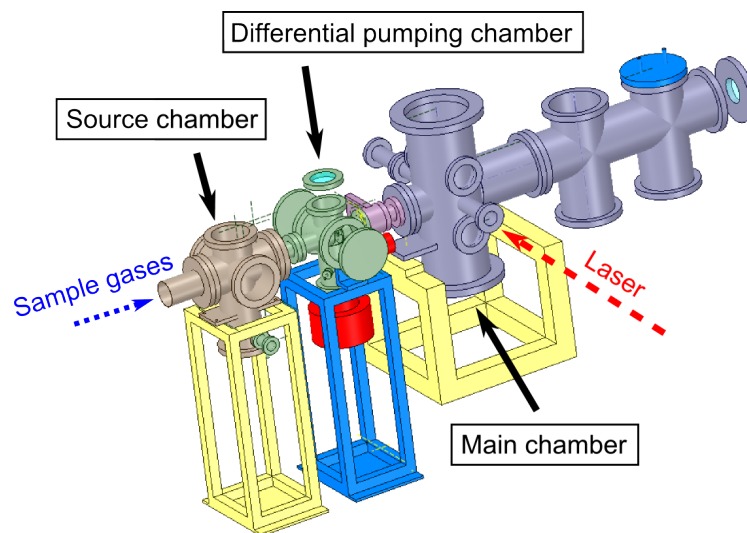


Figure 4.2: Overview of the CO-VIS system. From left to right: source chamber (orange), differential pumping chamber (green), gate valve (purple), and main chamber (blue). Sample gases are expanded into the source chamber (dotted line). The laser enters the main chamber through a fused silica window (dashed line).

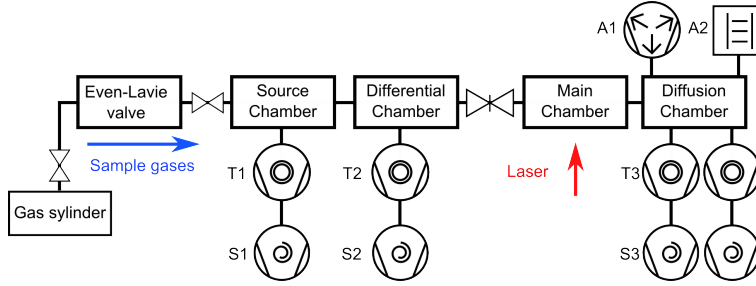


Figure 4.3: Pumping system of CO-VIS. T1: Edwards, STP-451; T2: Pfeiffer, HiPace300; T3: Edwards, STP-1603C; S1: ANEST IWATA, ISP-250C; S2: ; S3: ANEST IWATA, ISP-500C; A1: SAES Getters, CapaciTorr D-2000; A2: home-built liquid N₂ cold trap. Vacuum symbols are found in figure 1.

Table 4.1: Sustainable temperature for several components

item	sustainable temperature
skimmer	1000
MCP	480
HEX	150
O-ring	140
View port(SQ)	350

the apparatus. The CO-VIS consists of three vacuum chambers: a source chamber for loading sample gasses with an Even–Lavie valve, a differential pumping chamber for skimming the molecular beam, and a main chamber, where the laser pulse interacts with the molecular samples, for coincidence measurement of photo-ions and photo-electrons. In the following sections, we describe each component in detail.

Ultrahigh-vacuum chamber

A vacuum system is crucial for coincidence measurements because only a single target molecule should be ionized by a given laser pulse. For our experiments, we designed a vacuum chamber to obtain the vacuum of $\sim 1 \times 10^{-10}$ torr. Under this pressure, a typical background event is less than 0.1 per one laser shot. Figure 4.3 shows the pumping system. The vacuum is created by turbo-molecular pumps assisted by a getter pump and a liquid N₂ cold trap. Baking the chamber at high temperature ~ 100 °C is a common way to obtain an ultrahigh high vacuum. We used sheath heaters for each chamber and extra ribbon heaters for joints and other places. Several items were maintained at or below the temperatures given in table 4.1. With this setup, we obtained a vacuum of $\sim 1 \times 10^{-10}$ torr. Finally, we introduced a liquid N₂ cold trap system to evacuate, for example, remaining H₂O molecules, which are more likely to be ionized than OCS molecules, and pose major problems for our experiment.

Photoelectron and fragment ion spectrometer

Several techniques and apparatuses have been developed to obtain the MF-PADs that are usually smeared out by freely rotating molecules in the gas phase. The MF-PAD is the key to understanding the underlying physics of molecule–light interaction because, for one thing, photoelectrons carry information about the molecular orbitals [40]. Recently two different experimental techniques have been developed to obtain the MF-PAD of polar molecules in intense laser fields: the molecular alignment (orientation) technique [23] and the photoion–photoelectron coincidence technique [19]. As described in section 1.2.2, we do a photoion–photoelectron coincidence measurement to obtain the MF-PAD.

The velocity imaging method was first developed by Eppink and Parker [113], who used electrostatic lens to form an inhomogeneous electric field over the interaction region to render the velocity imaging initial-velocity independent. To simultaneously detect electrons and ions, Takahashi *et al.* placed a mesh in front of the ion-drift region to develop a new apparatus wherein electrons and ions with the same initial velocity arrive at the same position on the detector [114]. Later, Lebech *et al.* suggested a new apparatus wherein placing two meshes in front of the electron- and ion-drift regions causes the acceleration region to be formed by a homogeneous electric field [115]. To study the innershell photoionization dynamics of molecules, Hosaka *et al.* from the Yagishita group developed the CO-VIS for coincidence velocity mapping. The design is based on the velocity imaging method [112].

With the help of the Yagishita group, we have developed an home-built CO-VIS apparatus. Ions and electrons are produced at the intersection of a super-sonic molecular beam with a femtosecond laser pulse. Figure 4.4 shows the cross section of the spectrometer and the associate equipotential lines. The intersection region wherein electrons and ions are produced is located at the center of the cross section. The spectrometer is covered by a μ metal to avoid geomagnetic field invading into the spectrometer. The spectrometer has twelve lenses (L1–L12), two meshes (one at L3 and one at L8), two MCPs, and two delay-line anodes (DLAs). The lens sets (L1–L3 and L6–L8) form a homogeneous electric field in the acceleration region, which directs charged particles into the drift region. Two other lens sets (L4, L5, and 11 and L9, L10, and L12) form in-homogeneous electric fields in the drift region to direct charged particles to the same position on the surface of the MCP detectors, irrespective of their initial positions. The electric current of the arrived charged particles is amplified by the voltage-biased MCPs and detected by the delay-line anodes. The momenta of the charged particles can be calculated from these current signals, as explained in section 4.1.3.

We optimized the voltage of each lens such that electrons generated over a Rayleigh length ($z = -2$ mm to 2 mm) are focused to a 0.1-mm width on the surface of the MCP

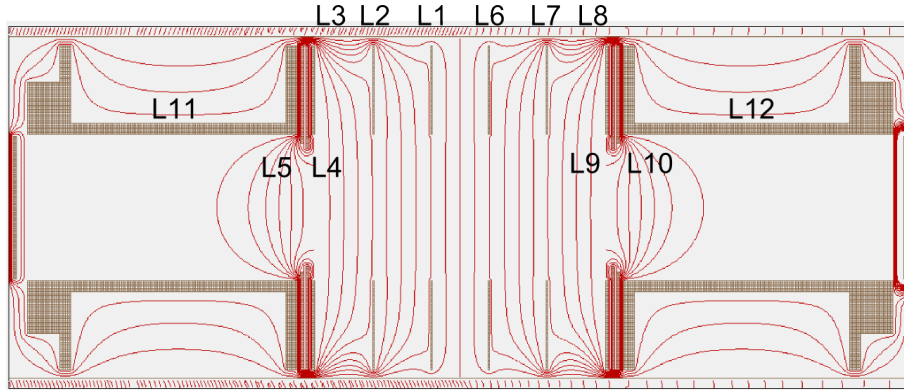


Figure 4.4: Equipotential lines formed by set of electrostatic lenses. Lenses L1–L3 and L6–L8 form an acceleration region where the charged particle is extracted into a drift region through a mesh located at L3 (or L8 for particles of opposite charge). The combination of L4 (L9), L5 (L10), and L11 (L12) forms a drift region where charged particles generated at different positions are focused on the surface of the MCP. The geometry file for the SIMION software is provided by the Yagishita group.

for electron moving along the x axis with the initial kinetic energies from 0 to 5 eV. Note that the trajectories depend only on the potential and the kinetic energy [116]. We obtain the following optimized voltage set: L3 (L8) = (–)500V, L4 (L9) = (–)712 V, L5 (L10) = (–)319 V, and L11 (L12) = (–)170 V.

Delay-line anode

When an electron shower created by the MCP arrives at a wire at position u , two voltage pulses propagate with a constant velocity v_u from the position u toward the two ends of the wire. Detecting the arrival times t_1 and t_2 of these pulses at the wire ends, the position where the charge arrived can be calculated in the delay line’s coordinate system as

$$u = f_v \cdot (t_1 - t_2), \quad (4.1)$$

where $f_v = v_u/2$. A delay line consists of a pair of wires (“signal” and “reference”) that are wound around a holder. These two wires form a Lecher line, which has a well-defined impedance. To gather almost all electrons, the signal wire is at a + 200 V potential with respect to its reference wire. Combined with a differential amplifier, this geometry significantly reduces noise [117].

Note that the signal referred to above does not propagate along the wire but perpendicular to the wire. This fact decreases the effective speed of the signal, which improves spatial resolution. In addition, an electron shower hits several positions of wires. Because the signal-processing electronics only deals with the “center of the mass” of the voltage pulse, the detector’s spatial resolution is better than the wire separation [117].

The HEX consists of three pairs of the delay-line anodes which are wound in different

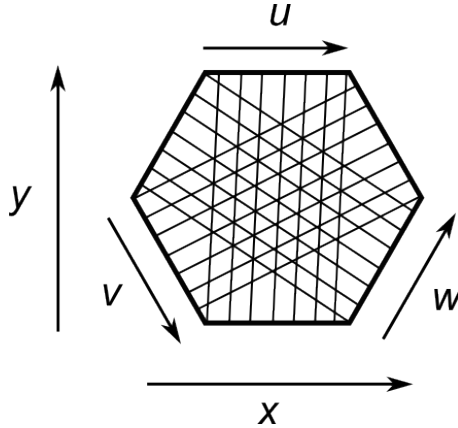


Figure 4.5: Coordinate system of HEX.

directions around a holder. They determine the positions u , v , w for each direction. Figure 4.5 shows the relation between the hexagonal frame and a Cartesian coordinate system. The hexagonal frame can be transformed into the Cartesian coordinate system by the following equations [117]:

$$x_{uv} = u, \quad y_{uv} = (u - 2v)/\sqrt{3} \quad (4.2)$$

$$x_{uw} = u, \quad y_{uw} = (2w - u)/\sqrt{3} \quad (4.3)$$

$$x_{vw} = v + w, \quad y_{vw} = (w - v)/\sqrt{3}. \quad (4.4)$$

These position data are used to calibrate the parameters f_u , f_v , f_w . For further details see manuals provided by RoentDek [117].

Gas jet

We use a supersonic molecular beam to supply samples into the spectrometer for two reasons: First, it decreases translational temperature, which improves the momentum resolution from $k_B T \sim 26$ meV at room temperature (300 K) to $k_B T \sim 1$ meV at 10 K. Second, a gas jet can insert a high density of samples into the spectrometer without excessively sacrificing the vacuum. In our experiment, we create a gas jet by using an Even–Lavie valve [118], which can potentially reduce the sample temperature to ~ 1 K. Below 10 K, the momentum resolution in our experiment is determined by the detector resolution.

Molecular samples are expanded in the source chamber through the Even–Lavie valve supplies. A molecular beam is extracted from the free molecular flow region by a 3-mm-diameter skimmer (Beam Dynamics, No. 50.8). A skimmer consists of a conical nozzle shaped to avoid any supersonic shock waves going back into the gas flow and increasing the translational temperature. The dimension of the extracted molecular beam is much larger

than the laser focus, which is $\sim 0.1 \times 1 \text{ mm}^2$, and thus it would unnecessarily degrade the vacuum of the spectrometer. Therefore, the molecular beam is further 0.5-diam skimmed by another skimmer (Beam Dynamics, Model 2, 0.50 mm diameter) located in the differential pumping chamber. As a result, we maintain the vacuum of $\sim 1 \times 10^{-10}$ torr in the spectrometer even when a molecular sample is introduced.

Coordinate system

Figure 4.6 defines the coordinate system in the spectrometer. The view from the polarization plane is shown in figure 4.6 (a), and the side view of (a) is shown in figure 4.6 (b). The molecular beam is injected along the negative y axis. Note that the x axis for the electron detector is reversed. The laser propagates along the x axis of the ion detector, and focused along the negative x axis of the ion detector by the concave mirror. The spectrometer from negative x axis, and back focused by a concave mirror. On the upper left side of the figure, the conditions of the polarization are described (CCW, CW). The major polarization axis is along the z axis. Note that the condition of the polarization does not change by the reflection on the concave mirror.

To confirm this coordinate system, we measured momentum distribution of OCS^+ with the electron detector by changing the polarity of the electrostatic lens and detectors. Figure 4.1.1 shows momentum distribution of OCS^+ detected with the ion detector (left) and the electron detector (right). Intense signals are found around $p_y \sim -15$ a.u. for both cases. As explained in section 4.2.2, the momenta correspond to the initial velocity of the molecular beam, and should be the same value for both cases in this coordinate system (see figure 4.6.) Note that the two momentum distributions are measured at different laser intensities, but this fact does not affect the above discussion.

4.1.2 Angular streaking and optical setup

When circularly polarized pulses or elliptically polarized pulses are used, ionized electrons never return to the vicinity of its parent ions; therefore, the propagation of the electron after ionization is simplified such that the electron is driven in the laser fields ignoring the Coulomb potential of the parent ion [107]. The equation of the motion of the electron after ionization is given by

$$\dot{\mathbf{p}}(t) = -\mathbf{F}(t), \quad (4.5)$$

where atomic units are used ($m_e = e = 1$, see appendix), \mathbf{p} is the momentum of the electron, and \mathbf{F} is the electric field. Integrating this equation we have

$$\mathbf{p}(\infty) = -\mathbf{A}(t_0), \quad (4.6)$$

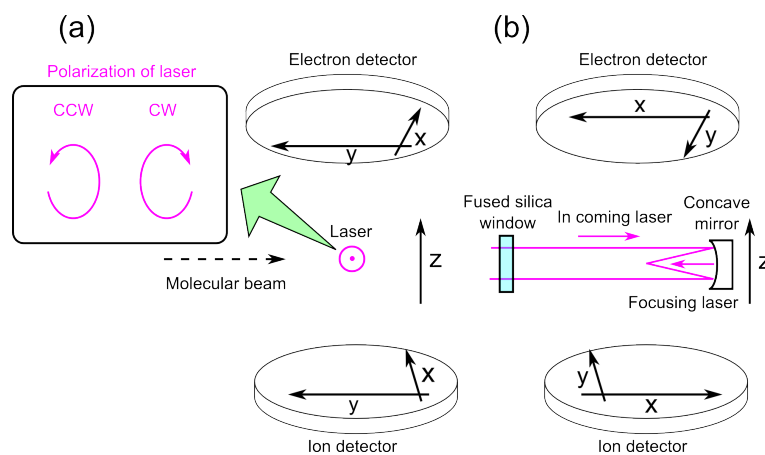


Figure 4.6: Coordinate system in the spectrometer viewed from the laser window (a), and viewed from the side of the laser window (b). The molecular beam is injected along the negative y axis. Note that the x axis for the electron detector is reversed. The laser propagates along the x axis of the ion detector, and focused along the negative x axis of the ion detector by the concave mirror. On the upper left side of the figure, the conditions of the polarization are described (CCW (LCP), CW (RCP)). CW: clockwise, CCW: counterclockwise, LCP: left-circularly polarized, RCP: right-circularly polarized.

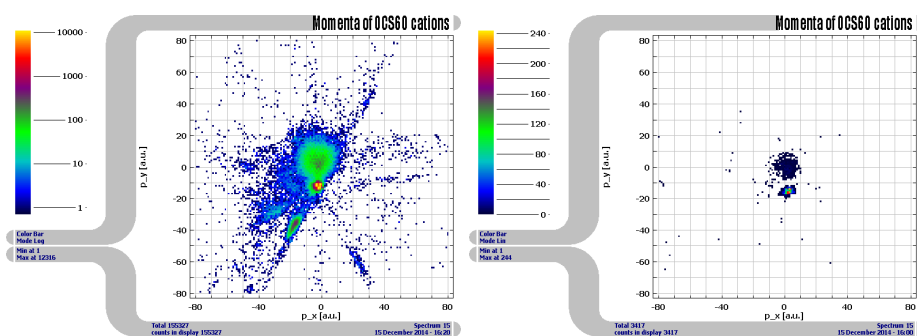


Figure 4.7: Momentum distributions of OCS^+ . Left: Momentum distribution in the normal setup. Right: Momentum distribution of OCS^+ detected with the electron detector by changing the polarity of electrostatic lens and detectors.

where t_0 is the instance of ionization and $\mathbf{A}(t)$ is the vector potential of the laser field, $\mathbf{A}(t) = -\int_{-\infty}^t F(t')dt'$. The vector potential precedes the electric field by a phase of $\pi/2$ or $-\pi/2$, which causes the asymmetry in head and tail ionization efficiency of molecules to be converted into the electron momentum asymmetry. Assuming the pulse duration is long enough to regard the pulse as a plane wave, the vector potential is given by

$$\frac{e}{\omega} \cos(\phi_0), \quad (4.7)$$

where ω the laser angular frequency, ϕ_0 is the phase of the laser pulse at the instance of ionization, $\phi_0 = \omega t_0$.

The angular streaking method is based on this classical picture. It originally proposed to map tunnel ionization time to angle of electron momentum by using a CEP-controlled near-circularly polarized few-cycle pulse [119]. This technique is known as ‘‘attosecond angular streaking’’ [119, 120, 121]. In our experiments, in multicycle regime, it maps the angle of electric field of elliptically polarized pulse at the instance of ionization to the angle of final momentum of the photoelectrons in the polarization plane. Figure 4.8 shows the schematic diagram of the angular streaking and relationship between ionization rate and momentum distribution of electrons. When right (left) circularly polarized pulses are used, the momentum distribution corresponds to the ionization rate, but rotated by $(-)\text{90}^\circ$. With this method, ionization rates of molecules can be measured as a function of angles between the electric field and the molecular axis [15, 23, 25].

Calibration of ellipticity

To experimentally determine the ellipticity and the angle of the major axis of the laser pulse a polarization beam splitter mounted on a rotational stage is placed after the quarter-wave plate, followed by a power meter. With the power meter, we measure the power of the transmitted laser pulse as a function of the angle of the polarized beam splitter. An elliptically polarized pulse is described as

$$\mathbf{F}(t) = F(t)(\cos \omega t, \epsilon \sin \omega t), \quad (4.8)$$

where $F(t)$ represents the pulse envelope, ω is the angular frequency, and ϵ is the ellipticity of the pulse. A polarization beam splitter transmits p -polarized pulses and reflects s -polarized pulses. When rotating the splitter by θ the p -polarized vector can be obtained by multiplying Eq. (4.8) by the rotation matrix:

$$\begin{pmatrix} \cos \theta & -\sin \theta \\ \sin \theta & \cos \theta \end{pmatrix}, \quad (4.9)$$

which gives the following p -polarized pulse:

$$\mathbf{F}(t, \theta)_p^2 = F(t)^2(\cos^2 \theta \cos \omega t + \epsilon^2 \sin^2 \theta \sin^2 \omega t - 2\epsilon \cos \theta \sin \theta \cos \omega t \sin \omega t). \quad (4.10)$$

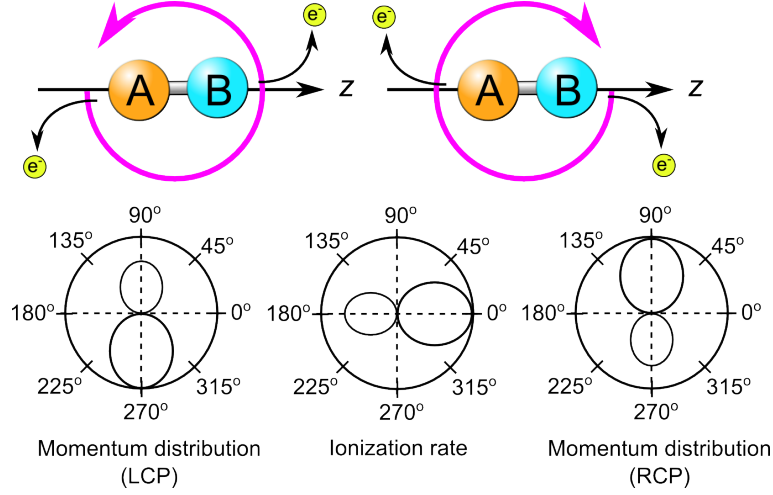


Figure 4.8: Schematic diagram of the angular streaking. The upper part shows the schematic diagram of the angular streaking for left circularly polarized pulses (left) and right circularly polarized pulses (right). Two electrons gain momenta depending on the timing of ionization in a circularly polarized field (rotating pink arrow). The lower part shows the ionization rate of the A–B molecule and the momentum distribution of ionized electrons as a function of angle. The angle is between z axis and the electric field for the ionization rate, and between z axis and the electron momentum for the momentum distribution. LCP: left-circularly polarized. RCP: right-circularly polarized.

Averaging this over the phase ωt and integrating over t , we obtain the power as a function of the rotation angle θ for a p -polarized pulse:

$$F_p(\theta)^2 \propto 1 - (1 - \epsilon^2) \sin^2 \theta. \quad (4.11)$$

Fitting the experimentally observed power with Eq.(4.11) as a function of the angle θ of the beam splitter gives the ellipticity ϵ and the angle ϕ of the major axis¹.

Figure 4.9 shows the experimentally observed ellipticity ϵ and the major axis of polarization ϕ as a function of the angle of the half-wave plate. Because the laser pulse has a broad spectrum, the angle of the major axis starts to deviate from zero as the ellipticity nears unity. The wave plates ideally works only at wavelength of 800 nm. In order to compensate for the change in the angle ϕ of the major axis, we optimize the angle of both the half-wave plate and the quarter-wave plate. As a result, we obtain a right-circularly-polarized pulse (RCP) with ellipticity of 0.85 and a major axis angle of -1.6° from the z axis and a left-circularly-polarized pulse (LCP) with ellipticity of 0.84 and a major axis angle of 2.7° from the z axis.

¹Explicitly, the angle θ in equation 4.11 should be replaced by $\theta' = \theta + \phi$, where θ is the angle of the beam splitter, ϕ is the angle of the major axis of the polarization.

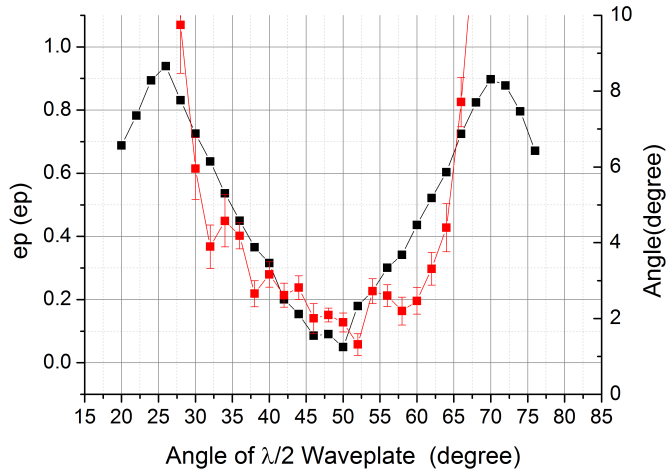


Figure 4.9: Measured ellipticity as a function of angle of the $\lambda/2$ wave plate.

Intensity calibration

Laser intensity is one of the most important parameters in this experiment because it changes the Keldysh parameter, and can change the ionization process accordingly. We calibrated the intensity as described below. None of these values is reportedly more reliable than within $\pm 0.5 \times 10^{14}$ W/cm² [122, 123].

The dissociation process for H₂ molecules is strongly affected by changing the laser intensity. In 1990, Bucksbaum *et al.* found that the kinetic energy released by the dissociation of H₂ has discrete momentum peaks separated by the energy of a single photon [125]. They explained this phenomenon by introducing a field-dressed bonding state and invoking transitions between these states to explain the discrete momentum. This phenomenon was named “bond softening”. Later, Alnaser *et al.* suggested that the momentum peak ratio can be used to calibrate the intensity of the laser pulse [124]. Figure 4.10 shows the reference TOF spectra of protons [126] and observed TOF spectra of protons from background H₂ at various laser powers measured by a power meter. By comparing patterns of the TOF spectra to tabulated spectra from Ref. [126], we obtain a rule: the intensity is roughly $(1 \pm 0.5) \times 10^{14}$ W/cm² for 100-mW pulses.

4.1.3 Reconstruction of momenta of ion and electrons

With the CO-VIS apparatus, an ion or an electron with a specific initial momentum hits the MCP at the corresponding time and position. In order to reconstruct the initial momentum, we should know the arrival time of one MCP signal and six DLA signals for the ion and six DLA signals for the electron. To accurately record the arrival times, the

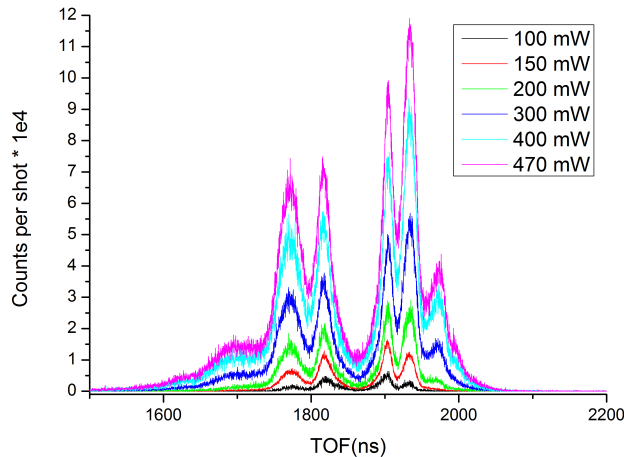


Figure 4.10: Time of flight for protons with linearly polarized pulses for various pulse intensities. Comparison of the results with the reference spectra from Ref. [124] gives laser intensity estimation.

MCP and DLA signal are amplified by an amplifier (FAMP8, Roentdek) followed by a constant fraction discriminator (CFD) (CFD7x, Roentdek). The CFD reduces the timing jitters caused by the fluctuation in signal magnitude. The processed signals are digitized by a TDC card (HPTDC8, RoentDek) in a personal computer and stored as a list-mode file (LMF). LMFs are analyzed by a software (COBOLD2010, Roentdek). The program reconstructs the TOF and the position of detected particles.

4.1.4 Momentum calibration

Ion

The flight time of ions t_{TOF} can be described by the arrival time of the MCP signals t_{MCP} and the irradiation time of the laser pulse t_{laser} as

$$t_{\text{TOF}} = t_{\text{MCP}} - t_{\text{Laser}} - t_{\text{offset}}. \quad (4.12)$$

Here, the residual time t_{offset} includes the signal propagation in cables, detector processing time in the electronics, etc. Calibration of the offset t_{offset} can be done with the experimental data as following.

Starting from the law of conservation of energy (the first integral of the equation of the motion), we obtain the time of flight [116]:

$$t_{\text{TOF}} = \sqrt{\frac{m}{2}} \int \frac{dz}{E - U(z)}, \quad (4.13)$$

where E the initial kinetic energy of ions, m the mass, and $U(z)$ the electric potential. This equation tells that the time of flight t_{TOF}^m of a particle with zero-kinetic energy is

determined only by the mass of the particle m :

$$t_{\text{TOF}}^m = A_{\text{mass}} \cdot \sqrt{m}, \quad (4.14)$$

$$t_{\text{MCP}}^m - t_{\text{Laser}}^m - t_{\text{offset}} = A_{\text{mass}} \cdot \sqrt{m} \quad (4.15)$$

which gives a mass spectrum. The offset time t_{offset} and the coefficient A_{mass} can be obtained by solving the equation 4.15 with at least two times $t_{\text{MCP}}^m - t_{\text{Laser}}^m$ for different masses.

We now find the relation between the energy E and the time of flight t_{TOF} . However, equation (4.13) is not solved analytically because the potential in the drift region is inhomogeneous. Therefore, the momentum is calculated using approximations. We approximate the momenta p_x and p_y :

$$p_x = \frac{mx}{t_{\text{TOF}}} \quad (4.16)$$

$$p_y = \frac{my}{t_{\text{TOF}}}. \quad (4.17)$$

Note that the t_{TOF} , x , and y are measurable. Because of the focusing lens in the drift region, the calculated momentum is different from the real one. This effect is compensated afterwards. The reconstruction of the kinetic energy E_{kin} along the z axis by the time of flight t_{TOF} is done approximately as

$$E_{\text{kin}} = A^+ \cdot (t_{\text{TOF}} - t_{\text{TOF}}^m)^2 \quad \text{when } t_{\text{TOF}} - t_{\text{TOF}}^m > 0, \quad (4.18)$$

$$= A^- \cdot (t_{\text{TOF}} - t_{\text{TOF}}^m)^2 \quad \text{when } t_{\text{TOF}} - t_{\text{TOF}}^m < 0, \quad (4.19)$$

where t_{TOF}^m is the time of flight with zero-kinetic energy given by eq (4.15). We obtain the coefficients A^+ and A^- by the following two steps: First, figure 4.13 shows the kinetic energy vs TOF for two target molecules with masses of 28 and 32 amu (a CO molecule and an S atom, respectively) obtained by simulating the trajectory with the SIMION software. By fitting these plots with the equation (4.19), we obtain the ratios A^-/A^+ , which are almost the same for the two fragments ($A^-/A^+ = 0.78365$ for CO and $A^-/A^+ = 0.78364$ for S). Second, the value of the coefficient A^+ is obtained by exploiting the symmetry between p_x and p_z or between p_y and p_z under an experimental condition. Figure 4.11 shows momentum distributions by changing the direction of polarization of the linearly polarized pulse with the same laser intensity. We change the value of the coefficient A^+ such that the symmetric momentum pair p_y and p_z appears in the same way upon changing the direction of polarization.

At this stage, the ratios among the momenta p_x , p_y , and p_z have been calibrated. However, they have an ambiguity in the magnitude because of the focusing lens in the drift region. The focusing lens shrinks the momentum distribution on the xy plane to

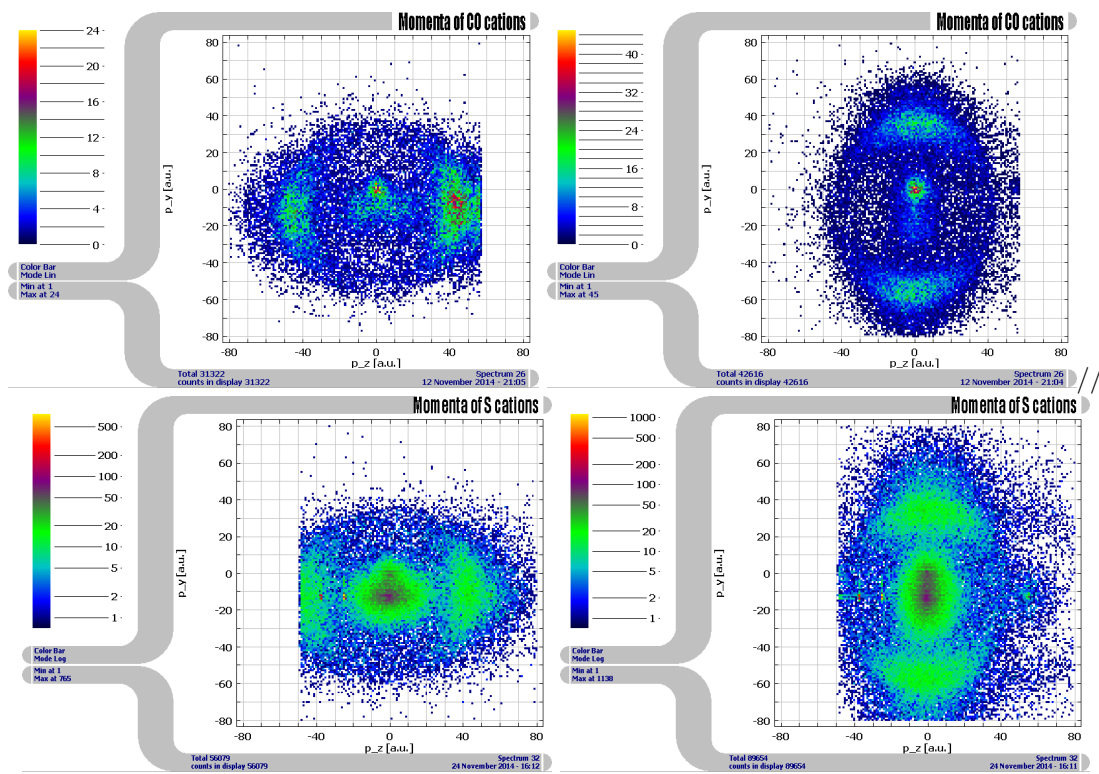


Figure 4.11: Top: Momentum images of CO⁺ in yz plane with linearly polarized pulses. The polarization are along y-axis (left) and z-axis (right) with the same intensity at $\sim 1 \times 10^{14}$ W/cm². The momentum p_z is calibrated by comparing these data. Bottom: Same but for S⁺. See texts for details.

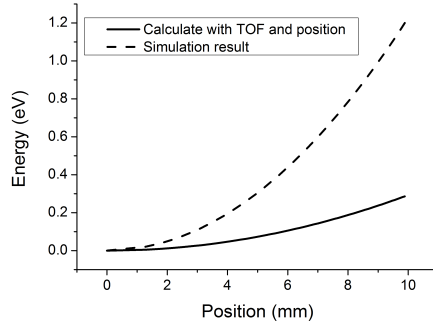


Figure 4.12: The kinetic energy as a function of position on the detector. The solid line shows the kinetic energy calculated with TOF and position data. The dashed line shows the result of the SIMION simulation.

some extent. Therefore, we compare the results of the trajectory simulations with and without the focusing lens effect, and magnify the momenta so that the momenta as a function of the position become the same as simulated ones. Figure 4.12 shows the kinetic energy as a function of position on the detector. The solid line shows the kinetic energy calculated with TOF and position data. The dashed line shows the result of the SIMION simulation. These plots are well fitted with parabolic functions, $E_{\text{kin}} = ax^2$. The coefficients a are 0.01225 for the dashed line and 0.00293 for solid line. Therefore, we obtain real kinetic energy by multiplying the calculated kinetic energy by ~ 4.2 .

This calibration method may be improved by using experimental data which have discrete peaks separated by a specific energy such as the above-threshold ionization or the photoelectron distribution by synchrotron radiation.

Electron

In the spectrometer electrons travel about two order of magnitude faster than ions. Therefore, the measurements of time of flights of electrons are not accurate enough to obtain the momenta of electrons along the z axis. Under an experimental condition where the polarization is linear along the y axis, i.e., the cylindrical symmetry is retained, the momentum p_z can be reconstructed by the Abel inversion method [127]. However, in our experimental condition, the cylindrical symmetry is not strictly perfect. Nevertheless, the two dimensional electron distributions have enough information to make conclusions. We calculate the momentum in the xy plane in the same way as done for ions. Note that, according to Maupertuis' principle [116], the trajectories of particles are determined by the potential and the energy. In other words, an ion and an electron with the same kinetic energy travels perfectly the same trajectory but the direction is inverse due to

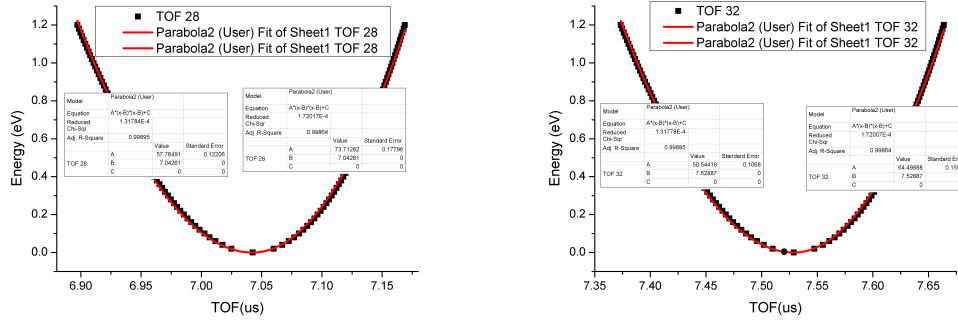


Figure 4.13: Kinetic energy as a function of time of flight of cations with masses of 28 amu and 32 amu for the left and right panels, respectively.

their opposite charges².

4.2 Results

4.2.1 Mass spectrum

Figure 4.14 shows the mass spectrum obtained when OCS molecules are introduced into the spectrometer. The laser intensity is 1×10^{14} W/cm², and the ellipticity is $\epsilon \sim 0.84$. We observed many ions which originate from OCS and other background gasses (H₂, H₂O, N₂, O₂, etc.). Intense and narrow signals of OCS⁺ isotopes appear at 60 amu to 64 amu. OCS²⁺ are found at 30 amu to 32 amu. The most intense signals at 60 amu and 30 amu are ⁶⁰OCS⁺ and ⁶⁰OCS²⁺, respectively. CO⁺ and S⁺ appear with broad spectra at 28 amu and 32 amu, respectively, presenting finite initial momenta. C⁺, O⁺, and CS⁺ appear at 12 amu and 16 amu, and 44 amu, respectively. The most intense background signal is H₂O at 18 amu. N₂⁺ and O₂⁺ are found at 28 amu and 32 amu, respectively, which overlap with CO⁺ and S⁺, respectively. H⁺, H₂⁺, and C²⁺ are found at 1 amu, 2 amu, and 6 amu, respectively. We have not observed SO⁺ at all, which is consistent with the result where OCS is ionized by a wavelength-selected light beam from an atomic discharge lamp with photon energies at 21.21 eV and 40.8 eV [128]. The observed ions are tabulated in table 4.2.1.

²The differential equation of the path can be derived by Maupertuis's principle as $2\sqrt{E-U} \frac{d}{dt} \left[\sqrt{E-U} \frac{dr}{dt} \right] = -\frac{\partial U}{\partial r}$ [116].

Table 4.2: Mass of some ions observed in the mass spectrum (figure 4.14. The atomic mass unit (amu) is used.

	H ⁺	H ₂ ⁺	C ⁺	O ⁺	H ₂ O	CO ⁺	N ₂ ⁺
Mass	1	2	12	16	18	28	28
	OCS ²⁺	S ⁺	O ₂ ⁺	CS ⁺	OCS ⁺		
Mass	30	32	32	44	60		

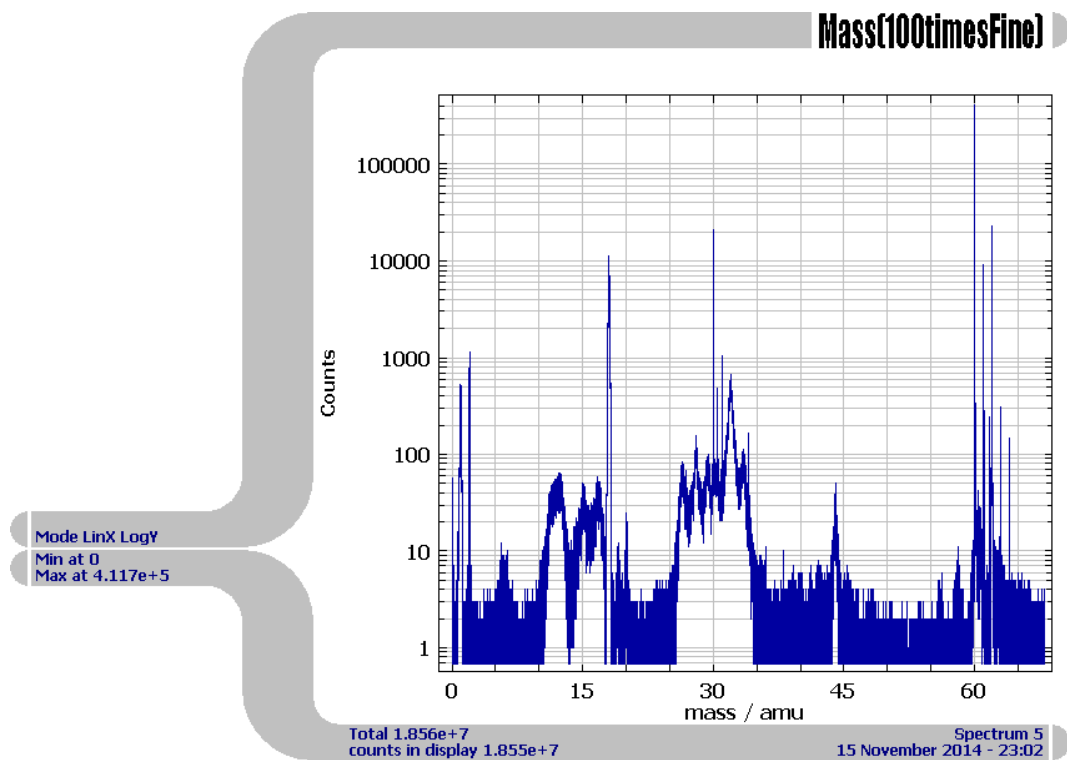


Figure 4.14: A mass spectrum at the laser intensity of 1×10^{14} W/cm². The ellipticity of the pulse is ~ 0.84 . The major polarization axis is along the y-axis.

4.2.2 Momentum distribution

Ion

Figure 4.15 shows momentum distribution of OCS^+ (left) and OCS^{2+} in the xy plane at laser intensities of $1 \times 10^{14} \text{ W/cm}^2$. The ellipticity of the pulse is $\epsilon \sim 0.84$. The major polarization axis is along the z axis. These distributions have maxima at $p_y^{\text{OCS}^+} \sim -50$ a.u. and $p_y^{\text{OCS}^{2+}} \sim -25$ a.u. for OCS^+ and OCS^{2+} , respectively, which can be explained by initial velocity of molecular samples. Since we use a gas jet to introduce OCS samples, the OCS samples have a specific translational velocity. Therefore, other fragments of OCS have the same initial velocity. We calculate the initial momentum p_y^{initial} of fragmented cations as

$$p_y^{\text{initial}} = m \cdot \frac{\left(p_y^{\text{OCS}^+} / 60 + p_y^{\text{OCS}^{2+}} / 30 \right)}{2}, \quad (4.20)$$

where m is the mass of the fragment ion in atomic mass unit.

Figure 4.16 shows the momentum distribution of CO^+ fragments in the xy plane at the laser intensity of $1 \times 10^{14} \text{ W/cm}^2$. The ellipticity of the pulse is $\epsilon \sim 0.84$. The major polarization axis is along the z axis. We explain how to interpret the momentum distribution with this data. After the explanation, we will show other momentum distributions at different laser intensities, or of other fragment ions. The interpretation we provide can be applied to those other momentum distributions. As indicated by a red arrow in figure 4.16, the isotropic distribution around the center $p_x \approx p_y \approx 0$ is attributed to N_2^+ molecules, which has the same atomic mass as CO_2 . The region indicated by a yellow arrow is produced by CO^+ molecules which are dissociated from OCS^+ molecules. The region indicated by a brown arrow is produced by CO^+ molecules which are produced by Coulomb explosion of OCS^{2+} molecules. The two regions which stem from OCS molecules (yellow and brown regions) shifts in momentum along the p_y axis by ~ 20 a.u., which can be explained by taking into account the initial velocity of the molecular beam. The velocity of the molecular beam is estimated to be $\sim 400 \text{ m/s}$.

Figure 4.17 shows momentum distribution of S^+ at laser intensities $5 \times 10^{13} \text{ W/cm}^2$ (upper left), $1 \times 10^{14} \text{ W/cm}^2$ (upper right), $1.5 \times 10^{14} \text{ W/cm}^2$ (lower left), and $2.2 \times 10^{14} \text{ W/cm}^2$ (lower right). The ellipticity of the pulse is $\epsilon \sim 0.84$ and its major axis is along the z axis and its minor axis is along the y axis. The momentum distributions consist of three regions: (i) background molecular ions (O_2), which has the same atomic mass as S and are observed near the center ($p_x \approx p_y \approx 0$) and isotropic. (ii) dissociated S^+ cations produced from singly charged OCS molecules (OCS^+), which are observed as a disc with a small momentum, and are slightly anisotropic. (iii) Coulomb exploded cations produced from highly charged OCS molecules (OCS^{2+} , OCS^{3+} , etc.), which are observed as an anisotropic ring with a large momentum. The regions (ii) and (iii) are slightly shifted

towards negative p_y , which can be explained by initial velocity of molecular samples. Since we use a gas jet to introduce OCS samples, the OCS samples have a distinctive translational velocity.

The background component without introducing OCS samples observed in the TOF regions of S^+ at the laser intensity of 1.5×10^{14} W/cm² is shown in the upper right panel of figure 4.21. The ellipticity of the pulse is $\epsilon \sim 0.84$. The main background ion near the center is expected to be the molecular ion O_2^+ , which has the same atomic mass as S^+ , and small signals of $^{18}O^{16}O$ is observed. These momentum distributions are all small and isotropic. Therefore, anisotropic distributions observed in figures 4.17–4.20 are confirmed to be from OCS samples.

The channel (ii) of the dissociated ions have small kinetic energy and show as light anisotropy. As discussed in section 4.3.2, the slight anisotropy indicates a rather long lifetime of the excited states which correlate to the $S^+ + CO$ channel. At the laser intensity 5×10^{13} W/cm² (upper left in figure 4.17), the dissociated ion channel dominates the momentum distribution, and is decreased as the intensity increases. On the other hand, the Coulomb explosion channel (iii) is a minor one at the intensity of 5×10^{13} W/cm² and is increased as the intensity increases. At the laser intensity higher than 1.5×10^{14} W/cm², the channel (iii) is the dominant channel in the momentum distribution. This fact shows that the production efficiency of highly charged ions OCS^{2+} , OCS^{3+} , etc. becomes much higher at these laser intensities.

Figure 4.18 shows momentum distributions of CO^+ obtained at laser intensities 5×10^{13} W/cm² (upper left), 1×10^{14} W/cm² (upper right), 1.5×10^{14} W/cm² (lower left), and 2.2×10^{14} W/cm² (lower right). The ellipticity of the pulse is $\epsilon \sim 0.84$ and its major axis is along the z axis and its minor axis is along the y axis. As observed in the momentum distributions of S^+ , there are three regions (i), (ii), and (iii) in the momentum distributions of CO^+ . The region (ii) for CO^+ is more anisotropic than that for S^+ , extending along the major polarization axis (z axis). The background molecular ions are expected to be N_2^+ ions for CO^+ .

At the intensity $\sim 5 \times 10^{13}$ W/cm² (upper left), the dissociated ion channel (ii) dominates the momentum distribution, and is decreased as the intensity decreases. On the other hand, the Coulomb explosion channel (iii) is the dominant channel in the momentum distribution. This is the same situation as S^+ momentum distributions. OCS^+ into CO^+ and S^+ .

Figure 4.19 shows momentum distributions of CS^+ at laser intensities 5×10^{13} W/cm² (upper left), 1×10^{14} W/cm² (upper right), 1.5×10^{14} W/cm² (lower left), and 2.2×10^{14} W/cm² (lower right). The ellipticity of the pulse is $\epsilon \sim 0.84$ and its major axis is along the z axis and its minor axis is along the y axis. The three regions (i), (ii), and (iii) can

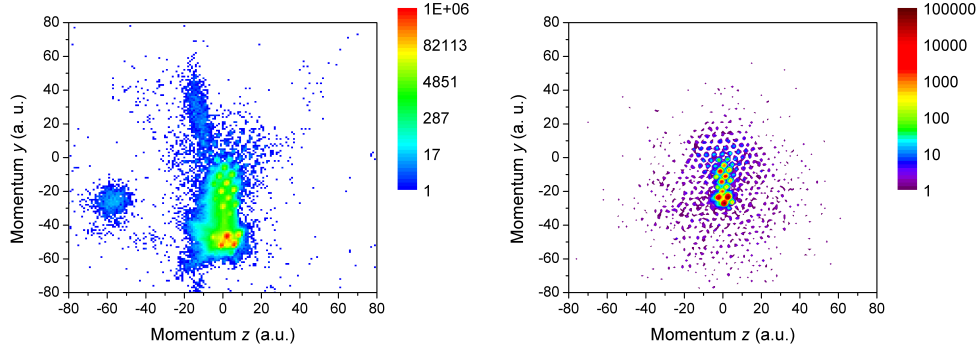


Figure 4.15: Momentum distributions of OCS^+ (left) and OCS^{2+} in the xy plane at laser intensities of 1×10^{14} W/cm². The ellipticity of the pulse is $\epsilon \sim 0.84$. The major polarization axis is along the z axis.

be observed as other fragments. At all laser intensities, the dominant contribution is the background molecular ions (i) which are expected to be CO_2^+ . In the dissociation channel (ii) there is an intense narrow peak at the center of the region. We expect these are CO_2^+ contained in OCS samples. It is known that the sample of OCS are contaminated with a small amounts of CO_2 impurity, which may produces spurious CO^+ signals. However, the observed amounts of CO_2^+ is smaller than the amounts of CO^+ . In addition, we confirm that CO_2 samples do not affect our experimental results, described in section 4.2.5.

Figure 4.20 shows momentum distributions of O^+ at laser intensities 5×10^{13} W/cm² (upper left), 1×10^{14} W/cm² (upper right), 1.5×10^{14} W/cm² (lower left), and 2.2×10^{14} W/cm² (lower right). The ellipticity of the pulse is $\epsilon \sim 0.84$ and its major axis is along the z axis and its minor axis is along the y axis. It can be seen the three regions (i), (ii), and (iii) as other fragments. The lower right panel in figure 4.21 shows background component without introducing OCS samples observed in the TOF region of O^+ at the laser intensity of 1.5×10^{14} W/cm². The ellipticity of the pulse is $\epsilon \sim 0.84$. The background ions are expected to be O^+ produced from H_2O or O_2^+ . In the dissociation channel (ii), two well separated ions are seen with an offset caused by the initial velocity of molecular samples. We do confirm that this ions are not produced by Coulomb explosion by counting the number of correlated electrons, which will be described in section 4.2.3. Also, a possible production mechanism of O^+ by ionization of CO_2 contaminated in OCS samples will be considered in section 4.2.5.

Electron

Figure 4.22 shows momentum images of electrons on the xy plane correlated with OCS^+ for different values of ellipticity, $\epsilon \sim 0$ (left) and $\epsilon \sim 0.84$ (right). Their major axis of the polarization are along the y axis for the linearly polarized pulse, and the z axis for the elliptically polarized pulse. The intensity is 1×10^{14} W/cm² for both pulses. Every

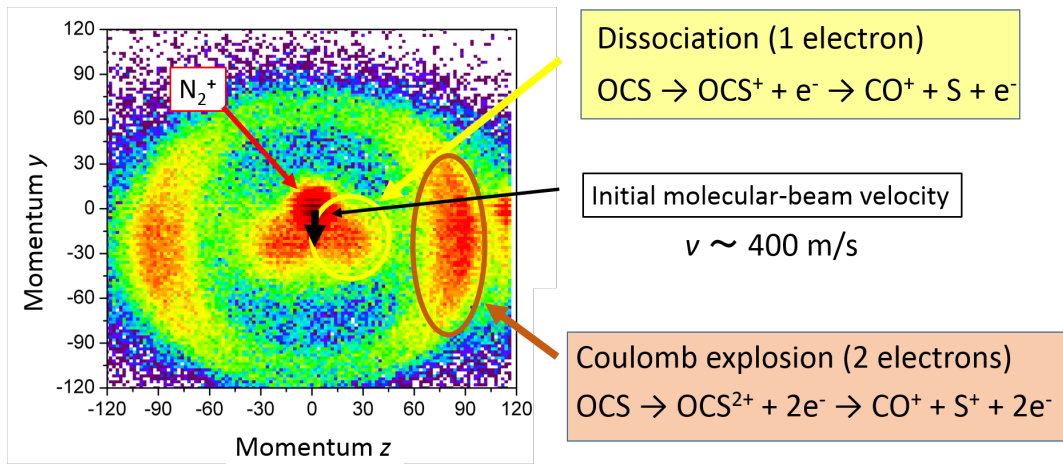


Figure 4.16: Momentum distributions of CO^+ in the xy plane at the laser intensity of $1 \times 10^{14} \text{ W/cm}^2$. The ellipticity of the pulse is $\epsilon \sim 0.84$. The major polarization axis is along the z axis.

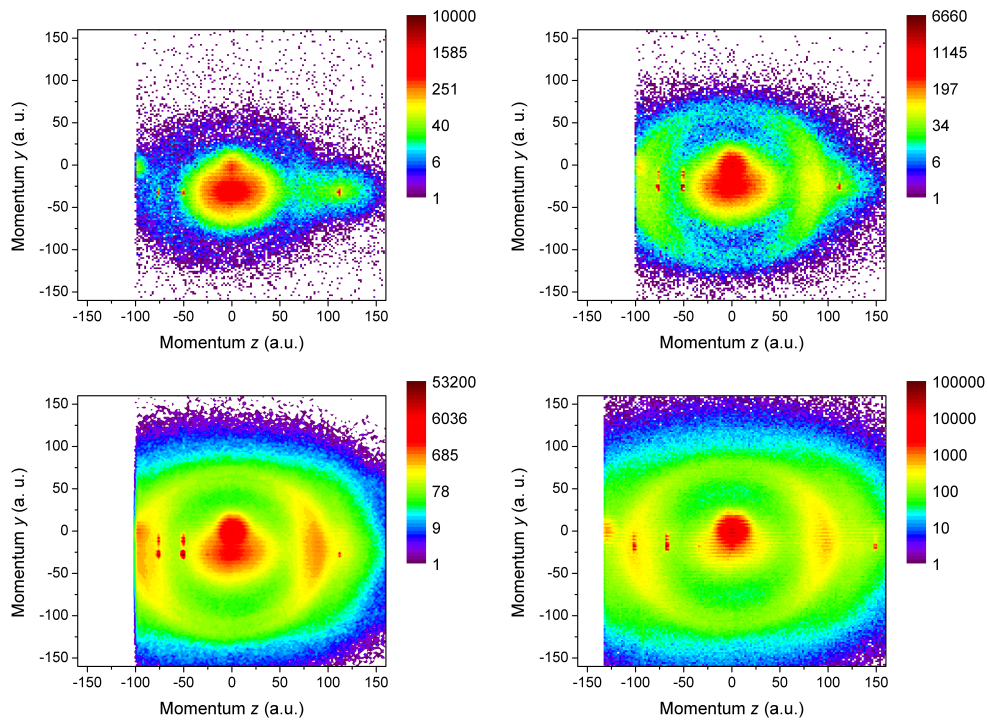


Figure 4.17: Momentum distributions of S^+ in the polarization plane (yz plane) at laser intensities of $5 \times 10^{13} \text{ W/cm}^2$ (upper left), $1 \times 10^{14} \text{ W/cm}^2$ (upper right), $1.5 \times 10^{14} \text{ W/cm}^2$ (lower left), and $2.2 \times 10^{13} \text{ W/cm}^2$ (lower right). The ellipticity of the pulse is $\epsilon \sim 0.84$. The major polarization axis is along the z axis.

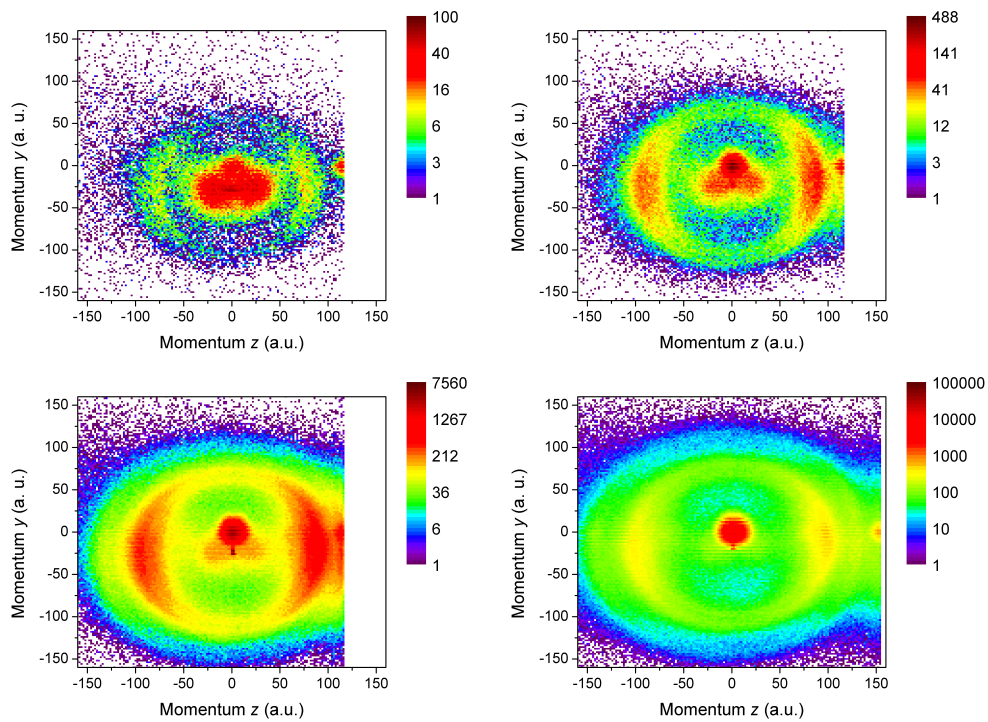


Figure 4.18: Same as figure 4.17, but for CO^+ cations.

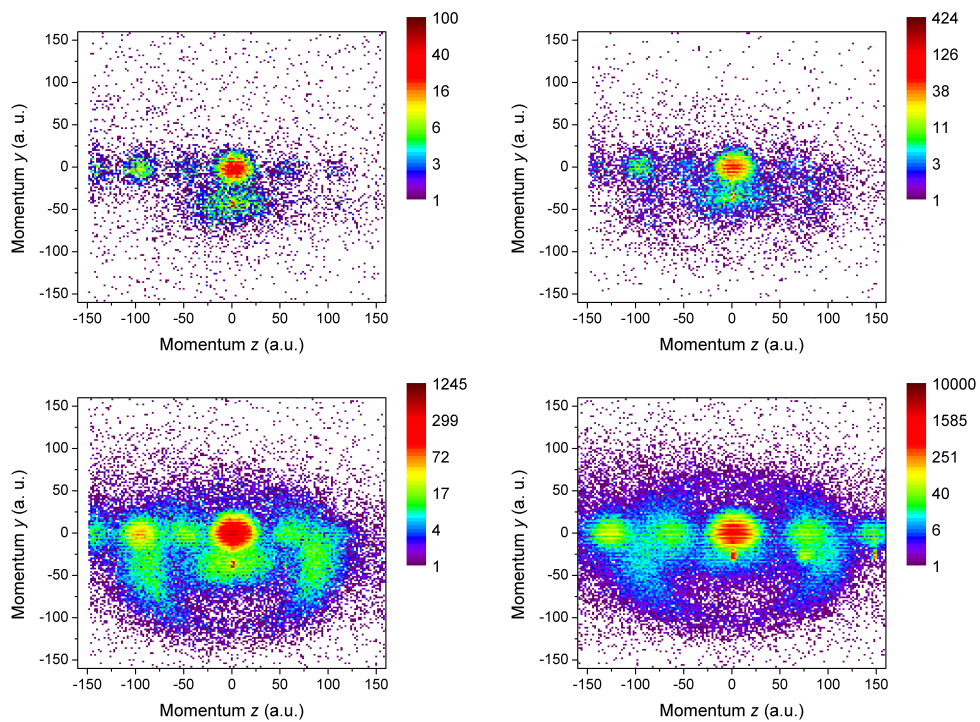


Figure 4.19: Same as figure 4.17, but for CS^+ cations.

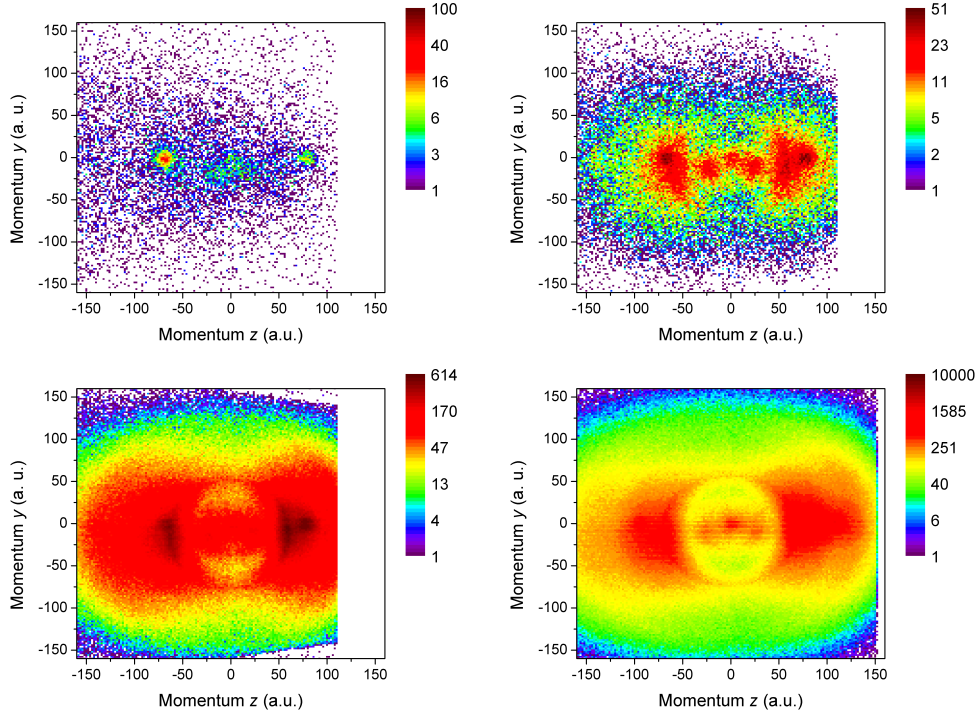


Figure 4.20: Same as figure 4.17, but for O^+ cations.

Table 4.3: Considered regions of the momentum for coincidence measurements. We define the region by the absolute momentum p_{\min} , p_{\max} , and the angle θ_{dis} with respect to the z axis. Atomic units are used.

Cation	p_{\min}	p_{\max}	θ_{dis}
S^+	20	66	$\pi/4$ and $\pi/8$
CO^+	10	50	$\pi/4$ and $\pi/8$
CS^+	14	44	$\pi/4$ and $\pi/8$
O^+	10	40	$\pi/4$ and $\pi/8$

electron is correlated with an OCS^+ ion. When linearly polarized pulses are used (upper left), the photoelectron distribution is confined along the polarization axis (y axis) with a maximum region located around the center $p_y \sim 0$. When ellipticity is increased from $\epsilon \sim 0$, the photoelectron distribution spreads along the minor axis of the polarization and the most intense momenta shift from the center to a higher point along the p_y axis.

4.2.3 Coincidence measurement

In order to estimate the emitted direction of photoelectrons with respect to the molecular frame, we employ the coincidence measurement of a single electron and a single fragment. By using an elliptically polarized pulse, the ionization probability is much higher when the electric field directs in the direction of major axis of the ellipse. Assuming an in-

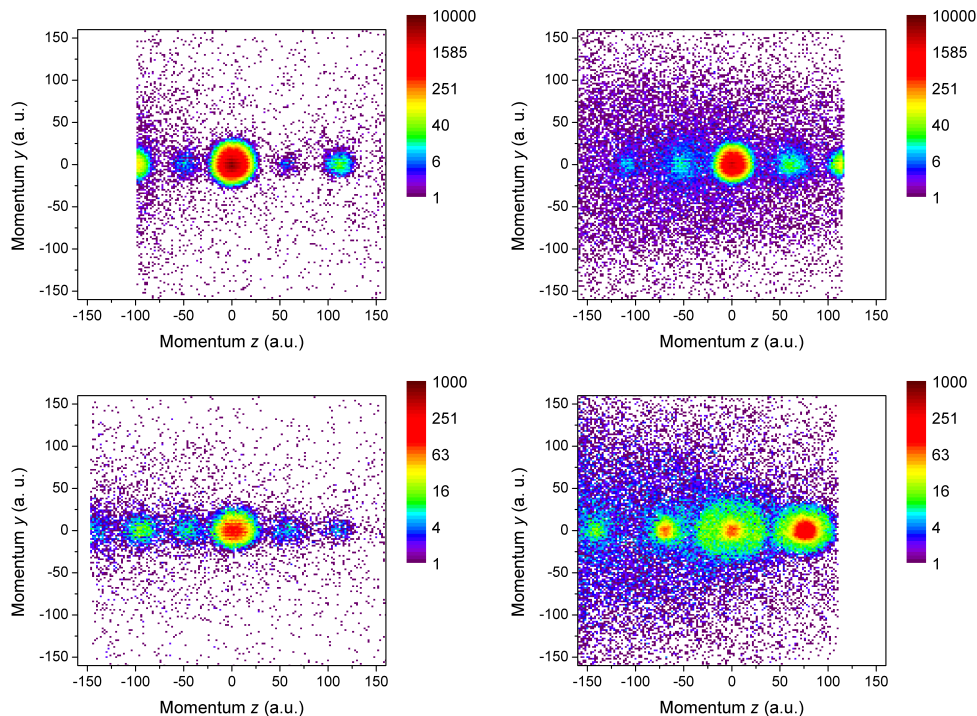


Figure 4.21: Momentum distributions without introducing OCS samples observed in the same TOF regions as S⁺ (upper right), CO⁺ (upper left), CS⁺ (lower left), and O⁺ (lower right). The laser intensity is 1.5×10^{14} W/cm². The ellipticity of the pulse $\epsilon \sim 0.84$. The major polarization axis is along the z axis.

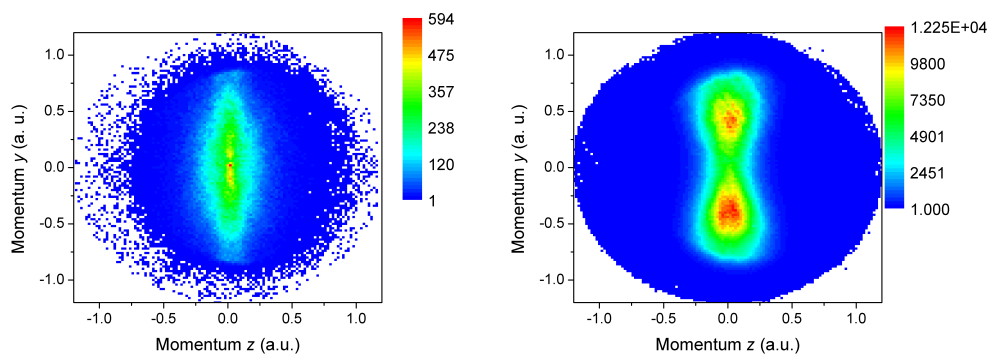


Figure 4.22: Momentum images of photoelectrons obtained with linearly polarized pulses (left) and elliptically polarized pulses (right) with the ellipticity $\epsilon \sim 0.84$. Their major axis of the polarization are along the y axis for the linearly polarized pulse, and the z axis for the elliptically polarized pulse. The intensity is 1×10^{14} W/cm² for both pulses. Every electron is correlated with an OCS⁺ ion.

stant dissociation, the direction of fragment ions represent the direction of the target molecule, and, with the help of angular streaking technique, explained in section 4.1.2, the ionization efficiency within the molecular frame can be obtained. Here note that the Coulomb explosion channel inevitably produces two electrons, which make the analysis more complicated. Therefore, in the following, we focus on the dissociated ion channels.

To analyze the coincidence event, we place the following restrictions on each event³: (i) single target cation (CO^+ , S^+ , O^+ , or CS^+) and single electron are detected. (ii) we only consider a specific region of the momentum for respective cations. The region R of the ion distribution is given by ⁴

$$R = \{(p, \theta, \phi) | p_{\min} < p < p_{\max}, 0 \leq \theta < \theta_{\text{dis}}, 0 \leq \phi \leq 2\pi\}, \quad (4.21)$$

where p , θ , and ϕ are the spherical polar coordinates in momentum space defined as

$$p_x = p \sin \theta \cos \phi \quad (4.22)$$

$$p_y = p \sin \theta \sin \phi \quad (4.23)$$

$$p_z = p \cos \theta. \quad (4.24)$$

The values of p_{\min} , p_{\max} , and θ_{dis} for each fragment are given in table 4.3.

Restriction (i) should be fulfilled for any coincidence measurement to prevent an accidental coincidence. With restriction (ii), the direction of the molecular axis is fixed along the z axis, and the correlated photoelectrons are in the molecular frame. The momentum regions are defined for each target cation such that the regions include the dissociated fragments but exclude the Coulomb exploded fragments and the background contributions (see figures 4.18–4.19). Finally, the molecular-frame photoelectron momentum distributions are obtained by selecting electron which meets the above restrictions. To better understand this analysis, we show how the momentum image of CO^+ is processed given with restrictions in figure 4.23 when the clockwise polarization of ellipticity $\epsilon \sim 0.84$ with the intensity of $1 \times 10^{14} \text{ W/cm}^2$ is employed.

The panel (a) in figure 4.23 shows the momentum image of CO^+ (same as shown in figure 4.18). The panel (b) shows the momentum image of CO^+ when no other ions are detected in the same event and the momentum is restricted (restriction (i) and (ii)). The panels (c) and (d) show the electron distributions correlated with the positive z -momentum p_z of dissociated CO^+ and the negative z -momentum p_z of them shown in the panel (b) in figure 4.23. The molecular axis is fixed to the z axis within axial recoil-approximation; therefore, the photoelectron images are regarded as the MF-PADs projected on the xy plane. By projecting the momentum image in the panel (c) and (d)

³In a event a molecular jet and a laser pulse come across in the spectrometer.

⁴Note that this region R is shifted by p_y^{initial} (equation 4.20) to take account of the momentum shift by the initial velocity of molecular samples.

in figure 4.23 on y axis, we obtain the momentum distribution as shown in figure 4.24. In the left panels, momentum distributions p_y of electrons correlated with CO^+ having positive p_z (upper left) and negative p_z (middle left) are shown. For comparison, we plot in the bottom panel in figure 4.24 the momentum distribution of electrons correlated with the molecular ion $^{61}\text{OCS}^+$. In the right panels, the same distributions but changing the polarization from clockwise to counterclockwise are shown. This analysis allows us to cross check the experimental results [15, 23, 25]. They clearly have asymmetric distribution as a function of the momentum p_y in those MF-PADs depending on the polarization and the correlated ion' momentum p_z . In order to quantitatively evaluate the positive–negative asymmetry, we introduce the up/total ratio $R_{\text{up/total}}$ of the MF-PAD given by

$$R_{\text{up/total}} = \frac{\int_0^\infty dp_y \int_{-\infty}^\infty dp_x \rho(p_x, p_y)}{\iint_{-\infty}^\infty dp_y dp_x \rho(p_x, p_y)}, \quad (4.25)$$

where $\rho(p_x, p_y)$ is the electron distribution. In the case of CO^+ (figure 4.24), the up/total ratio $R_{\text{up/total}}$ for electrons correlated with positive p_z is smaller than 0.5, whereas the ratio $R_{\text{up/total}}$ for electrons correlated with negative p_z is larger than 0.5 when the clockwise polarization is employed. This situation reverses when changing the laser polarization from clockwise to counterclockwise. Tables 4.4–4.7 summarize how laser intensity and polarization affect the up/total ratios $R_{\text{up/total}}$ for each OCS fragment S^+ , CO^+ , CS^+ , and O^+ . We measured MF-PADs at four laser intensities $5 \times 10^{13} \text{ W/cm}^2$, $1 \times 10^{14} \text{ W/cm}^2$, $1.5 \times 10^{14} \text{ W/cm}^2$, and $2.2 \times 10^{14} \text{ W/cm}^2$ with two polarization conditions of clock wise elliptical polarization and counterclockwise elliptical polarization, in both polarization cases ellipticity is $\epsilon \sim 0.84$. The values of Keldysh parameter γ_{Keldysh} are 1.78, 1.26, 1.03, and 0.85 for the laser intensities of $5 \times 10^{13} \text{ W/cm}^2$, $1 \times 10^{14} \text{ W/cm}^2$, $1.5 \times 10^{14} \text{ W/cm}^2$, and $2.2 \times 10^{14} \text{ W/cm}^2$, respectively. In the tables, denoted by $p_{z, \pi/4(\pi/8)}^{+(-)}$, the ratios $R_{\text{up/total}}$ are calculated for MF-PADs which are correlated with the target cations which are distributed within the angle $\pi/4$ ($\pi/8$) with respect to the z axis and have positive (negative) momenta p_z^+ (p_z^-). The ratios $R_{\text{up/total}}$ correlated with $^{61}\text{OCS}^+$ cations are shown for comparison. As can be seen in figures 4.17–4.20, background gases may contribute to the MF-PADs measurements. To observe the effects of the background gases, we do the same measurements and analysis without introducing OCS samples. Those results are shown at the bottom lines of the tables 4.4–4.7. In principle, as explained above, the up/total ratio $R_{\text{up/total}}$ should be inverted against the baseline of $R_{\text{up/total}} = 0.5$ by changing from electrons with positive to negative p_z ions or by changing from clockwise to counterclockwise polarization. On the general tendency, the ratio $R_{\text{up/total}}$ follows the above relation on polarization and molecular axis as can be seen in table 4.4–4.7. However, because of statistical and machine-dependent reasons, the ratio $R_{\text{up/total}}$ has a few percent of de-

violation from 50 % also in the background signals without introducing OCS or in the electrons correlated with $^{61}\text{OCS}^+$ ions. In order to compensate these small errors, we average the four cases (positive and negative momentum for CW and CCW polarization) and introduce the degree of asymmetry $A_{\text{MF-PAD}}$ of the MF-PAD by taking the average as

$$A_{\text{MF-PAD}} = \Sigma_{\text{all}} [\sigma_{\text{sign}} \cdot (R_{\text{up/total}} - 0.5)] / \Sigma_{\text{all}} |\sigma_{\text{sign}}| \quad (4.26)$$

where the summation takes all cases (the direction of p_z and the different polarization) for each fragment. The σ_{sign} is defined such that the degree of asymmetry can be interpreted how the electron tunnels through the potential of an OCS, that is, when $A_{\text{MF-PAD}} > 0$, electrons are more likely to be ionized from the O atom of OCS molecules than from the S atom of OCS molecules, and when $A_{\text{MF-PAD}} < 0$, electrons are more likely to be ionized from the S atom of OCS molecules than from the O atom of OCS molecules. The values of σ_{sign} are listed in table 4.8 for all fragments. Note that for S^+ we neglect the events where the momenta p_z is negative because these signals overlap with the intense isotope signals of $^{61}\text{OCS}^{2+}$ and $^{62}\text{OCS}^{2+}$. Figure 4.25 shows the degree of asymmetry $A_{\text{MF-PAD}}$ for CO^+ and S^+ for various laser intensities. In order to check the validity of our analysis, we plot $A_{\text{MF-PAD}}$ for angle restrictions $\theta_{\text{dis}} \pi/4$ and $\pi/8$. It is clear that the asymmetry of the both cations increase as the intensity increases. In particular, as the intensity increases from $0.5 \times 10^{14} \text{ W/cm}^2$ to $1.0 \times 10^{14} \text{ W/cm}^2$ strong enhancements of the degree of asymmetry $A_{\text{MF-PAD}}$ are observed for all fragments. The selection of the momentum distribution range ($\pi/4$ and $\pi/8$) does not affect the asymmetry so much. These intensity-sensitive behavior of the degree of asymmetry $A_{\text{MF-PAD}}$ implies that the dissociation mechanism and the ionization mechanism are sensitive to the laser intensity as discussed in section 4.3.2.

4.2.4 Dissociation probability

As shown in figure 4.25, the degree of asymmetry $A_{\text{MF-PAD}}$ considerably differs for respective fragment ions event at a given laser intensity. This fact implies that the ionization efficiency depends not only on the directions between the polarization and the molecular axis but on the final state of the ionization, that is, the excited state of molecular ion which correlates with the specific fragment ions. Therefore, it is important to investigate the characteristics of fragment ions produced in the strong field ionization, by which theoretical investigations can be related to the experimental results. First, we evaluate the dissociation ratios of OCS^+ into various fragment ions by calculating the ratios of the numbers of detected fragments N_{CO^+} , N_{S^+} , N_{O^+} , and N_{CS^+} to the number of the detected cations N_{OCS^+} . Due to the detector system and the experimental conditions, the following precautions ,(i) and (ii), are taken to count the number of fragment ions,

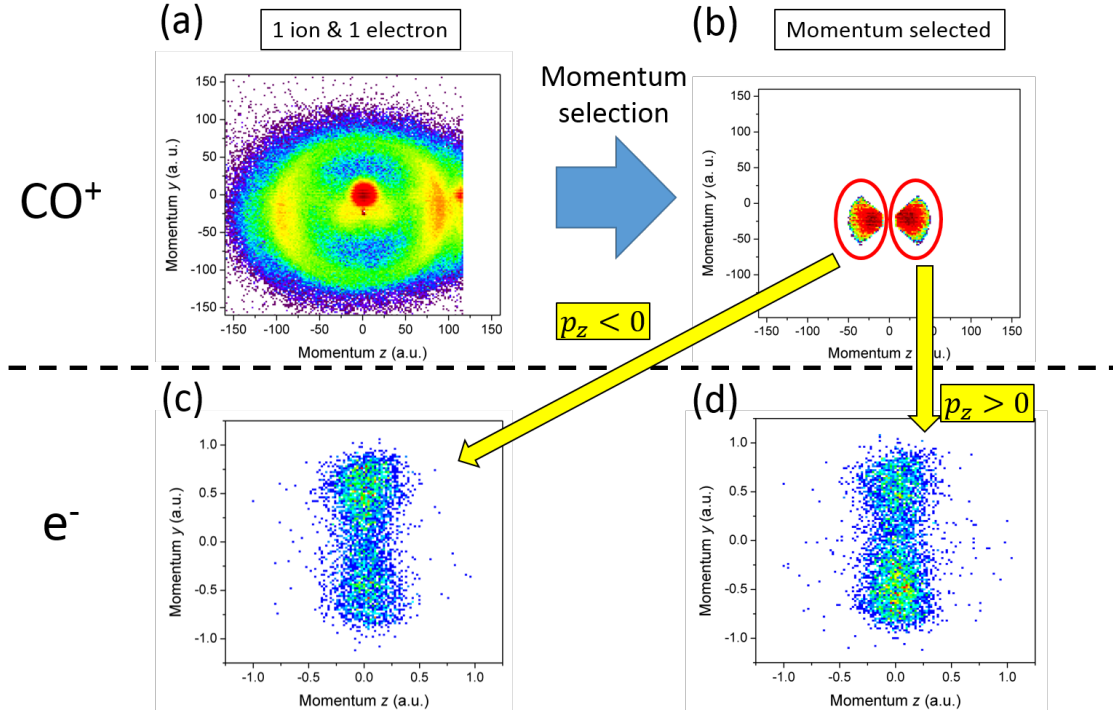


Figure 4.23: Coincidence analysis of events where a single CO^+ and a single electron are detected. The clockwise polarization of ellipticity $\epsilon \sim 0.84$ with the intensity of $1 \times 10^{14} \text{ W/cm}^2$ is employed. (a) The momentum distribution of CO^+ . (b) Selected momentum distribution with the angle restriction $\theta_{\text{dis}} = \pi/8$ and absolute value momentum restriction (see table 4.3). (c) Momentum distribution of electrons which are correlated with the ion with negative p_z values, which are indicated by a left circle in (b). (d) Momentum distribution of electrons which are correlated with the ion with positive p_z values, which are indicated by the right circle in (b).

Table 4.4: The up/total ratios $R_{\text{up/total}}$ with the ellipticity ~ 0.84 . The MF-PADs are correlated with positive z -axis momenta p_z^+ and negative z -axis momenta p_z^- of S^+ . The distributions of momenta are selected within angles of $\pi/4$ ($p_{z,\pi/4}^+$ and $p_{z,\pi/4}^-$), and $\pi/8$ ($p_{z,\pi/8}^+$ and $p_{z,\pi/8}^-$), for each case. The up/total ratios correlated with $^{61}\text{OCS}^+$ cations are listed in the right column. For comparison, the up/total ratios $R_{\text{up/total}}$ without introducing OCS samples are shown in the bottom line. Uncertainties are given in parentheses after the corresponding last digits. Values larger than 50 % are colored red, and values smaller than 50 % are colored blue.

Intensity (W/cm^2)	$p_{z,\pi/4}^+, p_{z,\pi/8}^+$	$p_{z,\pi/4}^-, p_{z,\pi/8}^-$	Reference
5×10^{13} (CW)	48.6(2), 49.4(4)	46.4(2), 46.0(4)	50.7
5×10^{13} (CCW)	48.4(2), 47.6(4)	50.2(2), 50.4(4)	51.9
1×10^{14} (CW)	53.1(2), 54.8(4)	47.1(2), 47.4(2)	50.8
1×10^{14} (CCW)	47.9(3), 46.3(5)	51.3(2), 50.3(3)	52.0
1.5×10^{14} (CW)	54.1(1), 55.1(3)	47.2(1), 47.9(1)	47.6
1.5×10^{14} (CCW)	46.3(2), 46.7(3)	52.4(1), 51.5(1)	48.5
2.2×10^{14} (CW)	53.9(2), 54.4(3)	46.4(2), 46.6(3)	47.9
2.2×10^{14} (CCW)	47.9(2), 47.4(4)	55.3(2), 55.8(4)	48.7
1.5×10^{14} (CW)	55.41, 47.22	51.67, 48.44	n/a

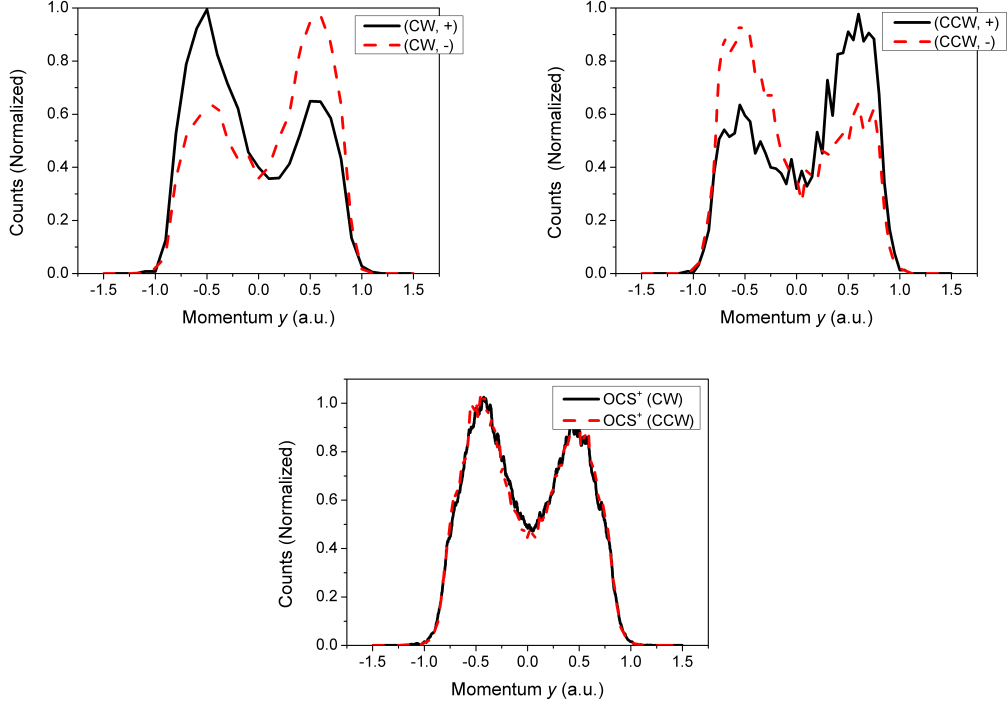


Figure 4.24: Upper figures show momenta of electrons along the y axis correlated with CO^+ having positive p_z (+) and negative p_z (-) with elliptically polarized pulses rotating clockwise (CW) and counterclockwise (CCW). The lower figure shows electron distributions correlated with $^{61}\text{OCS}^+$ with the same pulses.

Table 4.5: Same as table 4.4, but the correlated fragments are CO^+ .

Intensity (W/cm^2)	$p_{z,\pi/4}^+, p_{z,\pi/8}^+$	$p_{z,\pi/4}^-, p_{z,\pi/8}^-$	Reference
5×10^{13} (CW)	45.2(5), 46.3(8)	52.2(5), 54.8(9)	50.7
5×10^{13} (CCW)	52.4(5), 51.7(8)	47.6(5), 50.1(10)	51.9
1×10^{14} (CW)	43.1(5), 44.4(9)	59.2(5), 61.1(9)	50.8
1×10^{14} (CCW)	58.4(6), 56.9(10)	42.0(6), 43.6(11)	52.0
1.5×10^{14} (CW)	41.3(3), 40.1(6)	58.5(4), 61.1(7)	47.6
1.5×10^{14} (CCW)	59.7(4), 60.0(5)	41.7(4), 41.9(7)	48.5
2.2×10^{14} (CW)	50.5(2), 48.3(6)	56.5(3), 57.5(7)	47.9
2.2×10^{14} (CCW)	56.6(3), 57.8(6)	47.7(4), 44.4(8)	48.7
1.5×10^{14} (CW)	54.96, 55.93	53.00, 52.8	n/a

Table 4.6: Same as table 4.4, but the correlated fragments are CS^+ . Signals are too weak to measure the ratios $R_{\text{up}/\text{total}}$ without introducing OCS samples.

Intensity (W/cm^2)	$p_{z,\pi/4}^+, p_{z,\pi/8}^+$	$p_{z,\pi/4}^-, p_{z,\pi/8}^-$	Reference
5×10^{13} (CW)	51.2(19), 43.8(33)	45.8(19), 42.9(33)	50.7
5×10^{13} (CCW)	46.9(20), 37.3(29)	56.6(21), 58.1(44)	51.9
1×10^{14} (CW)	62.4(17), 73.8(25)	36.9(17), 21.6(24)	50.8
1×10^{14} (CCW)	40.4(19), 37.3(33)	60.7(17), 60.0(34)	52.0
1.5×10^{14} (CW)	56.5(11), 55.1(21)	39.2(11), 35.47(24)	47.6
1.5×10^{14} (CCW)	40.5(12), 35.0(23)	61.0(12), 70.1(20)	48.5
2.2×10^{14} (CW)	55.4(9), 61.3(23)	46.6(11), 49.8(22)	47.9
2.2×10^{14} (CCW)	48.6(9), 39.2(24)	59.4(11), 62.1(28)	48.7
1.5×10^{14} (CW)	n/a	n/a	n/a

Table 4.7: Same as table 4.4, but the correlated fragments are O^+ .

Intensity (W/cm^2)	$p_{z,\pi/4}^+, p_{z,\pi/8}^+$	$p_{z,\pi/4}^-, p_{z,\pi/8}^-$	Reference
5×10^{13} (CW)	64.2(24), 75.0(35)	46.7(26), 40.9(42)	50.7
5×10^{13} (CCW)	54.0(25), 58.1(40)	55.6(26), 54.8(44)	51.9
1×10^{14} (CW)	59.9(9), 61.1(14)	37.8(10), 36.6(16)	50.8
1×10^{14} (CCW)	40.2(10), 41.6(18)	60.5(11), 61.6(19)	52.0
1.5×10^{14} (CW)	61.4(4), 63.3(6)	36.3(4), 36.2(7)	47.6
1.5×10^{14} (CCW)	38.1(4), 38.5(7)	62.7(4), 63.1(7)	48.5
2.2×10^{14} (CW)	56.7(3), 59.3(3)	40.3(3), 37.8(5)	47.9
2.2×10^{14} (CCW)	43.3(3), 43.6(6)	61.6(4), 62.7(6)	48.7
1.5×10^{14} (CW)	50.78, 50.84	47.49, 50.00	n/a

Table 4.8: The values of the signs σ_{sign} used in equation 4.26. For S^+ the events where the momentum p_z is negative are neglected because the signal overlaps with the isotopes of OCS^{2+} .

Cation	$p_{z,\pi/4}^+, p_{z,\pi/8}^+$	$p_{z,\pi/4}^-, p_{z,\pi/8}^-$
S^+ (CW)	1	0
S^+ (CCW)	-1	0
CO^+ (CW)	-1	1
CO^+ (CCW)	1	-1
CS^+ (CW)	1	-1
CS^+ (CCW)	-1	1
O^+ (CW)	-1	1
O^+ (CCW)	1	-1

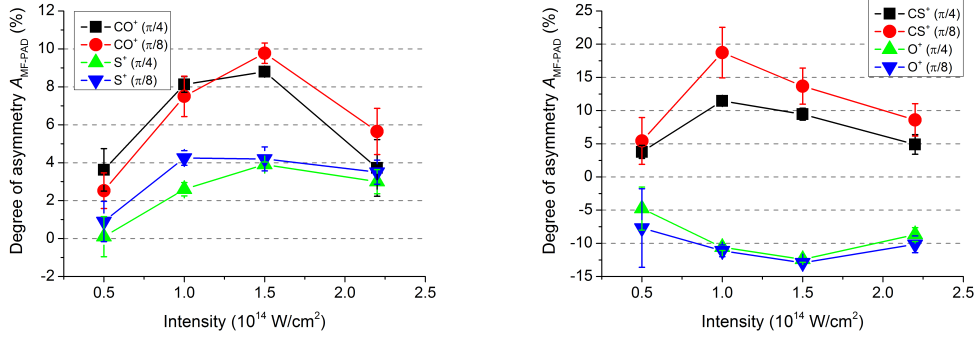


Figure 4.25: Degrees of asymmetry of MF-PADs $A_{\text{MF-PAD}}$ defined in equation (4.26) for the S-loss dissociation cations (left) and the O-loss dissociation cations (right) as a function of the laser intensity. The two momentum distributions d_{dis} ($\pi/4$ and $\pi/8$) with respect to the major polarization axis are considered for each fragment. For S^+ we neglect the event where the momentum p_z is negative because those signals overlap with the isotopes of OCS^{2+} . The values of Keldysh parameter γ_{Keldysh} are 1.78, 1.26, 1.03, and 0.85 for the laser intensities of $5 \times 10^{13} \text{ W/cm}^2$, $1 \times 10^{14} \text{ W/cm}^2$, $1.5 \times 10^{14} \text{ W/cm}^2$, and $2.2 \times 10^{14} \text{ W/cm}^2$, respectively.

depending on the specific ion.

(i) OCS^+

The cations OCS^+ have a small momentum distribution due to the cold translational temperature. So, the efficiency of multi-hit detection of OCS^+ is expected to be very low because of the dead time of the detector. Under typical experimental conditions, an OCS^+ is detected every three laser shots. We expect many OCS^+ events to be missing. Therefore, we used the third-most-probable isotope of OCS, $^{61}\text{OCS}^+$, as reference cation. Under typical experimental conditions, $^{61}\text{OCS}^+$ is detected once per 100 laser shots. Therefore, a multi-hits with ^{61}OCS are rare: a few percent of hits is multi-hit events⁵.

We use the same gas cylinder throughout this experiment, and the experiment was performed over a period of about 2 months. The ratio $^{61}\text{OCS}/^{60}\text{OCS}$ is expected to remain constant throughout the experiments. We measure the abundance of isotopes of OCS molecules by decreasing the counting rate of ^{60}OCS to lower than 10^{-2} , which eliminates the effect of the multi-hit of ^{60}OCS . At the laser intensity $1.5 \times 10^{13} \text{ W/cm}^2$ and $3.5 \times 10^{13} \text{ W/cm}^2$, the count rates are $\sim 10^{-3}$ and $\sim 10^{-2}$, respectively. Table 4.9 shows the measured abundance R_{low} and R_{high} of the isotopes of OCS molecules at the lower intensity and the higher intensity, respectively, and calculated proportions using the representative isotopes of oxygen, carbon, and sulfur.

We confirm that the measured abundance of ^{60}OCS is in agreement with the repre-

⁵ Assuming $(1-x)^N = S$, where $x (\ll 1)$ ionization rate, $N (\gg 1)$ number of molecules, $S (\sim 1)$ probability of no ionization event in a laser shot, the probability of double hits against single hit is given by $\ln S^{-1}$. When $S = 1 - 10^{-M}$, $\ln S^{-1} \approx 10^{-M}$.

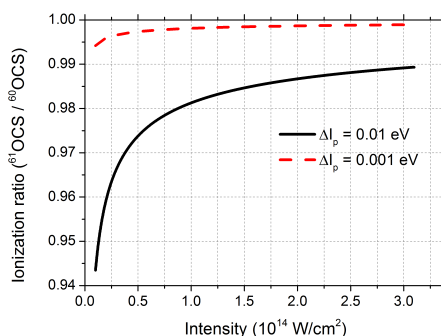


Figure 4.26: Calculated ionization ratio between ^{60}OCS and ^{61}OCS by the ADK theory. The ionization potential of ^{61}OCS is assumed to be higher than that of ^{60}OCS by 0.01 eV, which is the same value of the ionization potential difference between H_2 and HD . The ionization potential of ^{60}OCS is 11.19 eV [62].

sentative isotopes within the statistical errors.

To avoid the effect of the multi-hit, we use the measured abundance R_{low} to calibrate the number of ^{60}OCS cations in the following calculations of dissociation rates.

Finally, we consider the isotopic shifts of ionization potentials of molecules due to coupling of the electronic structure and the nuclear structure [129, 130]. For example, the ionization potentials of H_2 , HD , and D_2 are 15.43 eV, 15.44 eV, and 15.47 eV, respectively⁶ [62]. In the case of OCS molecules, we expect the isotope shift of the ionization potential is negligibly small because the HOMO of OCS molecules is not localized around the nuclei; therefore, the coupling of the electronic structure and the nuclear structure rarely happens. This can be seen in the difference of ionization potentials between H_2^{16}O and H_2^{18}O , 0.000 eV for the HOMO and 0.316 eV for the inner O_{1s} orbital, respectively [129]. Nevertheless, to estimate the error in measuring the abundance of ^{61}OCS , we calculate the ionization rates of the isotopes of OCS molecules by assuming the ionization potential of ^{61}OCS is higher than that of ^{60}OCS by $\Delta I_p = 0.01$ eV, which is the same value of the ionization potential difference between H_2 and HD , and by $\Delta I_p = 0.001$ eV, which is a still larger difference than that for H_2O isotopes (H_2^{16}O and H_2^{18}O). Figure 4.26 shows that the ratio of the ionization rates as a function of the laser intensity. Even with the apparently overestimated ionization difference $\Delta I_p = 0.01$ eV, the existence ratio of ^{61}OCS to ^{60}OCS can be measured accurately within 10 %, which is comparable to the standard errors in the measurements (see figure 4.9). Therefore, we can for sure say that the isotopic effect on the ionization potential of OCS molecules is negligible in our experiment.

⁶Note that the zero-point energy of D_2 and HD is lower than that of H_2 .

Table 4.9: The calculated and measured values of the existence ratios of isotopes of an OCS molecule. The most probable isotope, ^{60}OCS , has 30 protons (p) and 30 neutrons (n). The calculation is done by using the representative isotopic composition of oxygen, carbon, and sulfide. The measured data R_{low} and R_{high} are taken at the laser intensity of $1.5 \times 10^{13} \text{ W/cm}^2$ and $3.5 \times 10^{13} \text{ W/cm}^2$, respectively. Uncertainties are given in parentheses after the corresponding last digits. $a[b] = a \times 10^b$.

p+n	calculated	R_{low}	R_{high}
60	93.7 %	94.11(4) %	92.96(4) %
61	1.80 %	1.78(10) %	1.84(8) %
62	4.44 %	4.11(13) %	5.21(15) %
63	5.10[-2] %	n/a	n/a
64	2.85[-2] %	n/a	n/a

(ii) Dissociated fragments

As explained in section 4.2.2, the momentum images of fragments CO^+ , S^+ , O^+ , and CS^+ have two regions together with background signals: one related to the dissociation of OCS^+ and the other related to the Coulomb explosion of OCS^{2+} . Here we focus on the dissociation events. To accurately count the number N_{CO^+} , N_{S^+} , N_{O^+} , and N_{CS^+} of the dissociated cations, we separate the Coulomb exploded cations and from background ions by selecting ions with absolute momenta below a specific value p_{max} for each fragment (see table 4.3.). The background ions (for example, N_2^+ in CO^+ region and O_2^+ in S^+ region) are separated by the difference of the velocity of molecular samples. Here, ions from background gases and a molecular beam have different momenta of the center of mass than those from a molecular beam due to the velocity of the molecules in the molecular beams, the two still overlap due to the spread in momentum. We neglect the overlapped regions (upper half), integrate the non-overlapped regions (lower half), and double the result of the integration. For S^+ , the isotopes of OCS^{2+} overlap with S^+ momentum distribution. This contribution can be eliminated by selecting ions with momenta, $p_z > 0$. Finally, we obtain the number of the dissociated S^+ fragments by multiplying the number of selected ions by four. Figure 4.27 shows the procedure for CO^+ (upper) and S^+ (lower). Table 4.10 gives the ratios $R_{\text{fragment}} = N_{\text{fragment}}/N_{\text{OCS}^+}$ for several experimental conditions. We plot the ratios as a function of laser intensity in figure 4.28 by taking the average values of the ratios for the CW cases and the CCW cases. The ratios tends to increase as a function of the laser intensity from $5 \times 10^{13} \text{ W/cm}^2$ to $2.2 \times 10^{14} \text{ W/cm}^2$. But the ratios R_{S^+} and R_{CO^+} decreases from the laser intensity of $1.5 \times 10^{14} \text{ W/cm}^2$ to the laser intensity of $2.2 \times 10^{14} \text{ W/cm}^2$. This decreasing behavior is expected to be caused by sequential ionization of dissociation states of OCS^+ , which can be seen in the momentum distributions of S^+ and CO^+ at the laser intensity

of 2.2×10^{14} W/cm², there are fewer dissociation signals (figure 4.17 and figure 4.18).

We now evaluate these dissociation probabilities $P_{\text{dis}}^{\text{fragment}}$:

$$\text{OCS}^+ \xrightarrow{\text{(dissociation)}} \begin{cases} \text{S}^+ + \text{CO} \text{ with probability } P_{\text{dis}}^{\text{S}^+} \\ \text{CO}^+ + \text{S} \text{ with probability } P_{\text{dis}}^{\text{CO}^+} \\ \text{CS}^+ + \text{O} \text{ with probability } P_{\text{dis}}^{\text{CS}^+} \\ \text{O}^+ + \text{CS} \text{ with probability } P_{\text{dis}}^{\text{O}^+} . \end{cases} \quad (4.27)$$

There are four dissociation paths for OCS⁺. Therefore, the dissociation probability P_{dis} for each path is given by

$$P_{\text{dis}}^{\text{fragment}} = \frac{N_{\text{fragment}}}{N_{\text{OCS}^+} + N_{\text{S}^+} + N_{\text{CO}^+} + N_{\text{CS}^+} + N_{\text{O}^+}}. \quad (4.28)$$

In our experiment the dissociation probability meets $P_{\text{dis}}^{\text{fragment}} \ll 1$ so that $N_{\text{S}^+} + N_{\text{CO}^+} + N_{\text{CS}^+} + N_{\text{O}^+} \ll 1$, the probability of dissociation into each fragment path can be calculated as

$$P_{\text{dis}}^{\text{fragment}} \approx \frac{N_{\text{fragment}}}{N_{\text{OCS}^+}} = R_{\text{fragment}}, \quad (4.29)$$

which enables us to compare the dissociation probabilities with a theory.

Next, we calculate the dissociation probability by a simple tunneling model where the tunnel ionization into the states of OCS⁺ occurs with a probability given by the ADK theory (equation 2.4) [7]. The ionization rate is given by the ionization potential for each state. As will be described in detail in section 4.3.2, the ground state X²Π of OCS⁺ is stable, while the excited states A²Π, B²Σ⁺, and C²Σ⁺ of OCS⁺ decay into fragments. It is well known that S⁺ cations are produced from the A, B, and C states, and CO⁺ and CS⁺ cations are produced from the C state. The dissociation path for O⁺ fragments are unclear. The ionization pathways are given below with the ionization probabilities into these states $\Gamma_{\text{ADK}}^{\text{circular}} [I_p]$:

$$\text{OCS} \xrightarrow{\text{(ionization)}} \begin{cases} \text{OCS}^+(\text{X}) \text{ with probability } \Gamma_{\text{ADK}}^{\text{circular}} [I_p(\text{X})] \\ \text{OCS}^+(\text{A}) \text{ with probability } \Gamma_{\text{ADK}}^{\text{circular}} [I_p(\text{A})] \\ \text{OCS}^+(\text{B}) \text{ with probability } \Gamma_{\text{ADK}}^{\text{circular}} [I_p(\text{B})] \\ \text{OCS}^+(\text{C}) \text{ with probability } \Gamma_{\text{ADK}}^{\text{circular}} [I_p(\text{C})], \end{cases} \quad (4.30)$$

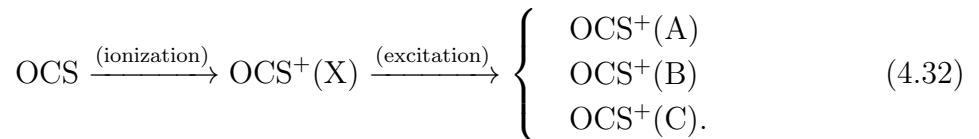
where $I_p(\text{X})$, $I_p(\text{A})$, $I_p(\text{B})$, and $I_p(\text{C})$ are ionization potentials of an OCS molecule into the X, A, B, and C states, respectively, and $\Gamma_{\text{ADK}}^{\text{circular}} [I_p]$ is given in equation (2.4). The dissociation probabilities $P_{\text{dis}}(\text{A})$, $P_{\text{dis}}(\text{B})$, $P_{\text{dis}}(\text{C})$ for three pathways (via the A, B, and C states) are given by

$$P_{\text{dis}}(\text{excited state}) = \frac{\Gamma_{\text{ADK}}^{\text{circular}} [I_p(\text{excited state})]}{\Gamma_{\text{ADK}}^{\text{circular}} [I_p(\text{X})]}, \quad (4.31)$$

Table 4.10: Ratios of the number of CO^+ cations R_{CO^+} and S^+ cations R_{S^+} to the number of OCS^+ cations for different laser intensities. The ellipticity is $\epsilon \sim 0.84$. The ratios for clockwise (CW) and counterclockwise (CCW) rotating polarizations are shown. $a[b] = a \times 10^b$.

Intensity (W/cm^2)	R_{S^+}	R_{CO^+}	R_{CS^+}	R_{O^+}
5×10^{13} (CW)	5.66[-3]	4.22[-4]	2.35[-5]	1.46[-5]
5×10^{13} (CCW)	5.08[-3]	5.08[-4]	2.21[-5]	1.37[-5]
1×10^{14} (CW)	1.26[-2]	1.54[-3]	7.81[-5]	2.27[-4]
1×10^{14} (CCW)	1.09[-2]	1.41[-3]	7.13[-5]	1.83[-4]
1.5×10^{14} (CW)	2.16[-2]	3.62[-3]	1.88[-4]	1.19[-3]
1.5×10^{14} (CCW)	1.95[-2]	3.20[-3]	1.69[-4]	1.01[-3]
2.2×10^{14} (CW)	1.68[-2]	3.35[-3]	6.68[-4]	5.16[-3]
2.2×10^{14} (CCW)	1.57[-2]	2.88[-3]	5.50[-4]	4.84[-3]

We plot the dissociation probabilities for the A, B, and C states as a function of the laser intensity in figure 4.28 together with the measured ones R_{fragment} . The measured dissociation probabilities for S^+ and CO^+ fragments are much higher than the calculated dissociation probabilities for all states. The measured dissociation probabilities for CS^+ and O^+ fragments are much higher than the calculated dissociation probability for the C state. These results indicate that not only the direct tunnel ionization into excited electronic states but also multiphoton excitation processes after tunnel ionization occurs:



This situation may explain the observed larger dissociation probabilities than calculated ones because the multiphoton excitation of the X state decreases the number of detected OCS^+ cations N_{OCS^+} , and increases the number of the detected fragment ions N_{S^+} , N_{CO^+} , N_{CS^+} , and N_{O^+} . In section 4.3.2, we discuss possible dissociation mechanisms.

4.2.5 Reference experiment: CO_2 molecular sample

A comparison of the results for OCS molecules to the results for CO_2 molecules gives us a insight into the effect of the asymmetry in molecular structure on the MF-PADs. The electronic states of a CO_2 molecule is similar to those of an OCS molecule, replacing the O atom of the CO_2 molecule with an S atom, both of which belong to the same group in the periodic table of the elements. In addition, it is known that commercial OCS gas samples contain a small amount of CO_2 impurity, which may produce spurious CO_2^+ (the same mass as CS^+) and O^+ signals, and the effect of the impurity will be confirmed negligible below.

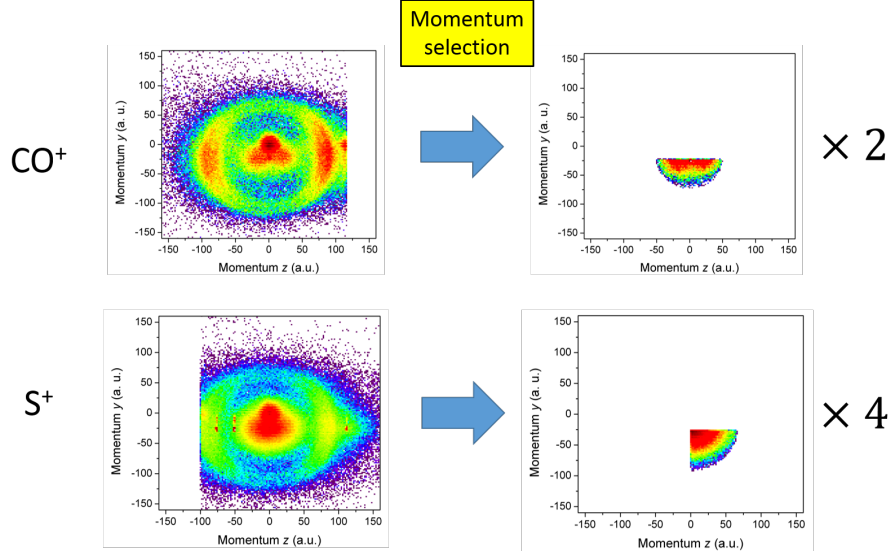


Figure 4.27: How to count the N_{CO^+} (upper) and N_{S^+} (lower). Upper left: momentum distribution of CO^+ . Upper right: selected momentum distribution of CO^+ . Lower left: momentum distribution of S^+ . Lower right: selected momentum distribution of S^+ . The laser intensity is $1 \times 10^{14} \text{ W/cm}^2$. The ellipticity is $\epsilon \sim 0.84$.

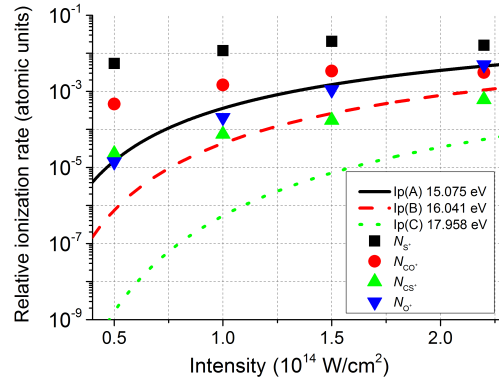


Figure 4.28: The measured dissociation rates R_{S^+} , R_{CO^+} , R_{CS^+} , and R_{O^+} are plotted in these figures. Relative ionization rates for ionic states A $^2\Pi$ (solid line), B $^2\Sigma^+$ (dashed line), and C $^2\Sigma^+$ (dotted line) of OCS^+ to the ground state $\text{X}^2\Pi$ of OCS^+ as a function of the laser intensity of the circularly polarized pulse. The ionization potentials for these excited states are given in Ref. [131]. The calculation is done by using the ADK theory (equation (2.4)).

Table 4.11: The up/total ratios $R_{\text{up/total}}$ with the ellipticity $\epsilon \sim 0.84$ for CO_2 samples. The MF-PADs are correlated with positive z -axis momenta p_z^+ and negative z -axis momenta p_z^- of CO^+ . The distributions of momenta are selected within angles of $\pi/4$ ($p_{z,\pi/4}^+$ and $p_{z,\pi/4}^-$), and $\pi/8$ ($p_{z,\pi/8}^+$ and $p_{z,\pi/8}^-$), for each case. The up/total ratios correlated with CO_2^+ cations are listed in the Reference column. Uncertainties are given in parentheses after the corresponding last digits.

Intensity (W/cm^2)	$p_{z,\pi/4}^+, p_{z,\pi/8}^+$	$p_{z,\pi/4}^-, p_{z,\pi/8}^-$	Reference
2.2×10^{14} (CW)	50.6(4), 51.5(7)	48.6(4), 50.5(9)	50.0
2.2×10^{14} (CCW)	49.8(4), 48.6(8)	49.5(4), 48.1(8)	50.0

Figure 4.29 shows the momentum distributions for CO^+ and O^+ cations, which have different characteristics than the momentum distributions of CO^+ and O^+ produced from OCS samples (see figure 4.18 for CO^+ and figure 4.20 for O^+). The momentum distribution of CO^+ (left panel of figure 4.29) consists of three momentum regions: (i) background molecular ions, (ii) dissociated CO^+ , (iii) CO^+ produced from CO_2^+ . This is similar situation to the case of OCS samples; however, the momentum distribution of the dissociated channels (ii) are not well separated along the major axis of the polarization, which are major difference in the momentum distributions between the case of CO_2 samples and OCS samples (see 4.18). In the momentum distribution of O^+ (right panel of figure 4.29), there are observed four distinctive regions: (i) dissociated O^+ . (ii) inner ring. (iii) outer ring. The rings are expected to be originated from CO^{2+} and CO^{3+} . Tables 4.11 and 4.12 show the up/total ratios $R_{\text{up/total}}$ of the MF-PADs correlated with CO^+ and O^+ , respectively. The ratios do not show clear dependence on the polarization nor on the direction of the momentum p_z of cations, which are different situations from that for OCS samples.

The degrees of asymmetry $A_{\text{MF-PAD}}$ are calculated to be 0.68(22), 1.32(25), 1.22(20), and 0.53(20) for CO^+ with $\pi/4$ distribution, CO^+ with $\pi/8$ distribution, O^+ with $\pi/4$ distribution, and O^+ with $\pi/8$ distribution, respectively. These values are much smaller than the results for OCS samples. Therefore, we obtain two conclusions: First, the effect of impurity of CO_2 in OCS samples is not a candidate which causes the asymmetry in MF-PADs correlated with O^+ . Second, the MF-PADs for symmetric molecular samples does not have asymmetry. Therefore, we suppose that the asymmetry caused by the direction of the electric field at the instant of the ionization does not play a role in the subsequent dissociation processes ⁷.

⁷For OCS molecules, asymmetry is caused by the direction of the molecular axis and the charge distribution, while for CO_2 molecules, asymmetry is caused by the charge distribution.

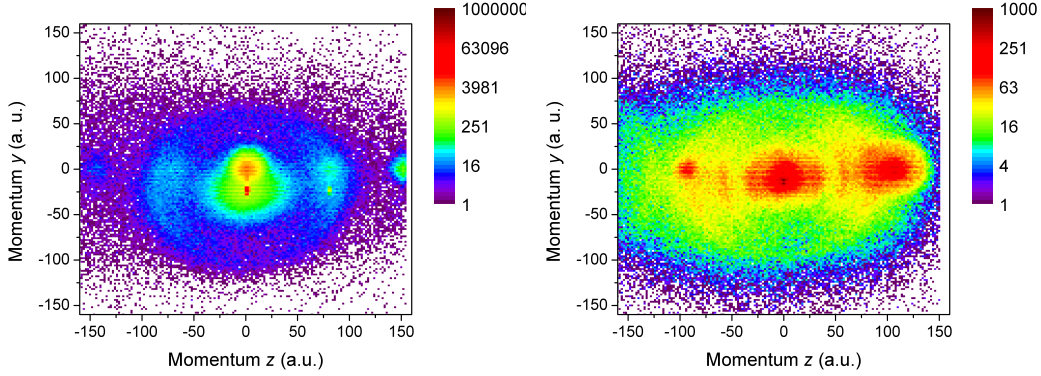


Figure 4.29: Momentum distributions of CO^+ (left) and O^+ (right) in the polarization plane (yz plane) at the laser intensity of $2.2 \times 10^{14} \text{ W/cm}^2$. The ellipticity of the pulse is $\epsilon \sim 0.84$. The major polarization axis is along the z axis.

Table 4.12: Same as table 4.11, but the correlated fragments are O^+ .

Intensity (W/cm^2)	$p_{z,\pi/4}^+, p_{z,\pi/8}^+$	$p_{z,\pi/4}^-, p_{z,\pi/8}^-$	Reference
2.2×10^{14} (CW)	50.7(5), 49.6(8)	48.2(5), 49.7(8)	50.0
2.2×10^{14} (CCW)	51.1(4), 48.8(7)	51.3(4), 49.8(7)	50.0

4.3 Discussion

4.3.1 MF-PADs calculated by the WFAT theory

In this section, we compare the experimental results with weak-field asymptotic theory (WFAT) by calculating the up/total ratios $R_{\text{up/total}}$ under our experimental conditions. The details of the theory are described in section 2.1. The electric field is given by

$$\mathbf{F}(\theta_\epsilon) = (F_z, F_y) = (F_0 \cos \theta'_\epsilon, \epsilon F_0 \sin \theta'_\epsilon), \quad (4.33)$$

where F_0 the maximum electric field, θ'_ϵ the orientation angle of the polarization ellipse, ϵ the ellipticity. To compare our experimental results with WFAT, we need to consider the angular distribution of the molecular axis of OCS molecules. The ionization rate $d\Gamma_{\text{calc}}$ is given by

$$d\Gamma_{\text{calc}} = \Gamma_{\text{WFAT}}(\theta'_\epsilon, \theta_m, \phi_m) P(\theta_m, \phi_m) d\theta_\epsilon d\Omega_m, \quad (4.34)$$

where $P(\theta_m, \phi_m)$ the angular distribution of the molecular axis, θ_m and ϕ_m are the polar and the azimuthal angles of the molecular axis of OCS, respectively. In our experiments, OCS molecules rotate freely, but the angular distribution of the molecular axis $P(\theta_m, \phi_m)$ can be obtained by observing momenta of dissociated fragments. We thus obtain the ionization rate $d\Gamma_{\text{calc}}$

$$d\Gamma_{\text{calc}} = |G_{00}(\vartheta)|^2 W_{00} [F(\theta'_\epsilon)] P(\theta_m, \phi_m) \sin \theta_m d\theta_m d\phi_m d\theta'_\epsilon, \quad (4.35)$$

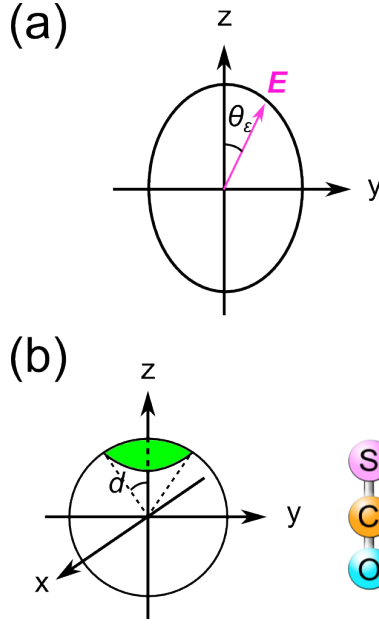


Figure 4.30: Geometry for the calculation. (a) The elliptically polarized electric field. (b) The angular distribution of the inter-nuclear molecular axis. When d_{axis} is small (~ 0), the OCS molecule is oriented with the S atom toward positive z . See text for details.

where ϑ is the angle between the molecular axis and the electric field, and is given by

$$\vartheta = \vartheta(\theta'_\epsilon, \theta_m, \phi_m) \quad (4.36)$$

$$= \arccos \{ \sin \theta_m \sin \phi_m \sin [\arctan(\epsilon \tan \theta'_\epsilon)] + \cos \theta_m \cos [\arctan(\epsilon \tan \theta'_\epsilon)] \}. \quad (4.37)$$

Assuming that the angular distribution $P(\theta_m, \phi_m)$ is given by

$$P(\theta_m, \phi_m) = 1 \text{ when } \theta_m < d_{\text{axis}} \text{ and} \quad (4.38)$$

$$= 0 \text{ when } \theta_m > d_{\text{axis}}, \quad (4.39)$$

where d_{axis} is the molecular angle with respect to the z axis, we obtain the ionization rate by equation (4.35). Figure 4.31 shows the ionization rate as a function of the angle of polarization with the ellipticity of 0.6 and 0.84 for different molecular axis distribution d_{axis} from 1° to 90° by integrating equation (4.35) over θ_m and ϕ_m . Note that the ionization rate is very sensitive to both ellipticity and the molecular axis distribution d_{axis} . For example, the up (0° - 90°)/total (0° - 180°) ratios $R_{\text{up/total}}$ of the photoelectron distributions drastically vary as the molecular axis distribution d_{axis} changes from 30° to 90° . This sensitivity can be understood by noting that the ionization rate has peaks at each of the angles of $\sim 27^\circ$ and $\sim 116^\circ$, and minima at each of the three angles of 0° , 61° , and 180° as shown in figure 2.1.

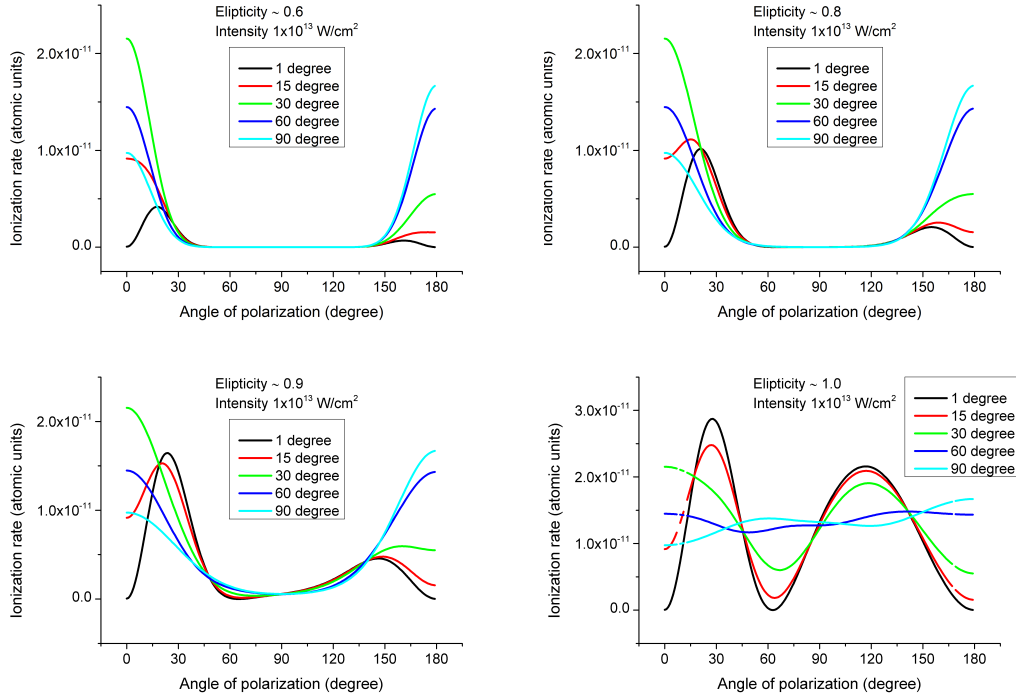


Figure 4.31: Ionization rate as a function of the orientation angle of the electric field with ellipticity of 0.6(upper left), 0.84(upper right), 0.9 (lower left), and 1.0(lower right) for various angular distributions d_{axis} of the molecular axis. The angular distribution d_{axis} is defined with respect to the z axis.

Table 4.13: up/total ratios $R_{\text{up/total}}$ for different values of ellipticity and the molecular axis distributions d_{axis} . Values larger than 50 % are colored red, and values smaller than 50 % are colored blue.

Ellipticity	$d < 1^\circ$	$d < 15^\circ$	$d < 30^\circ$	$d < 60^\circ$	$d < 90^\circ$
0.6	85.03 %	84.19 %	78.53 %	51.47 %	38.89 %
0.84	79.48 %	79.08 %	74.47 %	50.44 %	39.89 %
0.9	68.56 %	69.17 %	66.77 %	49.17 %	42.03 %
1.0	45.59 %	47.29 %	49.41 %	47.58 %	46.62 %

Table 4.14: The calculated energy, E , of excited states of an OCS^+ cation at the equilibrium bond lengths [132]. For clarity the energy of the ground state of the OCS cation is taken as a zero. The decay times and the dissociation fragments of those states are also listed.

state	$E[\text{eV}]$	$r_{\text{CO}}[\text{\AA}]$	$r_{\text{CS}}[\text{\AA}]$	Decay time	fragment
$\tilde{\text{X}}^2\Pi$	11.174 [131]	1.130	1.649	stable	n/a
$\tilde{\text{A}}^2\Pi$	15.075 [131]	1.290	1.575	110 ns [133]	S^+ [131, 128]
$\tilde{\text{B}}^2\Sigma^+$	16.041 [131]	1.146	1.569	80 ns[133]	S^+ [131, 128]
$\tilde{\text{C}}^2\Sigma^+$	17.958 [131]	1.180	1.545	unknown	S^+ , CO^+ , CS^+ [131, 128]

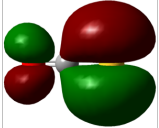

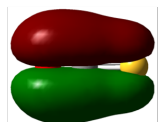
	Orbital (O=C=S)	Symmetry	Related cation state
HOMO		π	$X^2\Pi$
HOMO -1		σ	$B^2\Sigma^+$
HOMO -2		π	$A^2\Pi$

Figure 4.32: Images of the three highest occupied molecular orbitals, HOMO, HOMO-1, and HOMO-2. The O (S) atom of the OCS molecule is directing to the left (right). The symmetry and related cation states, which ionization of an electron in a molecular orbital causes, of each molecular orbital are shown.

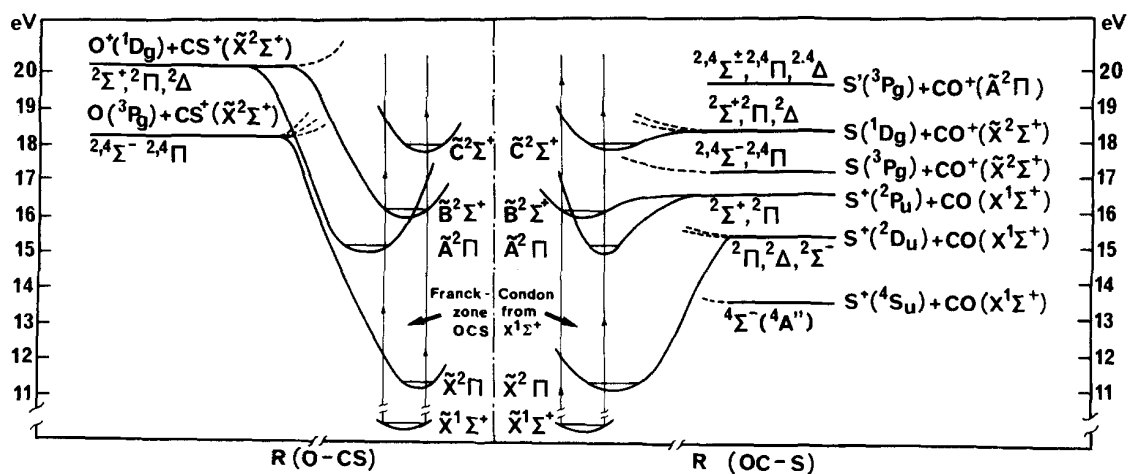


Figure 4.33: Potential surface of OCS^+ [134]. . The permission of reuse of this figure is given by AIP Publishing LLC with a license number 3557451426393.

4.3.2 Dissociation mechanism

In this subsection, we discuss previous studies on the dissociation of OCS^+ , and compare those results to our experimental results. We propose possible mechanisms of the dissociation observed in our experiments. Based on the above consideration, we examine the validity of obtained MF-PADs for each dissociated cation.

The valence electronic configuration of the ground state of OCS molecules is $\dots 8\sigma^2 9\sigma^2 2\pi^4 3\pi^4$ [132]. The lowest four states of OCS^+ , $X^2\Pi$, $A^2\Pi$, $B^2\Sigma^+$ and $C^2\Sigma^+$, can be well described by ionization of an electron from the 3π , 2π , 9σ and 8σ orbitals, respectively [132]. Table 4.14 shows the ionization potentials from the neutral ground state and symmetries for four lowest excited states of OCS^+ . These four ionic states are reported to be linear from photoelectron spectroscopy [134]. Other higher excited states have not been studied experimentally nor theoretically, to the best of our knowledge. Figure 4.33 shows ab initio potential surfaces of the ground and excited states of OCS^+ molecules calculated by Hirst [132]. Stable OCS^+ states are the ground state \tilde{X} and a fraction of the vibronic ground state of the \tilde{A} state, which emits fluorescence [128], while other states are repulsive or quasi-stable and easily decay into fragments. Morse *et al.* measured the branching ratios to ionic products from X, A, B, and C states of OCS^+ by a photoelectron-photoion coincidence measurement [128]. The A and B states decay producing S^+ , and the C state decays producing S^+ and CO^+ with a branching ratio $\sim 80\%$ and $\sim 20\%$, respectively. In 1994, Boesl *et al.* measured the decay time of OCS^+ [133]. They have revealed that the decay times of vibrationally-excited A state are longer than 15 ns for the bending modes, but those for stretching modes are smaller than 15 ns [133].

Chang *et al.* investigated dissociations of a mode-selected B state prepared by a double-resonance excitation scheme [135]. In their study two dissociation mechanisms are suggested. Internal conversion of the B state to the X state followed by the direct dissociation. Alternatively, a conical intersection between the B state and the A state followed by the dissociation via the intersection of the potential surface with the repulsive $^2\Delta$ surface. These mechanisms are examined by an ab-initio calculation by Hirst, and conclude that the both mechanisms are reasonable [132].

The \tilde{C} state correlates adiabatically with $\text{S}(^1\text{D}) + \text{CO}^+(\text{X}^+\Sigma^+)$, intersected by dissociative surfaces, $^4\Sigma^-$, $^2\Sigma^-$, and $^2\Delta$ [134, 132]. A coincidence experiment which was done by Morse *et al.* [128] showed the \tilde{C} state yield both S^+ and CO^+ .

Before moving on to the discussion for dissociation into specific fragments, we would like to stress that the multiphoton excitation processes contribute to the dissociation processes. We can see two evidences of the contributions in the dissociation probabilities measured for all dissociated fragments (see figure 4.28): First, the measured dissociation

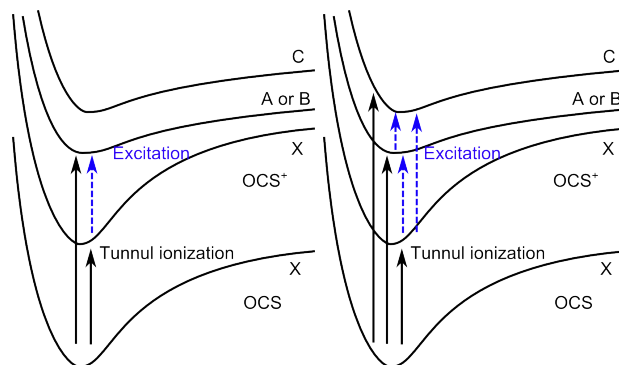


Figure 4.34: Schematic diagram of the dissociation mechanism of $\text{OCS}^+ \rightarrow \text{S}^+ + \text{CO}$ in the low intensity regime (left) and in the high intensity regime (right). Solid arrows represent the tunnel ionization. Dashed arrows represent the multiphoton excitation. The final states A, B, or C may dissociate into S^+ and CO.

probabilities for S^+ and CO^+ fragments are much higher than the dissociation probabilities for all states, and the measured dissociation probabilities for CS^+ and O^+ fragments are much higher than the dissociation probability for the C state. This implies multiphoton excitation from the ground state of OCS^+ molecules to the A, B, and C excited states. Second, At the highest intensity $2.2 \times 10^{14} \text{ W/cm}^2$, these dissociation probabilities are smaller than those at the intensity $1.5 \times 10^{14} \text{ W/cm}^2$, which can be explained by subsequent ionization of excited states (A, B, or C) of OCS^+ molecules by the laser pulse. In the rest of this section, keeping in mind the above discussion, we discuss each dissociation process.

Dissociation into $\text{S}^+ + \text{CO}$

All excited states introduced above, A, B, and C state, can decay into S^+ and CO. However, the A and B states decay much slower than the rotational period $T_{\text{rot}} = 82 \text{ ps}$ of OCS [133]. In this case, the momentum distribution does not correlate with the molecular axis during the ionization, which may explain why the momentum distributions of dissociated S^+ are near isotropic (see figure 4.17), and the value of the degree of asymmetry $A_{\text{MF-PAD}}$ is small at the low laser intensity $5 \times 10^{13} \text{ W/cm}^2$. However, we observe that the degree of asymmetry $A_{\text{MF-PAD}}$ grows as the laser intensity increases (see figure 4.25). This may be explained by considering the multiphoton excitation or the tunnel ionization from deep orbital described below. As the intensity increases, the ratio of the C state and the vibrationally excited A and B state to the lower-lying vibrational levels in A and B state become larger by the multiphoton excitation (bond softening) [125] or tunnel ionization from deep orbitals [15, 25]. Figure 4.34 schematically shows the mechanism. If the C state decays faster than the rotational period $T_{\text{rot}} = 82 \text{ ps}$ of OCS molecules, the orientation dependence of the ionization rate affects the MF-PADs

as in the case of the dissociation into $\text{CO}^+ + \text{S}$. We expect that the excitation from the A or the B state to the C state is probable because they have the same multiplicity and the similar equilibrium bond lengths [6].

Dissociation into $\text{CO}^+ + \text{S}$

As described above, we expect the decay of the C state is the major contribution to the dissociation path $\text{OCS} \rightarrow \text{CO}^+ + \text{S}$. Unfortunately, to the best of our knowledge the decay time of the C state has not been measured. In our experiment, the momentum distribution of CO^+ is extended along the major polarization axis. Therefore, We expect the decay time of the C state is much faster than the rotational period $T_{\text{rot}} = 82$ ps of OCS molecules. We now examine how the C state is populated during the interaction of OCS molecules with the pulse. The measured dissociation probability is much higher than the prediction by the ADK theory (see figure 4.28). Therefore, we expect that the population mechanisms by multiphoton excitations from the X, A, and B states into the C states after ionization are more probable than the direct tunnel ionization into the C state. Neglecting the contributions of the excited states A and B, almost all the electrons can be interpreted to be tunneled from the HOMO of OCS molecules, which may explain why electrons are more likely to be ionized from the O atom of OCS molecules than the S atom of OCS molecules [23].

Dissociation into $\text{CS}^+ + \text{O}$

The left side of figure 4.33 shows potential curves of OCS^+ as a function of the C–O bond length. The appearance potential for CS^+ dissociated from OCS^+ was reported to be ranging from 18 eV to 20 eV by several groups. For example, the first dissociation limit $\text{CS}^+ (\text{X}^2\Sigma^+) + \text{O} (^3P_g)$ was measured to be 18.56 eV [128], 18.22 eV [136], and 18.7 eV [137]. Hubin-Franshin *et al.* proposed that the dissociation into $\text{CS}^+ + \text{O}$ became accessible through vibrationally excited $\text{C}^2\Sigma^+$ state [131]. Very recently, Dong *et al.* studied this dissociation mechanism of the OCS^+ ion by the complete active space self-consistent-field and multiconfiguration second-order perturbation theory [138]. They suggested predissociation mechanisms of the OCS^+ via the $\text{C}^2\Sigma^+$ state.

The momentum distribution for this channel is nearly isotropic (figure 4.19), which is similar case for S^+ . However, the degree of asymmetry $A_{\text{MF-PAD}}$ is larger than that for S^+ and comparable to that for CO^+ (figure 4.25). These results indicate that some excited states decay into $\text{CS}^+ + \text{O}$ faster than the rotational period $T_{\text{rot}} = 82$ ps of OCS molecules. The increasing and decreasing behavior may indicate that the population ratio of these fast decay states vary as the laser intensity increases.

Dissociation into $O^+ + CS$

To the best of our knowledge, the dissociation mechanism of OCS^+ which produces O^+ fragment ions has not been studied. The study on the dissociation into $O^+ + CS$ is more rare than the dissociation into $O + CS^+$ because $O^+ + CS$ has higher energy than $O + CS^+$. In our experiment, the dissociated O^+ are well separated along the major polarization axis (see figure 4.20) and a clear asymmetry of MF-PAD is observed (see figure 4.25 and table 4.7). Therefore, we expect the decay time of the dissociation is much faster than the rotational period $T_{rot} = 82$ ps of OCS molecules.

The dissociation rate for O^+ is higher than those for CO^+ and CS^+ at the laser intensity of 2.2×10^{14} W/cm² (see figure 4.28) instead of the fact the adiabatic energy of the channel is largest. This result indicates that the saturation effects is important in this laser intensity regime $\sim 1 \times 10^{14}$ W/cm².

4.4 Summary

MF-PADs for OCS molecules by an intense elliptically polarized field have been observed for each correlated dissociation channel (S^+ , CO^+ , CS^+ , and O^+). These MF-PADs have the up/total asymmetry A_{MF-PAD} , which can be interpreted as angular-dependent ionization rates of OCS molecules. The asymmetry have different characteristics depending on the dissociated fragments. When CO^+ , S^+ , or CS^+ molecules are observed, the observed MF-PADs can be interpreted that electrons are more likely to be ionized from the O atoms of OCS molecules, while when O^+ molecules are observed, the observed MF-PADs can be interpreted that electrons are more likely to be ionized from the S atoms. We provide possible dissociation mechanisms by comparing the experimental results with previous studies on the dissociation of OCS^+ molecules ionized by synchrotron radiation or incoherent lights by atomic discharge. With the help of these studies, we have succeeded in qualitatively explaining the intensity-dependent asymmetry A_{MF-PAD} and fragment-dependent asymmetry A_{MF-PAD} . However, the inverse asymmetry of MF-PADs for O^+ fragments are yet to be understood fully. One of the reasons for that is the dissociation which produces O^+ has not been studied well.

Finally, the explanation we made are on many assumptions. For example, the C states decay much faster than the rotational period of OCS molecules and the multiphoton excitation after ionization is as probable as tunnel ionization into excited states. These assumptions could be confirmed by calculating the transition matrix. Using a few-cycle pulse would make the discussion clearer because the multiphoton excitation process is less likely to occur.

Chapter 5

Concluding remarks

In this work we have experimentally studied strong-field interaction with molecules where inversion symmetry is not preserved. Among a number of strong-field phenomena, we studied the process of high-order harmonic generation and the tunnel ionization, both of which are particularly important phenomena as described in chapter 1. The breaking of inversion symmetry is introduced by employing the CEP-controlled few-cycle pulses for experiments on the high-order harmonic generation, and by employing coincidence measurement of tunnel ionized OCS molecules for experiments on the tunnel ionization. We obtained novel information such as the harmonic chirp of high-order harmonics and molecular-orientation dependence of tunnel ionization rates, both of which are not obtained under conditions where inversion symmetry is preserved. In the rest of this chapter, we summarize the results and the outlook of the two experiments.

Results and Outlook

In chapter 3 we observed high-order harmonic spectra generated from aligned N₂ molecules and CO₂ molecules with CEP-controlled 10-fs pulses. The spectra showed fringes in the cutoff region which vary their shape depending on the relative values of the CEP. We analyzed the structure by employing Fourier analysis, and found three peaks in the Fourier spectrum. The positions (ΔT_i) did not change by varying the CEP and the non-linear medium. The phase ($\phi_{\text{Fourier}}^{\text{nth}}$) of these peaks were found to be linear with the value of the CEP for the 2nd and 3rd Fourier peaks, and independent with the value of the CEP for the 1st Fourier peaks.

To understand underlying physics, we performed two numerical calculations: a quantum-mechanical simulation (Lewenstein model) and a simple model simulation. Both of the two calculations reveal that the observed CEP-dependent spectra stemmed from the interference between attosecond pulses with a significantly large harmonic chirp. The simple model calculation predicted the magnitude of the harmonic chirps as $b > 0.6 \text{ fs}^{-2}$, which

is consistent with the result $b \sim 1.1(\pm 0.5) \text{ fs}^{-2}$ obtained with a well-known formula of intensity-dependent phase. Finally, we also examine the possibility of observing the harmonic phase change in the harmonic spectra generated from aligned CO_2 and N_2 . By applying inverse Fourier transform to the Fourier spectrum, we extracted the interference, the 2nd and 3rd Fourier peaks. We found phase changes and phase distortions in the region where the phase jump reportedly occurs. However, since the interference signals were very low, we found it rather difficult to provide a conclusive argument.

We revealed the mechanism of the CEP-dependent structure observed in harmonic spectra in the cutoff region. This mechanism offers the possibility of observing the magnitude of harmonic chirp b without direct measurements of the high-order harmonic phase. Besides, note that we observed the interference between attosecond pulses which were generated at different instantaneous laser intensity. Some groups reported that the position of destructive interference change depending on the intensity of the laser pulse. This effects may affect the CEP dependence of the fringes.

In chapter 4 we observed MF-PADs for OCS molecules irradiated with elliptically polarized femtosecond pulses which are tunnel ionized and dissociate with elliptically polarized pulses. The orientation-dependent tunnel ionization rates for each dissociation channel (S^+ , CO^+ , CS^+ , and O^+) were reconstructed from the up/total asymmetry $A_{\text{MF-PAD}}$ by using the angular streaking method. The asymmetry $A_{\text{MF-PAD}}$ was found to depend on the dissociation channels and the laser intensity: 1. The magnitude of the asymmetry became larger when the laser intensity increased from $0.5 \times 10^{14} \text{ W/cm}^2$ to $1.0 \times 10^{14} \text{ W/cm}^2$, while that became smaller when the laser intensity increased up to $1.5 \times 10^{14} \text{ W/cm}^2$ or $2.2 \times 10^{14} \text{ W/cm}^2$. 2. The asymmetry $A_{\text{MF-PAD}}$ of the photoelectrons which correspond to the channels producing fragment ions of S^+ , CO^+ , or CS^+ had positive values, while that for the channel producing O^+ had negative values. By considering the basics of angular streaking method, the second results showed that OCS molecules are more likely to be ionized when the electric field is directing from the O atom to the S atom for the dissociation channels which produce S^+ , CO^+ , and CS^+ , while those are more likely to be ionized when the electric field is directing from the S atom to the O atom for the dissociation channel which produces O^+ . In order to understand the dissociation mechanism of OCS^+ molecules, we performed numerical simulations where the dissociation probability was calculated within the ADK model, and compared it with the experimental results. The simulation revealed that the multiphoton excitation into dissociative electronic states of OCS^+ molecules after tunnel ionization of the HOMO of OCS molecules dominantly took place rather than the direct tunnel ionization into the dissociative electronic states for the S^+ , CO^+ , and CS^+ channels. This model may

explain why the observed orientation-dependent ionization rates for S^+ , CO^+ , and CS^+ are consistent with the results by the photoelectron measurement with oriented OCS molecules [23] and the results of the numerical simulation within the WFAT, in which the HOMO of OCS molecules are considered. Comparing the experimental results with previous research done with other light sources (synchrotron radiation, atomic discharge, etc.), we also showed that the intensity dependence of the asymmetry $A_{\text{MF-PAD}}$ can be explained by variation of the final population of the electronic states (X, A, B, C, etc.) of OCS^+ molecules. The final population was expected to be sensitive to the laser intensity, and determined by a combination of the tunnel ionization and the multiphoton excitation.

The apparently different asymmetry $A_{\text{MF-PAD}}$ for the O^+ channel implied the tunnel ionization mechanism was not the same as other channels. To the best of our knowledge, it is not clear how O^+ cations are produced during the dissociation of OCS^+ molecules. One possible situation leading to this result is the tunnel ionization of inner orbitals (HOMO-1, HOMO-2, and etc.) of OCS molecules.

This is the first observation of MF-PAD of triatomic molecules by using the coincidence measurement technique. This measurement, for the first time, found the effects of the inner molecular orbitals (HOMO, HOMO-1, HOMO-2, etc.), which cannot be obtained with the orientation techniques such as AC+DC, two-color laser fields, and plasma-shuttering techniques. The contribution of the multiphoton excitation for OCS molecules was much larger than that for HCl molecules. The difference may come from the larger Stark shifts (permanent dipoles, polarizabilities) for OCS molecules than that for HCl molecules. The effect of the Stark shifts is one of the most important to reveal the tunnel ionization dynamics in polar molecules with large permanent dipole and polarizability.

Finally, the explanation we made were on many assumptions. For example, the C states decay much faster than the rotational period of OCS molecules and the multiphoton excitation after ionization was as probable as tunnel ionization into excited states. These assumptions could be confirmed by calculating the transition matrix. Experimentally, by using the few cycle pulses, the multiphoton excitation from the ground state will be suppressed and the discussion would clearly elucidate the effects of tunnel ionization of inner molecular orbitals.

In the present thesis, we break inversion symmetry by employing inversion asymmetric laser field (chapter 3) or orienting polar molecules (chapter 4). The next challenge would be the combination of these techniques such as high-order harmonic generation from oriented molecules with CEP-controlled few-cycle pulses, secondly, a coincidence

measurement of dissociative tunnel ionization of polar molecules with CEP-controlled few-cycle pulses. In those configurations, the electron emits or recombines from only one direction in the molecular frame. There are possibilities to obtain new information such as the electron recombination (scattering) cross sections of polar molecules.

Appendix A

Atomic units

Atomic units are summarized in table A.1.

Table A.1: Conversion and formulas for atomic units. The values of atomic units in SI are given in Ref. [62] for constants, and in Ref. [139] for dimensions.

constant	symbol	SI units	
reduced Planck's constant	\hbar	$1.054571726(47) \times 10^{-34}$ Js	
elementary charge	e	$1.602176565(35) \times 10^{-19}$ C	
electron mass	m_e	$9.10938291(40) \times 10^{-31}$ kg	
dimension	symbol	formula	SI units
length	a_0	$4\pi\epsilon_0\hbar^2/(m_e e^2)$	5.291772×10^{-11} m
energy	E_h	$e^2/4\pi\epsilon_0 a_0$	4.359748×10^{-18} J
time	s	$4\pi\epsilon_0 a_0 \hbar / e^2$	2.418884×10^{-17} s
velocity	v_0	$e^2/4\pi\epsilon_0 \hbar$	2.418884×10^{-17} m/s

Acknowledgment

This work presented in this thesis comprises the contributions of many people. This chapter is dedicated to thank them.

First of all I have to express my deep appreciation to my supervisor, Professor Hirofumi Sakai, for giving me a wonderful opportunity to study in his laboratory with great experimental environment. I also thank him for his persistence and enthusiasm, which strongly stimulate me to propel the

I am extremely grateful to Dr. Shinichirou Minemoto. the Assistant Professor in the laboratory, for teaching me the basics of experiment and various measurement techniques, and for maintaining lasers and experimental apparatuses. I am also thankful to him for a lot of invaluable advice he gave to me.

I have to thank Dr. Ryo Yamashiro for outstanding contribution during early stage of the CO-VIS project. He taught me how to handle the CO-VIS apparatus, and vacuum systems.

I have to thank Dr. Kosaku Kato. A simulation code used to calculate the high-order harmonic spectra in chapter 3 was provided by him. His deep insights into high-order harmonic generation helped me conducting my research.

I would like to thank Mr. Je-Hoi Mun for his useful advice on handling and reassembling the Even-Lavie valve.

I would like to thank Mr. Kei Nakagawa for discussion on high-order harmonic generation.

I thank all the former members and visiting researchers of the laboratory, especially to Dr. Tsuneto Kanai, Dr. Hiraku Matsukuma, Dr. Tomoya Mizuno, Dr. Kyo Nakajima, Mr. Masahiro Muramatsu, Mr. Akihisa Goban, Mr. Keita Oda, Mr. Gentaro Watanabe, Mr. Masafumi Hita, Mr. Midai Suzuki, Mr. Tetsuro Hoshino, and Mr. Daisuke Takei. I genuinely indebted to them for their and kindness and support.

I would like to thank undergraduate students who supported my research. Mr. Yo Iida constructed a SIMION simulation code to optimize the voltages of the electrostatic lens of the spectrometer, and to calculate accurate time of flights and positions of ions and electrons. Mr. Koji Nagano simulated the electron trajectories after ionization and

confirmed the angular streaking was valid under our experimental conditions.

I sincerely appreciate the kind support of Dr. Masakazu Yamazaki. He gave me a lot of advice to handle the CO-VIS system.

I would like to thank Professor Akira Yagishita for helping constructing our CO-VIS system, and for many advice to handle the system.

I would like to thank Dr. Achim Czasch for helping the optimization of the CO-VIS system.

I express deep gratitude to Professor Kenichi Ishikawa, Chief of the thesis defence committee, and Professor Yohei Kobayashi, Professor Tohru Suemoto, Professor Jiro Itatani, and Professor Shinji Tsuneyuki, the members of the thesis defence committee, for a lot of valuable advice and comments on the thesis.

I greatly appreciate the members of the machine shop of the physics department for their excellent technical supports. I would also like to thank the secretaries for their clerical supports.

Finally, I would like to thank my family for their warm support and encouragement.

Bibliography

- [1] Leybold. *Vacuum Full Line Catalog*, http://www.fe.infn.it/~barion/docs/vacuum/vacuum_symbols, 2005.
- [2] O. Svelto. *Principles of Lasers FIFTH EDITION*. Springer, 2010.
- [3] Jean-Claude Diels and Wolfgang Rudolph. *Ultrashort Laser Pulse Phenomena*. Elsevier Inc., 2006.
- [4] D. Strickland and G. Mourou. Compression of Amplified Chirped Optical Pulses. *Opt. Commun.*, 55(6):447–449, 1985.
- [5] N. J. Kylstra C. J. Joachain and R. M. Potvliege. *ATOMS IN INTENSE LASER FIELDS*. CABRIDGE UNIVERSITY PRESS, 2012.
- [6] L. D. Landau and E. M. Lifshitz. *Quantum Mechanics (Non-Relativistic Theory) Third revised edition*. Pergamon Press, 1977.
- [7] N. B. Delone and V. P. Krainov. Energy and angular electron spectra for the tunnel ionization of atoms by strong low-frequency radiation. *JOSA B*, 8(6):1207–1211, 1991.
- [8] T. H. Maiman. Stimulated Optical Radiation in Ruby. *Nature*, 187:493–494, 1960.
- [9] P. A. Franken, A. E. Hill, C. W. Peters, and G. Weinreich. Generation of optical harmonics. *Phys. Rev. Lett.*, 7:118–119, 1961.
- [10] G. H. C. New and J. F. Ward. Optical third-harmonic generation in gases. *Phys. Rev. Lett.*, 19(10):556, 1967.
- [11] M Ferray, Anne L’ Huillier, X F Li, L a Lompre, G Mainfray, and C Manus. Multiple-harmonic conversion of 1064 nm radiation in rare gases. *J. Phys. B At. Mol. Opt. Phys.*, 21:L31–L35, 1988.
- [12] X. F. Li, A. L’ Huillier, M. Ferray, L. A. Lompré, and G. Mainfray. Multiple-harmonic generation in rare gases at high laser intensity. *Phys. Rev. A*, 39(11):5751–5761, 1989.

- [13] J. J. Macklin, J. D. Kmetec, and C. L. Gordon. High-order harmonic generation using intense femtosecond pulses. *Phys. Rev. Lett.*, 70(6):766–769, 1993.
- [14] J. Itatani, J. Levesque, D. Zeidler, Hiromichi Niikura, H. Pépin, J. C. Kieffer, P. B. Corkum, and D. M. Villeneuve. Tomographic imaging of molecular orbitals. *Nature*, 432(7019):867–871, December 2004.
- [15] H. Akagi, T. Otobe, A. Staudte, A. Shiner, F. Turner, R. Dörner, D. M. Villeneuve, and P. B. Corkum. Laser tunnel ionization from multiple orbitals in HCl. *Science*, 325(11):1364–1367, 2009.
- [16] Andrius Baltuška, Matthias Uiberacker, Eleftherios Goulielmakis, Reinhard Kienberger, Vladislav S. Yakovlev, Thomas Udem, Theodor W. Hänsch, and Ferenc Krausz. Phase-Controlled Amplification of Few-Cycle Laser Pulses. *IEEE J. Sel. Top. Quantum Electron.*, 9(4):972–989, 2003.
- [17] Hideki Ohmura and M. Tachiya. Robust quantum control of molecular tunneling ionization in the space domain by phase-controlled laser fields. *Phys. Rev. A*, 77(2):023408, February 2008.
- [18] Henrik Stapelfeldt and Tamar Seideman. Colloquium: Aligning molecules with strong laser pulses. 75(April):543–557, 2003.
- [19] A. Staudte, S. Patchkovskii, D. Pavičić, H. Akagi, Olga Smirnova, D. Zeidler, M. Meckel, D. Villeneuve, R. Dörner, M. Ivanov, and P. B. Corkum. Angular Tunneling Ionization Probability of Fixed-in-Space H₂ Molecules in Intense Laser Pulses. *Phys. Rev. Lett.*, 102(3):033004, January 2009.
- [20] E. Cormier and M. Lewenstein. Optimizing the efficiency in high order harmonic generation optimization by two-color fields. *Eur. Phys. J. D*, 12:227–233, 2000.
- [21] G. G. Paulus, F. Grasbon, H. Walther, P. Villoresi, M. Nisoli, S. Stagira, E. Priori, and S. De Silvestri. Absolute-phase phenomena in photoionization with few-cycle laser pulses. *Nature*, 414(November):182–184, 2001.
- [22] Reinhard Kienberger and Eleftherios Goulielmakis. Atomic transient recorder. *Nature*, 427(February):817–821, 2004.
- [23] Lotte Holmegaard, Jonas L. Hansen, Line Kalthøj, Sofie Louise Kragh, Henrik Stapelfeldt, Frank Filsinger, Jochen Küpper, Gerard Meijer, Darko Dimitrovski, Mahmoud Abu-samha, Christian P. J. Martiny, and Lars Bojer Madsen. Photoelectron angular distributions from strong-field ionization of oriented molecules. *Nat. Phys.*, 6(6):428–432, May 2010.

- [24] P. M. Kraus, D. Baykusheva, and H. J. Wörner. Two-Pulse Field-Free Orientation Reveals Anisotropy of Molecular Shape Resonance. *Phys. Rev. Lett.*, 113(2):023001, July 2014.
- [25] J. Wu, L. Ph. H. Schmidt, M. Kunitski, M. Meckel, S. Voss, H. Sann, H. Kim, T. Jahnke, A. Czasch, and R. Dörner. Multiorbital Tunneling Ionization of the CO Molecule. *Phys. Rev. Lett.*, 108(18):183001, April 2012.
- [26] Ferenc Krausz and Misha Ivanov. Attosecond physics. *Rev. Mod. Phys.*, 81(1):163–234, February 2009.
- [27] Tsuneto Kanai, Shinichirou Minemoto, and Hirofumi Sakai. Quantum interference during high-order harmonic generation from aligned molecules. *Nature*, 435(7041):470–474, May 2005.
- [28] Tsuneto Kanai, Shinichirou Minemoto, and Hirofumi Sakai. Ellipticity Dependence of High-Order Harmonic Generation from Aligned Molecules. *Phys. Rev. Lett.*, 98(5):053002, February 2007.
- [29] Kosaku Kato, Shinichirou Minemoto, and Hirofumi Sakai. Suppression of high-order-harmonic intensities observed in aligned CO₂ molecules with 1300-nm and 800-nm pulses. *Phys. Rev. A*, 84(2):021403, August 2011.
- [30] S. Baker, J. S. Robinson, C. A. Haworth, H. Teng, R. A. Smith, C. C. Chirila, Manfred Lein, J. W. G. Tisch, and Jonathan P. Marangos. Probing proton dynamics in molecules on an attosecond time scale. *Science*, 312(5772):424–427, April 2006.
- [31] Hiroki Mizutani, Shinichirou Minemoto, Yuichiro Oguchi, and Hirofumi Sakai. Effect of nuclear motion observed in high-order harmonic generation from D₂ H₂ molecules with intense multi-cycle 1300 nm and 800 nm pulses. *J. Phys. B At. Mol. Opt. Phys.*, 44(8):081002, April 2011.
- [32] A. Baltuška, T. Udem, M. Uiberacker, M. Hentschel, E. Goulielmakis, Ch. Gohle, R. Holzwarth, V. S. Yakovlev, A. Scrinzi, T. W. Hönsch, and F. Krausz. Attosecond control of electronic processes by intense light fields. *Nature*, 421(February):611, 2003.
- [33] Giuseppe Sansone, E. Benedetti, J.-P. Caumes, S. Stagira, Caterina Vozzi, M. Pascolini, L. Poletto, P. Villoresi, S. De Silvestri, and Mauro Nisoli. Measurement of Harmonic Phase Differences by Interference of Attosecond Light Pulses. *Phys. Rev. Lett.*, 94(19):193903, May 2005.

- [34] Yusuke Sakemi, Kosaku Kato, Shinichirou Minemoto, and Hirofumi Sakai. Characteristics of high-order harmonics generated from atoms and aligned molecules with carrier-envelope-phase-stabilized 25-fs pulses. *Phys. Rev. A*, 85(5):051801, May 2012.
- [35] Yann Mairesse and F. Quéré. Frequency-resolved optical gating for complete reconstruction of attosecond bursts. *Phys. Rev. A*, 71(1):011401, January 2005.
- [36] Kenneth J. Schafer. Strong Field Laser Physics. In Thomas Brabec, editor, *Strong F. Laser Phys.*, volume 134 of *Springer Series in Optical Sciences*, pages 111–145. Springer New York, New York, NY, 2009.
- [37] Toru Morishita, Anh-Thu Le, Zhangjin Chen, and C. D. Lin. Accurate Retrieval of Structural Information from Laser-Induced Photoelectron and High-Order Harmonic Spectra by Few-Cycle Laser Pulses. *Phys. Rev. Lett.*, 100(1):013903, January 2008.
- [38] D. Ray, B. Ulrich, I. Bocharova, C. Maharjan, P. Ranitovic, B. Gramkow, M. Margravelidze, S. De, I. V. Litvinyuk, A. Le, Toru Morishita, C. D. Lin, G. G. Paulus, and C. L. Cocke. Large-Angle Electron Diffraction Structure in Laser-Induced Rescattering from Rare Gases. *Phys. Rev. Lett.*, 100(14):143002, April 2008.
- [39] D. Ray, Zhangjin Chen, S. De, W. Cao, I. V. Litvinyuk, a. T. Le, C. D. Lin, Matthias F. Kling, and C. L. Cocke. Momentum spectra of electrons rescattered from rare-gas targets following their extraction by one- and two-color femtosecond laser pulses. *Phys. Rev. A*, 83(1):013410, January 2011.
- [40] M. Meckel, D. Comtois, D. Zeidler, A. Staudte, D. Pavicic, H. C. Bandulet, H. Pépin, J. C. Kieffer, R. Dörner, D. M. Villeneuve, and P. B. Corkum. Laser-induced electron tunneling and diffraction. *Science*, 320:1478–1482, 2008.
- [41] X. M. Tong, Z. X. Zhao, and C. D. Lin. Theory of molecular tunneling ionization. *Phys. Rev. A*, 66(3):033402, September 2002.
- [42] A. S. Alnaser, C. M. Maharjan, X. M. Tong, B. Ulrich, P. Ranitovic, B. Shan, Z. Chang, C. D. Lin, C. L. Cocke, and I. V. Litvinyuk. Effects of orbital symmetries in dissociative ionization of molecules by few-cycle laser pulses. *Phys. Rev. A*, 71(3):031403, March 2005.
- [43] Domagoj Pavičić, Kevin F. Lee, D. M. Rayner, P. B. Corkum, and D. M. Villeneuve. Direct Measurement of the Angular Dependence of Ionization for N₂, O₂, and CO₂ in Intense Laser Fields. *Phys. Rev. Lett.*, 98(24):243001, June 2007.

- [44] Hideki Ohmura, Naoaki Saito, and Toru Morishita. Molecular tunneling ionization of the carbonyl sulfide molecule by double-frequency phase-controlled laser fields. *Phys. Rev. A*, 89(1):013405, January 2014.
- [45] Eugene Frumker, N. Kajumba, J. B. Bertrand, Hans Jakob Wörner, C. T. Hebeisen, P. Hockett, Michael Spanner, Serguei Patchkovskii, G. G. Paulus, D. M. Villeneuve, A. Naumov, and P. B. Corkum. Probing Polar Molecules with High Harmonic Spectroscopy. *Phys. Rev. Lett.*, 109(23):233904, December 2012.
- [46] Eugene Frumker, C. T. Hebeisen, N. Kajumba, J. B. Bertrand, Hans Jakob Wörner, Michael Spanner, D. M. Villeneuve, A. Naumov, and P. B. Corkum. Oriented Rotational Wave-Packet Dynamics Studies via High Harmonic Generation. *Phys. Rev. Lett.*, 109(11):113901, September 2012.
- [47] Shian Zhang, Chenhui Lu, Tianqing Jia, Zugeng Wang, and Zhenrong Sun. Controlling field-free molecular orientation with combined single- and dual-color laser pulses. *Phys. Rev. A*, 83(4):043410, April 2011.
- [48] R. V. Kulyagin and V. D. Taranukhin. Tunneling ionization of atoms and ions in a strong laser field and the effect of local ionization suppression. *Laser Phys.*, 3(3):644–650, 1993.
- [49] Darko Dimitrovski, Mahmoud Abu-samha, Lars Bojer Madsen, Frank Filsinger, Gerard Meijer, Jochen Küpper, Lotte Holmegaard, Line Kalhøj, Jens H. Nielsen, and Henrik Stapelfeldt. Ionization of oriented carbonyl sulfide molecules by intense circularly polarized laser pulses. *Phys. Rev. A*, 83(2):023405, February 2011.
- [50] Oleg I. Tolstikhin, Toru Morishita, and Lars Bojer Madsen. Theory of tunneling ionization of molecules: Weak-field asymptotics including dipole effects. *Phys. Rev. A*, 84(5):053423, November 2011.
- [51] D. Dimitrovski, Christian P. J. Martiny, and Lars Bojer Madsen. Strong-field ionization of polar molecules: Stark-shift-corrected strong-field approximation. *Phys. Rev. A*, 82(5):053404, November 2010.
- [52] M. Abu-samha and Lars Bojer Madsen. Photoelectron angular distributions from polar molecules probed by intense femtosecond lasers. *Phys. Rev. A*, 82(4):043413, October 2010.
- [53] T. Otobe, K. Yabana, and J.-I. Iwata. First-principles calculations for the tunnel ionization rate of atoms and molecules. *Phys. Rev. A*, 69(5):053404, May 2004.

- [54] Frank Filsinger, Jochen Küpper, Gerard Meijer, Lotte Holmegaard, Jens H. Nielsen, Itach Nevo, Jonas L. Hansen, and Henrik Stapelfeldt. Quantum-state selection, alignment, and orientation of large molecules using static electric and laser fields. *J. Chem. Phys.*, 131(6):064309, August 2009.
- [55] Hideki Ohmura, Naoaki Saito, Hidehiko Nonaka, and Shingo Ichimura. Dissociative ionization of a large molecule studied by intense phase-controlled laser fields. *Phys. Rev. A*, 77(5):053405, May 2008.
- [56] Hideki Ohmura, Naoaki Saito, and Toru Morishita. Quantum control of molecular tunneling ionization in the spatiotemporal domain. *Phys. Rev. A*, 83(6):063407, June 2011.
- [57] H. Li, D. Ray, S. De, I. Znakovskaya, W. Cao, G. Laurent, Z. Wang, Matthias F. Kling, A. T. Le, and C. L. Cocke. Orientation dependence of the ionization of CO and NO in an intense femtosecond two-color laser field. *Phys. Rev. A*, 84(4):043429, October 2011.
- [58] Olga Smirnova, Yann Mairesse, Serguei Patchkovskii, Nirit Dudovich, D. M. Villeneuve, P. B. Corkum, and Misha Yu. Ivanov. High harmonic interferometry of multi-electron dynamics in molecules. *Nature*, 460(7258):972–977, August 2009.
- [59] Brian K. McFarland, Joseph P. Farrell, Philip H. Bucksbaum, and Markus Gühr. High harmonic generation from multiple orbitals in N₂. *Science*, 322(5905):1232–1235, November 2008.
- [60] J. Ullrich, R. Moshhammer, A Dorn, R Döner, L. Ph. Schmidt, and H Schmidte-Böcking. Recoil-ion and electron momentum spectroscopy: reaction-microscopes. *Rep. prog. Phys.*, 66:1463, 2003.
- [61] T. Morishita. private communication.
- [62] “nist computational chemistry comparison and benchmark database,” nist standard reference database number 101, release 16a, august 2013, editor: Russell d. johnson iii, <http://cccbdb.nist.gov/>.
- [63] L. V. Keldysh. Ionization in the field of a string electromagnetic wave. *J. Exp. Theor. Phys.*, 20(5):1307–1314, 1965.
- [64] N. B. Delone and Vladimir P. Krainov. Tunneling and barrier-suppression ionization of atoms and ions in a laser radiation field. *Physics-Uspekhi*, 41(5):469–485, May 1998.

- [65] Maciej Lewenstein, Philippe Balcou, Misha Yu. Ivanov, A L’Huillier, and P. B. Corkum. Theory of high-harmonic generation by low-frequency laser fields. *Phys. Rev. A*, 49(3):2117, 1994.
- [66] M. V. Ammosov, N. B. Delone, and V. P. Krainov. Tunnel ionization of complex atoms and of atomic ions in an alternating electromagnetic field. *Zh. Eksp. Teor. Fiz.*, 91:2008, 1986.
- [67] P. B. Corkum, N. H. Burnett, and F. Brunel. Above-threshold ionization in the long-wavelength limit. *Phys. Rev. Lett.*, 62(11):1259–1262, 1989.
- [68] W. Xiong and S. L. Chin. Tunnel ionization of potassium and xenon atoms in a high-intensity CO₂ laser radiation field. *Sov. Phys. JETP*, 72(September 1990):268–271, 1991.
- [69] U. Mohideen, M. H. Sher, H. W. K. Tom, G. D. Aumiller, O. R. Wood, R. R. Freeman, J. Bokor, and P. H. Bucksbaum. High intensity above-threshold ionization of He. *Phys. Rev. Lett.*, 71(4):509–512, 1993.
- [70] Emmanuel Penka Fowe and Andre D. Bandrauk. Nonperturbative time-dependent density-functional theory of ionization and harmonic generation in OCS and CS₂ molecules with ultrashort intense laser pulses: Intensity and orientational effects. *Phys. Rev. A*, 84(3):035402, September 2011.
- [71] Emmanuel Penka Fowe and Andre D. Bandrauk. Nonlinear time-dependent density-functional-theory study of ionization and harmonic generation in CO₂ by ultrashort intense laser pulses: Orientational effects. *Phys. Rev. A*, 81(2):023411, February 2010.
- [72] Song-Feng Zhao, Cheng Jin, Anh-Thu Le, T. F. Jiang, and C. D. Lin. Determination of structure parameters in strong-field tunneling ionization theory of molecules. *Phys. Rev. A*, 81(3):033423, March 2010.
- [73] Lars Bojer Madsen, Frank Jensen, Oleg I. Tolstikhin, and Toru Morishita. Structure factors for tunneling ionization rates of molecules. *Phys. Rev. A*, 87(1):013406, January 2013.
- [74] Oleg I. Tolstikhin and Toru Morishita. Adiabatic theory of ionization by intense laser pulses: Finite-range potentials. *Phys. Rev. A*, 86(4):043417, October 2012.
- [75] K. Kato. *Observation of the phase differences of near-threshold high-order harmonics generated in atoms and molecules*. PhD thesis, The University of Tokyo, Japan, 2014.

- [76] Zenghu Chang. *Fundamentals of Attosecond Optics*. CRC Press, 2011.
- [77] Takao Fuji, Jens Rauschenberger, Alexander Apolonski, Vladislav S. Yakovlev, Gabriel Tempea, Thomas Udem, Christoph Gohle, Theodor W. Hänsch, Walter Lehnert, Michael Scherer, and Ferenc Krausz. Monolithic carrier-envelope phase-stabilization scheme. *Opt. Lett.*, 30(3):332–334, February 2005.
- [78] Jens Rauschenberger, Takao Fuji, M. Hentschel, A.-J. Verhoef, T. Udem, C. Gohle, T. W. Hänsch, and Ferenc Krausz. Carrier-envelope phase-stabilized amplifier system. *Laser Phys. Lett.*, 3(1):37–42, January 2006.
- [79] Christian Spielmann, Peter F. Curley, Thomas Brabec, and Ferenc Krausz. Ultrabroadband femtosecond lasers. *IEEE J. Quantum Electron.*, 30(4):1100–1114, 1994.
- [80] Mauro Nisoli, S. De Silvestri, and O. Svelto. Generation of high energy 10 fs pulses by a new pulse compression technique. *Appl. Phys. Lett.*, 68(20):2793, 1996.
- [81] Mauro Nisoli, S. De Silvestri, O. Svelto, R. Szipöcs, K. Ferencz, Christian Spielmann, S. Sartania, and Ferenc Krausz. Compression of high-energy laser pulses below 5 fs. *Opt. Lett.*, 22(8):522–524, April 1997.
- [82] R. Szipöcs, K. Ferencz, Christian Spielmann, and Ferenc Krausz. Chirped multilayer coatings for broadband dispersion control in femtosecond lasers. *Opt. Lett.*, 19(3):201, February 1994.
- [83] C. Iaconis and I. A. Walmsley. Spectral phase interferometry for direct electric-field reconstruction of ultrashort optical pulses. *Opt. Lett.*, 23(10):792–794, May 1998.
- [84] C. Iaconis and I. A. Walmsley. Self-referencing spectral interferometry for measuring ultrashort optical pulses. *IEEE J. Quantum Electron.*, 35(4):501–509, April 1999.
- [85] Marcus Zimmermann, Christoph Gohle, Ronald Holzwarth, Thomas Udem, and Theodor W. Hänsch. Optical clockwork with an offset-free difference-frequency comb: accuracy of sum- and difference-frequency generation. *Opt. Lett.*, 29(3):310–312, 2004.
- [86] Takao Fuji, Alexander Apolonski, and Ferenc Krausz. Self-stabilization of carrier-envelope offset phase by use of difference-frequency generation. *Opt. Lett.*, 29(6):632–634, 2004.

- [87] L. Xu, Christian Spielmann, A. Poppe, T. Brabec, Ferenc Krausz, and T. W. Hänsch. Route to phase control of ultrashort light pulses. *Opt. Lett.*, 21(24):2008–2010, December 1996.
- [88] Pascal Salières, A. L’Huillier, and Maciej Lewenstein. Coherence Control of High Order Harmonics. *Phys. Rev. Lett.*, 74(19):3776–3779, 1995.
- [89] Philippe Balcou, Pascal Salières, Anne L’Huillier, and Maciej Lewenstein. Generalized phase-matching conditions for high harmonics: The role of field-gradient forces. *Phys. Rev. A*, 55(4):3204–3210, 1997.
- [90] F. Rosca-Pruna and M. Vrakking. Experimental Observation of Revival Structures in Picosecond Laser-Induced Alignment of I_2 . *Phys. Rev. Lett.*, 87(15):153902, September 2001.
- [91] Tamar Seideman and Edward Hamilton. Nonadiabatic alignment by intense pulses . Concepts , theory , and directions. *Adv. At., Mol., Opt. Phys.*, 52:289–329, 2006.
- [92] K. Kato. High-order harmonic generation from aligned molecules with 800-nm and 1300-nm femtosecond pulses, master’s thesis. Master’s thesis, The University of Tokyo, Japan, 2011.
- [93] Anh-Thu Le, X. M. Tong, and C. D. Lin. Alignment dependence of high-order harmonic generation from CO_2 . *J. Mod. Opt.*, 54(7):967–980, May 2007.
- [94] Ove Christiansen, Christof Hattig, and Jürgen Gauss. Polarizabilities of CO, N_2 , HF, Ne, BH, and CH^+ from ab initio calculations: Systematic studies of electron correlation, basis set errors, and vibrational contributions. *J. Chem. Phys.*, 109(12):4745, 1998.
- [95] Masanori Kaku, Keita Masuda, and Kenzo Miyazaki. Observation of Revival Structure in Femtosecond-Laser-Induced Alignment of N_2 with High-Order Harmonic Generation. *Jpn. J. Appl. Phys.*, 43(No. 4B):L591–L593, April 2004.
- [96] J. Itatani, D. Zeidler, J. Levesque, M. Spanner, D. M. Villeneuve, and P. B. Corkum. Controlling High Harmonic Generation with Molecular Wave Packets. *Phys. Rev. Lett.*, 94(12):123902, March 2005.
- [97] Mitsuo Takeda, Hideki Ina, and Seiji Kobayashi. Fourier-transform method of fringe-pattern analysis for computer-based topography and interferometry. *J. Opt. Soc. Am.*, 72(1):156, January 1982.
- [98] Mauro Nisoli, Giuseppe Sansone, S. Stagira, S. De Silvestri, C. Vozzi, M. Pascolini, L. Poletto, P. Villoresi, and G. Tondello. Effects of carrier-envelope phase differences

- of few-optical-cycle light pulses in single-shot high-order-harmonic spectra. *Phys. Rev. Lett.*, 91(21):213905, 2003.
- [99] E. Mansten, J. Dahlström, Johan Mauritsson, T. Ruchon, Anne L' Huillier, J. Tate, Mette B. Gaarde, Petrisa Eckle, A. Guandalini, M. Holler, F. Schapper, L. Gallmann, and Ursula Keller. Spectral Signature of Short Attosecond Pulse Trains. *Phys. Rev. Lett.*, 102(8):083002, February 2009.
- [100] Katalin Varjú, Yann Mairesse, B. Carré, Mette B. Gaarde, Per Johnsson, S. Kazamias, Rodrigo López-Martens, Johan Mauritsson, K. J. Schafer, Philippe Balcou, A. L'huillier, and Pascal Salières. Frequency chirp of harmonic and attosecond pulses. *J. Mod. Opt.*, 52(2-3):379–394, January 2005.
- [101] Maciej Lewenstein, Pascal Salières, and A L'huillier. Phase of the atomic polarization in high-order harmonic generation. *Phys. Rev. A*, 52(6):4747–4754, 1995.
- [102] Mette B. Gaarde, F. Salin, E. Constant, Philippe Balcou, K. Schafer, K. Kulander, and Anne L' Huillier. Spatiotemporal separation of high harmonic radiation into two quantum path components. *Phys. Rev. A*, 59(2):1367–1373, February 1999.
- [103] Pascal Salières, B. Carré, L. Le Déroff, F. Grasbon, G. G. Paulus, H. Walther, R. Kopold, W. Becker, D. B. Milošević, A. Sanpera, and Maciej Lewenstein. Feynman's path-integral approach for intense-laser-atom interactions. *Science*, 292(5518):902–905, May 2001.
- [104] Mette B. Gaarde and Kenneth Schafer. Quantum path distributions for high-order harmonics in rare gas atoms. *Phys. Rev. A*, 65(3):031406, March 2002.
- [105] Taro Sekikawa, Tomotaka Katsura, Satoshi Miura, and Shuntaro Watanabe. Measurement of the Intensity-Dependent Atomic Dipole Phase of a High Harmonic by Frequency-Resolved Optical Gating. *Phys. Rev. Lett.*, 88(19):193902, April 2002.
- [106] Jeffrey Krause, Kenneth Schafer, and Kenneth Kulander. High-order harmonic generation from atoms and ions in the high intensity regime. *Phys. Rev. Lett.*, 68(24):3535–3538, 1992.
- [107] P. B. Corkum. Plasma perspective on strong field multiphoton ionization. *Phys. Rev. Lett.*, 71(13):1994–1997, 1993.
- [108] S. Haessler, J. Caillat, W. Boutu, C. Giovanetti-Teixeira, T. Ruchon, T. Auguste, Z. Diveki, P. Breger, A. Maquet, B. Carré, R. Taïeb, and Pascal Salières. Attosecond imaging of molecular electronic wavepackets. *Nat. Phys.*, 6(3):200–206, January 2010.

- [109] W. Boutu, S. Haessler, H. Merdji, P. Breger, G. Waters, M. Stankiewicz, L. J. Frasinski, R. Taieb, J. Caillat, A. Maquet, P. Monchicourt, B. Carre, and Pascal Salières. Coherent control of attosecond emission from aligned molecules. *Nat. Phys.*, 4(7):545–549, May 2008.
- [110] Tsuneto Kanai, Eiji Takahashi, Yasuo Nabekawa, and Katsumi Midorikawa. Observing molecular structures by using high-order harmonic generation in mixed gases. *Phys. Rev. A*, 77(4):041402, April 2008.
- [111] Xibin Zhou, Robynne Lock, Wen Li, Nick Wagner, Margaret Murnane, and Henry Kapteyn. Molecular Recollision Interferometry in High Harmonic Generation. *Phys. Rev. Lett.*, 100(7):073902, February 2008.
- [112] Kouichi Hosaka, Jun-ichi Adachi, Alexander V. Golovin, Masahiko Takahashi, Noboru Watanabe, and Akira Yagishita. Coincidence Velocity Imaging Apparatus for Study of Angular Correlations between Photoelectrons and Photofragments. *Jpn. J. Appl. Phys.*, 45(3A):1841–1849, March 2006.
- [113] André T. J. B. Eppink and David H. Parker. Velocity map imaging of ions and electrons using electrostatic lenses: Application in photoelectron and photofragment ion imaging of molecular oxygen. *Rev. Sci. Instrum.*, 68(9):3477, 1997.
- [114] M. Takahashi, J. P. Cave, and J. H. D. Eland. Velocity imaging photoionization coincidence apparatus for the study of angular correlations between electrons and fragment ions. *Rev. Sci. Instrum.*, 71(2000):1337, 2000.
- [115] M. Lebeck, J. C. Houver, and D. Dowek. Ion - electron velocity vector correlations in dissociative photoionization of simple molecules using electrostatic lenses. *Rev. Sci. Instrum.*, 73(4):1866, 2002.
- [116] L. D. Landau and E. M. Lifshitz. *Mechanics third edition*. Pergamon Press, 1976.
- [117] RoentDek Handels GmbH. *Manuals*, 2011.
- [118] Uzi Even, J. Jortner, D. Noy, N. Lavie, and C. Cossart-Magos. Cooling of large molecules below 1 K and He clusters formation. *J. Chem. Phys.*, 112(18):8068, 2000.
- [119] Petrisa Eckle, Mathias Smolarski, Philip Schlup, Jens Biegert, André Staudte, Markus Schöffler, Harm G. Muller, Reinhard Dörner, and Ursula Keller. Attosecond angular streaking. *Nat. Phys.*, 4(7):565–570, May 2008.

- [120] Adrian N. Pfeiffer, Claudio Cirelli, Mathias Smolarski, Reinhard Dörner, and Ursula Keller. Timing the release in sequential double ionization. *Nat. Phys.*, 7(5):428–433, March 2011.
- [121] Adrian N. Pfeiffer, Claudio Cirelli, Mathias Smolarski, Darko Dimitrovski, Mahmoud Abu-samha, Lars Bojer Madsen, and Ursula Keller. Attoclock reveals natural coordinates of the laser-induced tunnelling current flow in atoms. *Nat. Phys.*, 8(1):76–80, October 2011.
- [122] A. Staudte. *Subfemtosecond Electron Dynamics of H₂ in Strong fields*. PhD thesis, Institut für Kernphysik, J. W. Goethe Universität, Frankfurt am Main, Germany, 2005.
- [123] M. Mechel. *Laser-Induced Electron Tunneling and Diffraction*. PhD thesis, Institut für Kernphysik, J. W. Goethe Universität, Frankfurt am Main, Germany, 2011.
- [124] A. S. Alnaser, X. Tong, T. Osipov, S. Voss, C. Maharjan, P. Ranitovic, B. Ulrich, B. Shan, Zenghu Chang, C. D. Lin, and C. L. Cocke. Routes to Control of H₂ Coulomb Explosion in Few-Cycle Laser Pulses. *Phys. Rev. Lett.*, 93(18):183202, October 2004.
- [125] P. H. Bucksbaum, A. Zavriyev, H. G. Muller, and D. W. Schumacher. Softening of the H₂⁺ molecular bond in intense laser fields. *Phys. Rev. Lett.*, 64(16):1883–1886, 1990.
- [126] A. S. Alnaser, S. Voss, X. Tong, C. Maharjan, P. Ranitovic, B. Ulrich, T. Osipov, B. Shan, Z. Chang, and C. L. Cocke. Effects Of Molecular Structure on Ion Disintegration Patterns In Ionization of O₂ and N₂ by Short Laser Pulses. *Phys. Rev. Lett.*, 93(11):113003, September 2004.
- [127] Milan Kalal and K. A. Nugent. Abel inversion using fast Fourier transforms. *Appl. Opt.*, 27(3):1956–1959, 1988.
- [128] S. Morse, M. Takahashi, J. H. D. Eland, and L. Karlsson. Dissociative photoionisation of OCS from threshold to 40.8 eV. *Int. J. Mass Spectrom. Ion Processes*, 184:67–74, 1999.
- [129] F. Moncada. Theoretical study of isotope effects in photoelectron spectroscopy.
- [130] G. H. Lee. Photoelectron Spectrum of (D₂O) – 6 Cluster Anions. *JKPS*, 37(1):76–78, 2000.
- [131] M.-J. Hubin-Franskin, J. Delwiche, P.-M. Guyon, M. Richard-Viard, M. Lavollée, O. Dutuit, J.-M. Robbe, and J.-P. Flament. Dissociation of the COS⁺ ion by

- photoionisation: experiment and ab initio calculations The Franck-Condon energy gap an the vibronic state Franck-Condon energy regions, 1996.
- [132] David M. Hirst. Ab initio potential energy surfaces for excited states of the OCS⁺ molecular ion. *Mol. Phys.*, 104(1):55–60, January 2006.
- [133] U. Boesl, R. Weinkauff, C. Weickhardt, and E.W. Schlag. Laser ion sources for time-of-flight mass spectrometry. *Int. J. Mass Spectrom. Ion Process.*, 131:87–124, February 1994.
- [134] Jacques Delwiche. Autoionization of OCS by threshold photoelectron spectroscopy. *J. Chem. Phys.*, 74(8):4219, 1981.
- [135] Chushuan Chang, Chu Yung Luo, and Kopin Liu. Imaging the mode-selected predissociation of OCS⁺. *J. Phys. Chem. A*, 109:1022–1025, 2005.
- [136] J. H. D. Eland. Predissociation of N₂ O⁺ and COS⁺ ions studied by photoelectron-photoion coincidence spectroscopy, 1973.
- [137] M. J. Hubin-Franskin, D. Huard, and P. Marmet. On the heat of formation of CS from CS₂ and OCS. *Int J Mass Spectrom Ion Phys*, 27:263, 1978.
- [138] Hua Dong, Chen Bo-Zhen, Huang Ming-Bao, and Hai-Bo Chang. O-Loss Photodissociation of the OCS⁺ Ion in the Low-Lying Electronic States Studied Using Multiconfiguration Second-Order Perturbation Theory. *Int. J. Quantum Chem.*, 111:3578–3587, 2010.
- [139] Kazuo Takayanagi. *Atomic and molecular physics (Japanese)*. Asakura, 2000.